

FACULTY
OF MATHEMATICS
AND PHYSICS
Charles University

1

BACHELOR THESIS

2

Martin Vavřík

3 4

Simulation and Reconstruction
of Charged Particle Trajectories in an
Atypic Time Projection Chamber

5

Institute of Particle and Nuclear Physics

6 7

Supervisor of the bachelor thesis: Mgr. Tomáš Sýkora, Ph.D.
Study programme: Physics

8

Prague 2025

- ⁹ I declare that I carried out this bachelor thesis independently, and only with the
¹⁰ cited sources, literature and other professional sources. It has not been used to
¹¹ obtain another or the same degree.
- ¹² I understand that my work relates to the rights and obligations under the Act
¹³ No. 121/2000 Sb., the Copyright Act, as amended, in particular the fact that the
¹⁴ Charles University has the right to conclude a license agreement on the use of this
¹⁵ work as a school work pursuant to Section 60 subsection 1 of the Copyright Act.

In date
Author's signature

¹⁶ Dedication.

Title: Simulation and Reconstruction of Charged Particle Trajectories in an Atypical Time Projection Chamber **Added hyphen to avoid overfull hbox**

Author: Martin Vavřík

Institute: Institute of Particle and Nuclear Physics

Supervisor: Mgr. Tomáš Sýkora, Ph.D., Institute of Particle and Nuclear Physics

Abstract: In this work, we describe the development of a reconstruction algorithm for atypical Time Projection Chambers (TPCs) that will be used at IEAP CTU to search for the ATOMKI anomalous internal pair creation [11]. The chambers have an inhomogeneous toroidal magnetic field orthogonal to their electric field, hence we call them Orthogonal Fields TPCs (OFTPCs). This arrangement causes a distortion of the drift inside the chamber and complicates the shape of electron/positron trajectories. We present a few approaches to tackle these problems, the best of which uses a simulated ionization electron drift map for track reconstruction, and Runge-Kutta fit for energy reconstruction. Finally, we show from simulations that, for an ideal charge readout with no multiplication and no noise, we can reach an energy resolution

Keywords: simulation reconstruction time projection chamber

¹⁷ Contents

¹⁸ Motivation	³
0.1 ATOMKI Anomaly	3
0.1.1 ATOMKI Measurements	3
0.1.2 Other Experiments	4
0.2 X17 Project at IEAP CTU	7
 ²³ 1 Time Projection Chamber	 ⁹
1.1 Charge transport in gases	9
1.1.1 Drift	10
1.1.2 Diffusion	11
1.2 Examples of TPCs	12
1.2.1 The original TPC at PEP-4 at SLAC	12
1.2.2 ALICE TPC	12
1.2.3 CERES/NA45 radial-drift TPC	13
1.2.4 Other interesting radial-drift TPCs	15
1.3 Readout	16
1.3.1 Multi-Wire Proportional Chamber	16
1.3.2 Micro-Pattern Gaseous Detectors	17
1.4 Orthogonal Fields TPC at IEAP CTU	19
1.4.1 Motivation and Associated Challenges	20
1.4.2 Coordinate Systems and Dimensions	20
1.4.3 Magnetic Field Simulation	22
 ³⁹ 2 Track Simulation	 ²⁶
2.1 Microscopic Simulation	26
2.1.1 First testing track	27
2.1.2 Grid-like testing sample	27
2.2 Runge-Kutta Simulation	27
2.2.1 Testing sample	30
 ⁴⁵ 3 Track Reconstruction	 ³²
3.1 Reconstruction Assuming Steady Drift	32
3.2 Ionization Electron Map	33
3.2.1 Map Simulation	40
3.2.2 Gradient Descent Algorithm	40
3.2.3 Interpolation on the Inverse Grid	41
3.3 Reconstruction testing	43
3.4 Discrete Reconstruction	43
 ⁵³ 4 Energy Reconstruction	 ⁴⁹
4.1 Cubic Spline Fit	49
4.2 Circle and Lines Fit	50
4.2.1 Two-dimensional fit	52
4.2.2 Three-dimensional fit	53
4.2.3 Testing on a Runge-Kutta sample	56

59	4.3 Runge-Kutta Fit	57
60	4.3.1 Testing on a microscopic sample	61
61	Conclusion	62
62	Future	65
63	Bibliography	68
64	List of Abbreviations	78

Motivation

66 Or chapter 1? MFF UK thesis template uses Introduction as an unnumbered
67 chapter, but it's not clear how they handle numbering inside the chapter. A Time
68 Projection Chamber (TPC) [refs], but what to cite here? D. Nygren (1974)? is
69 a gaseous detector that reconstructs charged particle trajectories by measuring
70 the positions and drift times of ionization electrons (and sometimes also ions)
71 created in the gas. The energies of these particles can be inferred from the
72 curvatures of their trajectories in a magnetic field.

73 The goal of this thesis is to develop an algorithm for the reconstruction of
74 charged particle trajectories and energy in an *atypic* TPC with orthogonal electric
75 and magnetic fields, hereafter referred to as the OFTPC, used in the X17 project
76 at the Institute of Experimental and Applied Physics, Czech Technical University
77 in Prague (IEAP CTU). Furthermore, we present the results of testing of several
78 (gradually improving) developed algorithms with different samples of simulated
79 data. Put this somewhere, (maybe just the abstract?). We use the Garfield++
80 toolkit [1] for simulations in combination with the ROOT framework [2] for data
81 analysis and visualization. Some of our more demanding simulations are run on
82 the MetaCentrum grid [3].

83 The X17 project in IEAP CTU aims to reproduce measurements of anomalous
84 behavior in the angular correlation distribution of pairs produced by the Internal
85 Pair Creation (IPC) mechanism [4] during the decay of certain excited nuclei
86 (^{8}Be , ^{12}C , and ^{4}He) observed by a team at ATOMKI in Hungary. I would leave
87 this here as a short summary before I explain it in more detail in the sections
88 below.

89 Add citations: X17 project, VdG. Maybe also TPC, etc.

0.1 ATOMKI Anomaly

90 Many different theories propose the existence of *new light boson(s)* that are weakly
91 coupled to ordinary matter [5]. These particles are potential dark matter candi-
92 dates and could contribute to a solution of other issues with the Standard Model,
93 such as the strong CP problem¹ and the anomalous muon magnetic moment. Mass
94 range of axions?

95 A possible way of detecting such bosons with a short lifetime is to observe
96 nuclear transitions of excited nuclei. If a boson was emitted during the transition
97 and subsequently decayed into an electron-positron pair, we could observe this as
98 a peak on top of the standard e^+e^- (both cursive and upright forms are used in
99 different articles) angular correlation from the Internal Pair Creation (IPC) and
100 the External Pair Creation (EPC).

0.1.1 ATOMKI Measurements

101 Historically, there were several measurements of the IPC in nuclear transitions
102 in ^{8}Be at Institute für Kernphysik (Frankfurt) [6, 7, 8] and at ATOMKI (Debre-

¹The CP symmetry could be violated in strong interactions according to the current formulation of quantum chromodynamics, but no such violation is observed.

cen, Hungary) [9, 10] resulting in different anomalies with invariant mass in the range 5 – 15 MeV. This motivated the development of a better spectrometer at ATOMKI.

In 2015, a group at ATOMKI observed an anomalous IPC in ${}^8\text{Be}$ [11]. They used the ${}^7\text{Li}(p, \gamma){}^8\text{Be}$ reaction at the $E_p = 1030$ keV proton capture resonance to prepare the 18.15 MeV excited state ($J^\pi = 1^+$, $T = 0$). This state decays predominantly through M1 transitions to the ground state ($J^\pi = 0^+$, $T = 0$) and to the 3.03 MeV state ($J^\pi = 2^+$, $T = 0$) [12]. **Transition figure – all transitions of isotopes? IPC figure?**

The angular correlation of the e^+e^- pairs created internally in these transitions were measured and compared to the simulation; results from a narrow $E_{\text{sum}} = 18$ MeV region are shown in Fig. 0.1a. The simulation includes boson decay pairs for different boson masses. The disparity parameter y is used to describe the asymmetry of energy between the two particles. It is defined as

$$y = \frac{E_{e^-} - E_{e^+}}{E_{e^-} + E_{e^+}}, \quad (0.1)$$

where E_{e^-} and E_{e^+} are the kinetic energies of the electron and positron.

Their experimental setup was later upgraded and used for new measurements. In 2022 the ${}^8\text{Be}$ anomaly was also measured using the $E_p = 441$ keV resonance to produce the 17.64 MeV excited state ($J^\pi = 1^+$, $T = 1$) which again decays primarily to the ground state and the 3.03 MeV state [12]. The anomaly was also verified for $E_p = 650$ and 800 keV where E1 transitions from the direct proton capture dominate [13]. The results for e^+e^- with $E_{\text{sum}} \in [13.5, 20]$ MeV are shown in Fig. 0.1b.

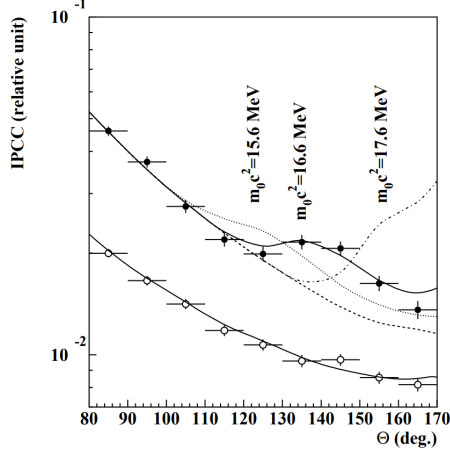
The newer setup was also used in 2021 to study the ${}^3\text{H}(p, e^+e^-){}^4\text{He}$ reaction at $E_p = 510, 610$ and 900 keV [14], inducing direct and resonant capture populating the overlapping first 20.21 MeV ($J^\pi = 0^+$) and second 21.01 MeV ($J^\pi = 0^-$) excited states [15]. The comparison of simulated and measured e^+e^- pair angular correlations in the $E_{\text{sum}} \in [18, 22]$ MeV region is shown in Fig. 0.1c.

In 2022, another anomaly was measured in the ${}^{11}\text{B}(p, e^+e^-){}^{12}\text{C}$ process [16]. The $E_p = 1388$ keV resonance was used to populate the 17.23 MeV excited state ($J^\pi = 1^-, T = 1$) with a large width $\Gamma = 1.15$ MeV [17]. This state decays mainly through E1 transitions to the ground state $J^\pi = 0^+$ and to the 4.44 MeV state $J^\pi = 2^+$. To compensate for energy losses in the target, five energies in the range $E_p = 1.5\text{--}2.5$ MeV were used. The experimental angular correlation for the 17.23 MeV transition to the ground state is shown in Fig. 0.1d.

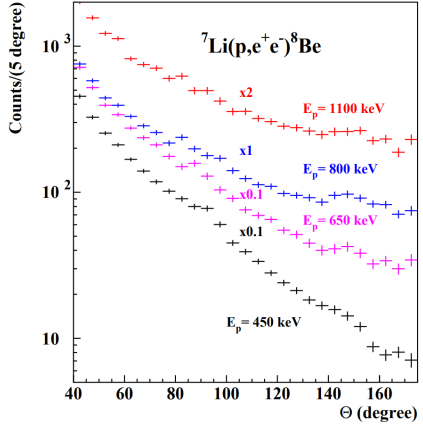
Possible explanations of the anomaly include experimental effects, higher order processes in the Standard Model [18, 19] or even a protophobic fifth force mediated by a new 17 MeV boson X17 [20]. **Not sure if the introduction should be referenced since even though it is related, it is an independent theory developed only (?) to explain these measurements. Zhang and Miller: <https://www.sciencedirect.com/science/article/pii/S0370269321000010> Paper from IEAP CTU: <https://arxiv.org/pdf/2309.12469.pdf>**

0.1.2 Other Experiments

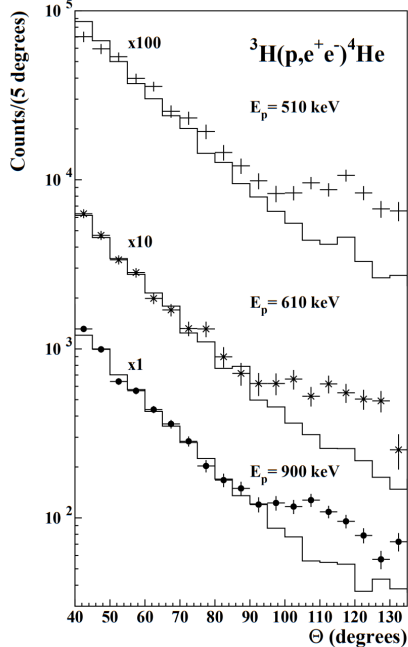
Since the ATOMKI measurements, several experiments have been initiated to attempt to replicate the results and search for the hypothetical X17 particle. The



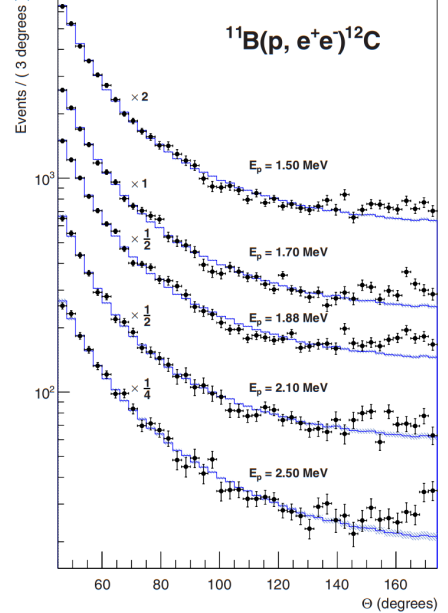
(a) Experimental e^+e^- pair correlations measured in the ${}^7\text{Li}(p, e^+e^-){}^8\text{Be}$ reaction with $|y| \leq 0.5$ (closed circles) and $|y| \geq 0.5$ (open circles) [11].



(b) Experimental e^+e^- pair correlations measured in the ${}^7\text{Li}(p, e^+e^-){}^8\text{Be}$ reaction with the improved setup for different proton beam energies [13].



(c) Experimental e^+e^- pair correlations measured in the ${}^3\text{H}(p, e^+e^-){}^4\text{He}$ reaction with $|y| \leq 0.3$ for different proton beam energies [14].



(d) Experimental e^+e^- pair correlations measured in the ${}^{11}\text{B}(p, e^+e^-){}^{12}\text{C}$ reaction for different proton beam energies [16].

Figure 0.1: The ATOMKI anomalous IPC measured for different nuclei.



Figure 0.2: Results from the Hanoi spectrometer – angular e^+e^- pair correlations measured in the ${}^7\text{Li}(p, e^+e^-){}^8\text{Be}$ reaction at $E_p = 1225$ keV [21].

following experiments have already produced results. Could cite the ATOMKI review paper here. NA64 at SPS: <https://arxiv.org/pdf/1803.07748>.

Two-arm e^+e^- spectrometer in Hanoi

The anomaly in ${}^8\text{Be}$ has been observed with a high ($> 4\sigma$ That's all they write in their article.) confidence by a team at the Hanoi University of Sciences for $E_p = 1225$ keV [21]. They built a two-arm spectrometer in collaboration with ATOMKI and calibrated it using the 17.6 MeV M1 transition. The results are shown in Fig. 0.2.

Collisions at Nuclotron in Dubna

At the Joint Institute for Nuclear Research in Dubna, signal in the form of enhanced structures in the $\gamma\gamma$ spectra at ~ 17 and ~ 38 MeV invariant masses for $p + \text{C}$, $d + \text{C}$ and $d + \text{Cu}$ reactions at momenta 5.5, 2.75, and 3.83 GeV per nucleon [22]. Monte Carlo simulations support the conclusion that the signals are a consequence of a decay of unknown particles X17 and E38.

The MEG II (Muon Electron Gamma) experiment

Experiments using the ${}^7\text{Li}(p, e^+e^-){}^8\text{Be}$ reaction were carried out at the Paul Scherrer Institute with the MEG II superconducting solenoid spectrometer [23]. Analysis of the data with $E_p = 1080$ keV exciting both of the resonances (beam fully stopping in the target) found no significant evidence supporting the X17 hypothesis, results are shown in Fig. 0.3. An upper bound (at 90% confidence) on the X17-to- γ branching ratio was set at $1.2 \cdot 10^{-5}$ for the 18.15 MeV state (larger than the ratio $5.8 \cdot 10^{-6}$ obtained by ATOMKI in 2016). Could add their 90% C.L bounds figure also. Insufficient statistics – 6.2 % (1.5σ) p-value.

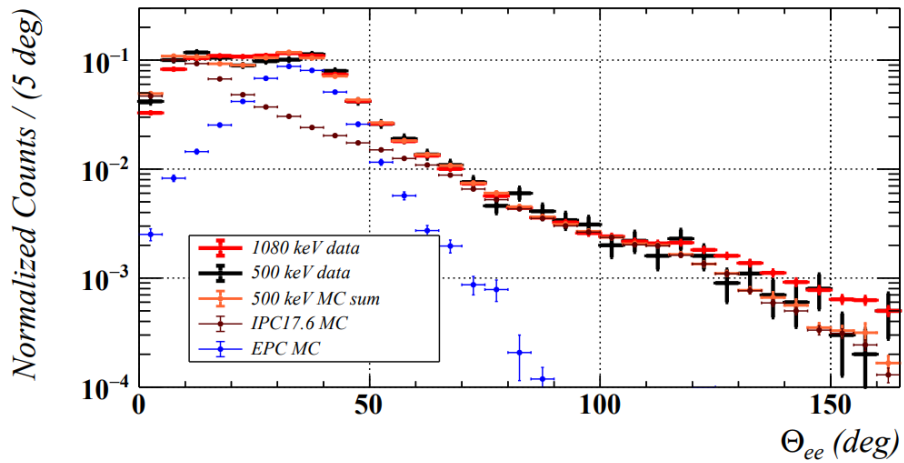


Figure 0.3: Results from the MEG II experiments – angular correlation of e^+e^- pairs with $E_{\text{sum}} \in [16, 20]$ MeV measured in the ${}^7\text{Li}(p, e^+e^-){}^8\text{Be}$ reaction with proton beam energies 500 and 1080 keV. The 500 keV dataset is fitted with Monte Carlo of both the IPC deexcitation and the EPC produced by gammas [23].

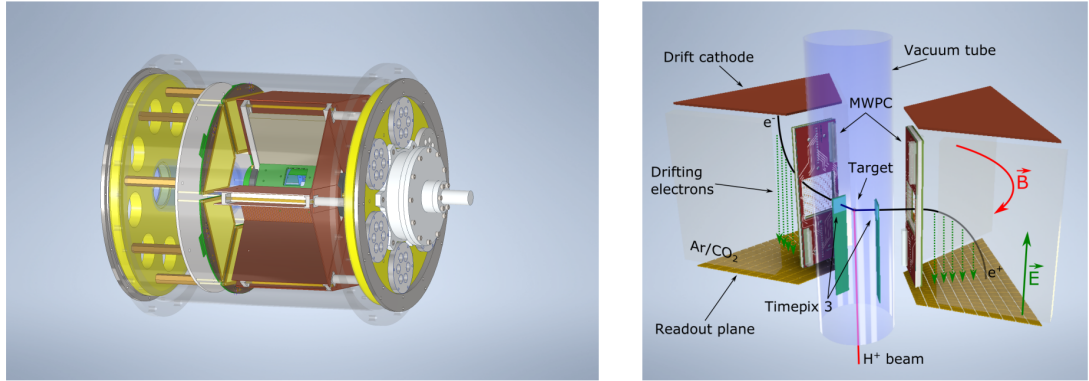


Figure 0.4: Schematics of the detector at the Van der Graaff facility at IEAP CTU (ref.).

172 0.2 X17 Project at IEAP CTU

173 The aim of the X17 project at the Van der Graaff facility of the Institute of
 174 Experimental and Applied Physics, Czech Technical University in Prague is to
 175 reproduce the results of the original ATOMKI experiments with ${}^7\text{Li}$ and ${}^3\text{H}$ tar-
 176 gets using an independent e^+e^- spectrometer. In order to effectively measure the
 177 anomaly, we need to reconstruct both the energy and the angular correlation of
 178 the e^+e^- pairs. The spectrometer will use three layers of detectors to achieve this
 179 – Timepix3 (TPX3) silicon pixel detector and Multi-Wire Proportional Cham-
 180 ber (MWPC) layers for the angle reconstruction and a Time Projection Cham-
 181 ber (TPC) layer for the energy reconstruction. The schematics of the prepared
 182 detector is in Fig. 0.4 Spectrometer CAD drawing (coordinates here or next chap-
 183 ter?). Cite some VdG paper, mention grant? Using https://cernbox.cern.ch/pdf-viewer/public/rf0oU1nqVLN3acZ/LuzH_submitted.pdf.

185 The energy of e^+e^- pair produced in the reaction is given by the energy

available E_r in the reaction and can be distributed between them arbitrarily. Nonetheless in the decay of the hypothetical X17 particle, electron and positron should have similar energy and we can therefore use a cut $|y| \leq 0.5$ in the disparity parameter (defined in Equation 0.1 **it was already used in ATOMKI figure captions, that's why it is defined prior to this**). Interesting events should rarely have a particle with an energy below $E_r/4$ (roughly 4 MeV). Electrons with such low energies are scattered significantly by even a thin layer of relatively light material, for this reason the TPX3 layer will be inside of the vacuum tube and the tube will have a thinned aluminum segment or KaptonTM windows.

TPX3 can measure (in each $55 \times 55 \mu\text{m}$ pixel of its 256×256 grid) time-of-arrival (ToA) with 1.6 ns precision and time-over-threshold (ToT) which reflects the deposited energy. This potentially allows 3D tracking if we increase the chip thickness at the cost of increased scattering. The layer can reconstruct the reaction vertex and the angular correlation with high precision.

The layer of MWPCs with sensitive area $40 \times 38 \text{ mm}^2$ will be outside of the beam pipe. It will provide an extra point on the particle trajectory which can help with the estimation of the reaction vertex and improve the TPC performance by providing its entry point.

The TPCs that are the subject of this thesis, are in a magnetic field generated by permanent magnets positioned between them and provide 3D track reconstruction and subsequent momentum and particle identification (its charge, or even type based on its stopping power). They avoid radiative losses thanks to the low density and atomic number of the gas mixture. For the readout, triple Gas Electron Multiplier (GEM) will be used. The magnetic field layout in our TPCs is atypical – orthogonal to the electric field inside the chamber, this is why we call them Orthogonal Fields TPC (OFTPC). Further details about our OFTPCs are provided in section 1.4.

1. Time Projection Chamber

A Time Projection Chamber (TPC) is a gaseous detector that uses the drift times of ionization electrons produced by a charged particle in an (ideally uniform) electric field to reconstruct the particle's 3D trajectory. The 2D projection is measured by an amplification stage at the end of the drift volume. When placed inside a magnetic field (typically parallel to the electric field), the momentum of the incident particle can be inferred from the curvature of its trajectory. Particle identification is also possible using the ionization energy loss inside the TPC (see Fig. 1.1). The following text (including Secs. 1.1 and 1.3) is based primarily on the reviews by Hilke [24] and the Particle Data Group [25].

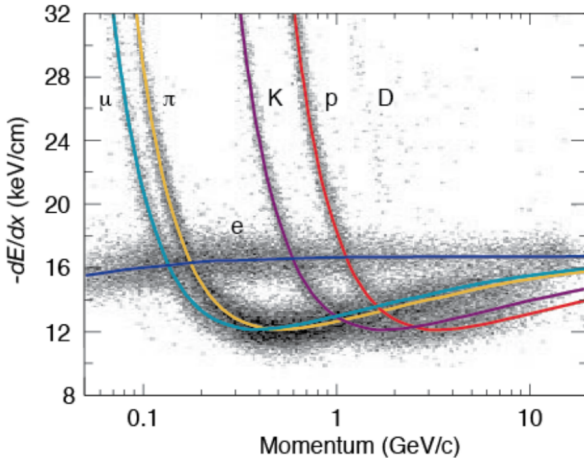


Figure 1.1: Particle identification in the PEP-4 TPC at SLAC based on the energy loss per distance $\frac{dE}{dx}$ in the 80:20 Ar:CH₄ filling at 8.5 atm pressure [26]. The reference doesn't point to the original PEP-4 article because this adapted version of the original picture that they used in the DUNE article looks better.

Large TPCs are sensitive to small distortions in the electric field (imperfections in the field cage, accumulation of positive ions in the gas volume) and to $\mathbf{E} \times \mathbf{B}$ effects on the drift velocity (see Eq. 1.1 below). Diffusion of the drifting electrons deteriorates the spacial resolution significantly, but it can be reduced up to ~ 10 times by a strong $\mathbf{B} \parallel \mathbf{E}$ field (see Eq. 1.8).

In neutrino and other rare-event experiments, large (up to 600 tons) Liquid Argon TPCs (LArTPCs) are used for particle identification and calorimetry. The ionization electrons can be drifted for many meters with a small diffusion. Scintillation photons are also measured. Negative ions?

1.1 Charge transport in gases

When a charged particle crosses the volume of a TPC, it loses energy by excitation and ionization of the detector gas (how much – from dE/dx + density → footnote?). Most ionizing collision produce a single ionization electron, sometimes a few secondary electrons are produced near the collision vertex, creating a cluster. In rare cases, the ionization electron has energy large enough to create

238 a measurable track, such an electron is called a δ -electron (terminology, just like
239 bellow – technically it's a (primary) ionization electron causing other (secondary)
240 ionization).

241 After their release, the ionization electrons are separated from positive ions
242 by the electric field and they both drift and diffuse in opposite directions towards
243 the electrodes. The charges are accelerated (different word?) by the electric field
244 inside the chamber, and they lose speed by colliding with the gas particles, quickly
245 reaching a constant (for a given field \mathbf{E}, \mathbf{B}) mean drift velocity. The electrons can
246 be absorbed by electronegative impurities, such as halides, O_2 , and H_2O .

247 In mixtures with a noble gas component, if the excitation energy of the noble
248 gas is higher than the ionization potential of an admixture, more free electrons can
249 be produced through collisions of the gas particles (so-called Penning transfer)
250 and through absorption of emitted photons.

251 If the electric field is strong enough, the electrons can cause further ion-
252 ization and excitation of the gas, leading to the development of a Townsend
253 avalanche (ref).

254 1.1.1 Drift

255 In many gases (called "hot", e.g., Ar or CH_4), the drift velocity is much greater
256 than that of their thermal motion thanks to a high proportion of elastic collisions.
257 On the other hand, "cold" gases like CO_2 have a higher proportion of inelastic
258 collisions (e.g., thanks to the excitation of rotational and vibrational states) and
259 therefore much lower (value? magnitude (implied?)) drift velocity. Or maybe it
260 is not so simple, because slowing down the electrons inelastically into a certain
261 minimum of elastic scattering cross-section increases drift velocity? In case of
262 $\text{Ar}+\text{CO}_2$ this is clearly not the case for low electric fields, so maybe irrelevant
263 here (or is the effect opposite for small additions?).

264 The ions produced by the ionization lose a significant portion of their energy
265 during each collision since their mass is close to the mass of the gas particles (see
266 the source material – average energy loss during collision $\Delta E = \frac{2m_i M}{(m_i + M)^2}$, this
267 way it's more accurate). This, together with their large collision cross section,
268 makes their drift velocity much smaller (about three orders of magnitude) and
269 their energy is close to thermal. Since their momenta are not randomized to such
270 an extent during collisions, their diffusion is smaller (move this to the diffusion
271 subsection, reformulate).

272 The drift is also influenced by the magnetic field. Langevin derived a good
273 approximation for the drift velocity vector:

$$\mathbf{v}_d = \left(\frac{\mathbf{E}}{\|\mathbf{E}\|} + \omega\tau \frac{\mathbf{E} \times \mathbf{B}}{\|\mathbf{E}\| \|\mathbf{B}\|} + \omega^2\tau^2 \frac{\mathbf{E} \cdot \mathbf{B}}{\|\mathbf{E}\| \|\mathbf{B}\|} \cdot \frac{\mathbf{B}}{\|\mathbf{B}\|} \right) \frac{q\tau}{m(1 + \omega^2\tau^2)} \|\mathbf{E}\|, \quad (1.1)$$

274 where q is the charge of the particle, m is its mass, τ is the mean time between
275 collisions and $\omega = \frac{q}{m} \|\mathbf{B}\|$ is the Larmor frequency. For orthogonal fields $\mathbf{E} \perp \mathbf{B}$,
276 it can be shown that the magnetic field bends the direction of the drift by the
277 so-called Lorentz angle:

$$\tan \psi = -\omega\tau. \quad (1.2)$$

278 The drift of ions is only negligibly influenced by the magnetic field ($\omega\tau \sim 10^{-4}$
279 is small due to the low drift velocity – better (?) because it takes τ into account

280 and differs only by E/B ratio (if the magnetic contribution to the magnitude is
 281 small)). In a standard TPC, \mathbf{E} is parallel to \mathbf{B} and the influence of the magnetic
 282 field on the drift is minimal. Without magnetic field, we can write

$$\mathbf{v}_d = \frac{q\tau}{m} \mathbf{E} = \mu \mathbf{E}, \quad (1.3)$$

283 where μ is called charge mobility.

284 1.1.2 Diffusion

285 All of the theory is from the same source mentioned at the beginning. None of the
 286 simulations explicitly depend on this. Due to collisions, a cloud of electrons or
 287 ions originating from the same point will show a Gaussian density distribution at
 288 time t while drifting in the electric field $\mathbf{E} = (0, 0, E_z)$ along the z -coordinate (co-
 289 ordinates defined by the electric field):

$$\rho(x, y, z, t) = (4\pi Dt)^{-\frac{3}{2}} \exp\left(-\frac{x^2 + y^2 + (z - v_d t)^2}{4Dt}\right), \quad (1.4)$$

290 where the diffusion coefficient D can be expressed as

$$D = \frac{\lambda^2}{3\tau} = \frac{\lambda v_d}{3} = \frac{v_d^2 \tau}{3} = \frac{2\varepsilon\tau}{3m}, \quad (1.5)$$

291 where λ is the mean free path and ε the mean kinetic energy. The lateral diffusion
 292 width σ_x after a drift distance L can be expressed as

$$\sigma_x^2 = 2Dt = \frac{4\varepsilon L}{3qE_z}. \quad (1.6)$$

293 The minimal diffusion width is given by the lowest possible energy of the particles
 294 $\varepsilon_{\text{th}} = \frac{3}{2}kT$ (corresponding to thermal motion):

$$\sigma_{x, \text{min}}^2 = \frac{2kTL}{qE}. \quad (1.7)$$

295 For electrons in "cold gases" (e.g., Ar/CO₂ mixture), the diffusion approaches this
 296 limit up to a certain field intensity (~100 V/cm at 1 atm pressure)¹. In reality, the
 297 transversal diffusion of electrons can differ significantly from their longitudinal
 298 diffusion and simulations are necessary to get a precise result.

299 In most TPCs, the transversal (but not the longitudinal) diffusion is reduced
 300 by the magnetic field, since it is parallel to the electric field and curves the
 301 diffusing electrons around their mean trajectory:

$$\frac{D_T(B)}{D_T(0)} = \frac{1}{C + \omega^2 \tau_2^2}, \quad (1.8)$$

302 where C and τ_2 are parameters dependent on the gas used. At low intensity of
 303 the magnetic field, we can use an approximation $C \approx 1$ and $\tau_2 \approx \tau$.

¹For us $\sigma_{x, \text{min}} = 0.45$ mm, quite close to the actual diffusion 0.5-0.7 mm – details of the calculation.

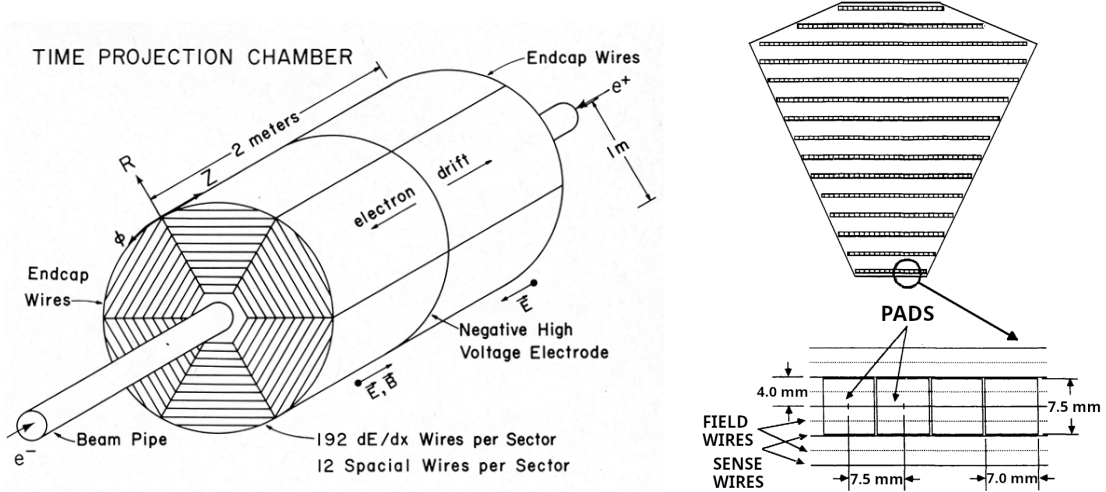


Figure 1.2: Schematic view of the PEP-4 TPC [28]. A charged particle produced in a collision in the beam pipe creates a spiral ionization track in the magnetic field. The central cathode then accelerates ionization electrons towards the endcap anode wires where they are multiplied and read out. A TPC sector with a detailed view of one of the pad rows is shown on the right [29].

304 1.2 Examples of TPCs

305 1.2.1 The original TPC at PEP-4 at SLAC

306 The original TPC used in the PEP-4 experiment at SLAC in the 1980s (Fig. 1.2)
 307 was a $2\text{ m} \times 2\text{ m}$ hollow cylinder with a central cathode that produced a strong
 308 electric field 750 V/cm , making the ionization electrons drift towards one of the
 309 endcaps [27]. It was filled with a 80:20 Ar:CH₄ mixture at 8.5 atm pressure
 310 and placed inside a 0.4 T solenoidal magnetic field. The readout consisted of
 311 MWPCs, where electrons are accelerated towards the anode wires fast enough to
 312 further ionize the gas and cause an avalanche (details are provided in Sec. 1.3.1).
 313 The wires had radial spacing 4 mm, fifteen of the sense wires had the cathode
 314 segmented into $7.0 \times 7.5\text{ mm}^2$ pads 4 mm under them (Fig. 1.2 right). When
 315 collecting electrons on the anode wire, signal is induced on the nearest 2-3 cathode
 316 pads.

317 1.2.2 ALICE TPC

318 The ALICE TPC (Fig. 1.3) is the main detector used for charged particle tracking
 319 and recognition in collisions at the ALICE experiment at the CERN LHC [30].
 320 Similarly to PEP-4, it is a hollow cylinder with outer radius 2.5 m and height 5 m.
 321 It is placed in a 0.5 T solenoidal magnetic field, and the central cathode generates
 322 a 400 V/cm electric field inside the field cage. The gas mixture in the detector
 323 is 90:10:5 Ne:CO₂:N₂, mainly chosen for its higher ion mobility compared to Ar
 324 mixtures. In 2020, the readout of the TPC was upgraded from MWPCs to stacks
 325 of four GEM foils (principle described in Sec. 1.3.2). This allows reading events
 326 continuously at a higher rate.

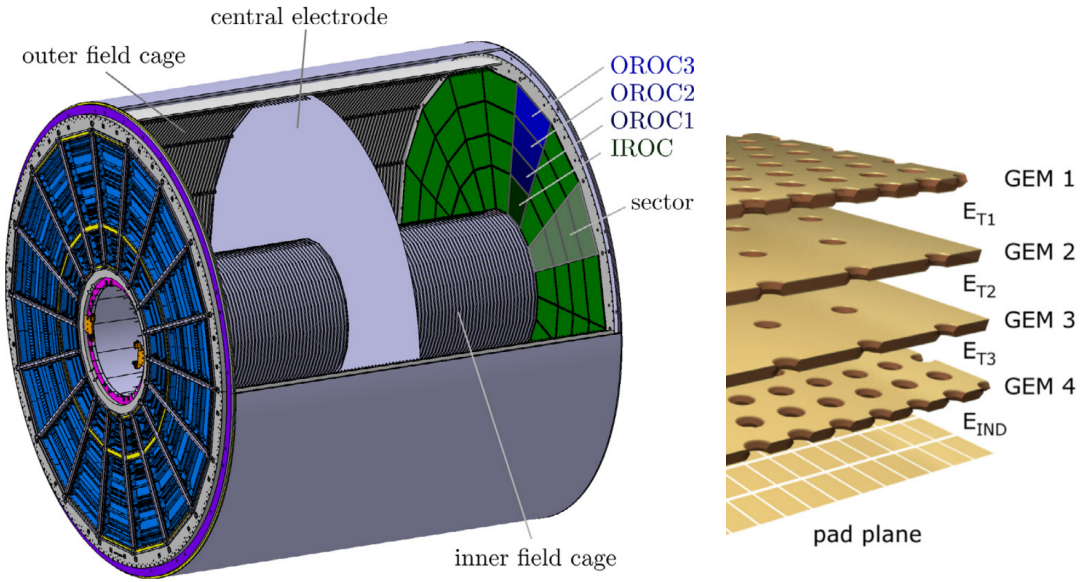


Figure 1.3: Schematic view of the ALICE TPC [31]. The readout at each endcap is divided into 18 sectors, each subdivided into an Inner Readout Chamber (IROC) with one GEM stack and Outer Readout Chamber (OROC) with three GEM stacks. A visualization of a GEM stack is on the right [32].

327 1.2.3 CERES/NA45 radial-drift TPC

328 In 1998, the CERES/NA45 (Cherenkov Ring Electron Spectrometer) experiment
 329 (Fig. 1.4) at the CERN SPS was upgraded with the first radial-drift TPC (rTPC)
 330 to achieve a higher momentum resolution [33]. Unlike a standard TPC, the elec-
 331 tric field 600–200 V/cm was arranged radially with the magnetic field (inhomoge-
 332 neous, up to 0.5 T) by two solenoidal coils with opposite polarity. The outward
 333 drift of the ionization electrons is affected by the crossing fields as shown in Eq. 1.1
 334 and the drift velocity is not uniform due to the varying electric field. The rTPC
 335 was filled with an 80:20 Ne:CO₂ gas mixture, which has relatively small diffu-
 336 sion coefficients and Lorentz angle. The readout was handled by conventional
 337 MWPCs (Fig. 1.5).

338 The field configuration in an rTPC enables a larger number of pads compared
 339 to a standard TPC, leading to improved spatial resolution and possibility of larger
 340 multiplicity rates. Since the drift time is lower, the detector is faster.

341 After an algorithm described in this thesis was developed for our OFTPCs at
 342 IEAP CTU, we noticed the similarities with the approach used by the CERES/NA45
 343 rTPC, when accounting for the transport process of charged clusters in the com-
 344 plex fields. The detector hit coordinates (pad, time, and plane) were transformed
 345 using look-up tables. The tables were calculated using a Runge-Kutta method to
 346 integrate the Langevin approximation of the drift velocity (Eq. 1.1). The drift
 347 velocity in the radial field was calibrated using seven parallel laser rays. This
 348 calibration was then used to make a correction compared to the MAGBOLTZ
 349 Monte Carlo drift [34]. **Measured mobility differs significantly from MAGBOLTZ,**
 350 **but this might be improved in the newer versions?** The tracks were fitted using
 351 reference tables with hit coordinates of tracks simulated with GEANT Monte
 352 Carlo (**not such a big problem for us right now, might be an idea if the recon-**

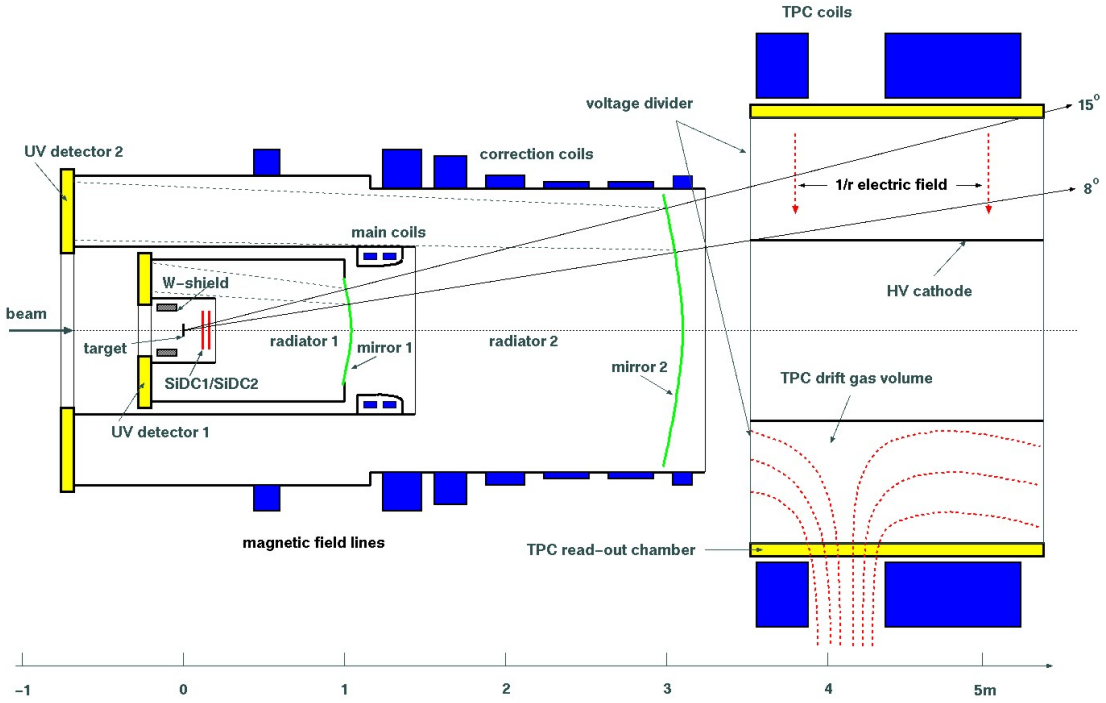


Figure 1.4: Experimental setup of the CERES/NA45 experiment with two Ring Imaging Cherenkov Counters (RICHs) on the left and a rTPC on the right. The magnetic field (red) is generated by two solenoidal coils (blue) with opposite polarity. Produced ionization electrons drift outward radially towards the readout chamber (yellow) [33].

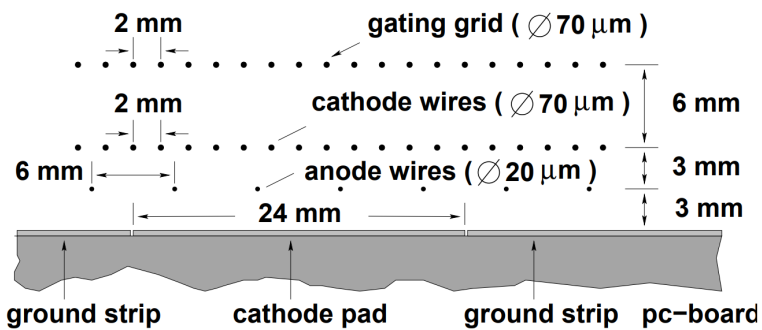


Figure 1.5: Cross section of a CERES/NA45 readout MWPC. The wires are stretched in the azimuthal direction above the pad plane. The gating grid controls the passage of electrons and ions. [33].

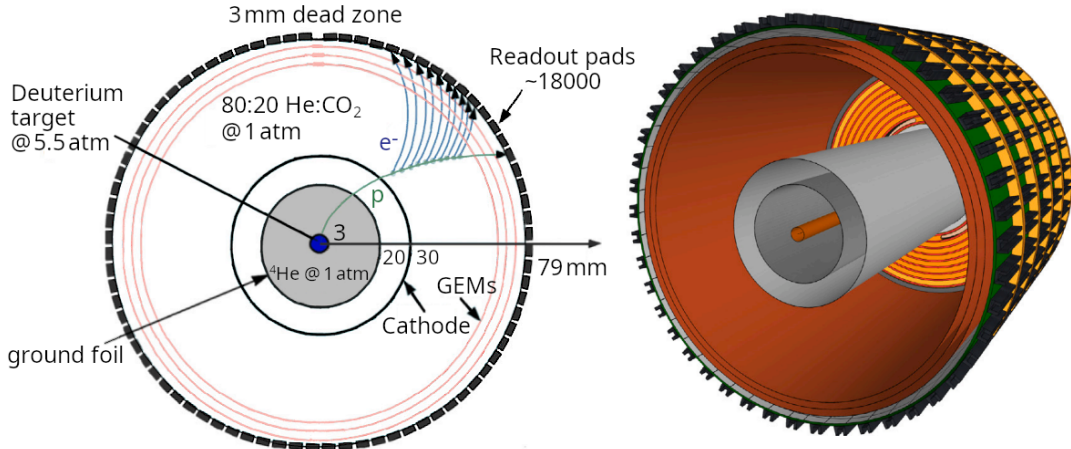


Figure 1.6: Schematic view of the BONuS12 rTPC [35].

353 red struction gets too slow).

354 1.2.4 Other interesting radial-drift TPCs

355 muEDM at PSI: [https://arxiv.org/pdf/2307.01535](https://arxiv.org/pdf/2307.01535.pdf),

356 FTPC at STAR at RHIC: [https://arxiv.org/pdf/nucl-ex/0211014](https://arxiv.org/pdf/nucl-ex/0211014.pdf)

357 BONuS12 rTPC

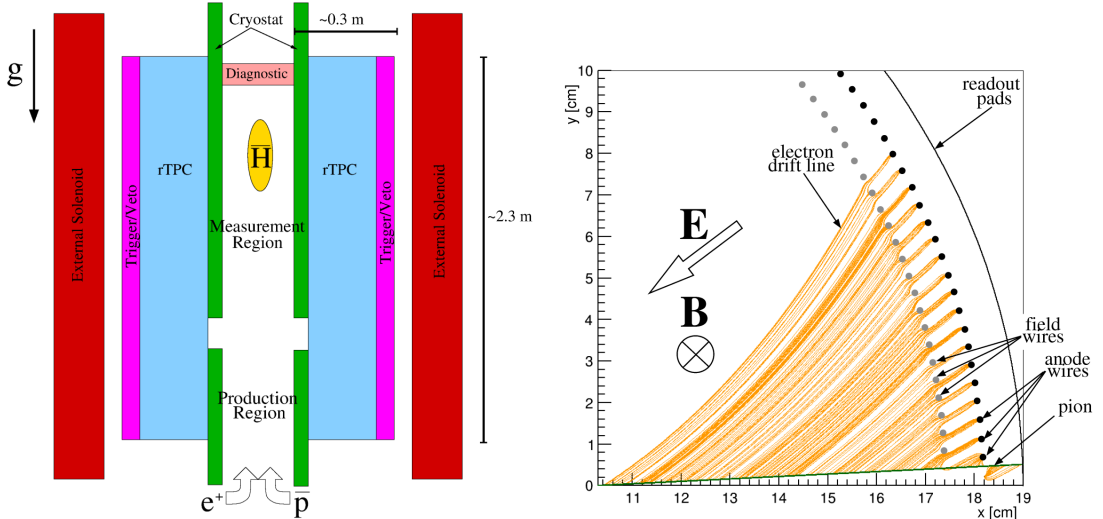
358 In 2020, the Barely Off-shell Neutron Structure 12 GeV (BONuS12) experiment
 359 used an rTPC (Fig. 1.6) to measure low-momentum spectator protons produced
 360 in $e^-d \rightarrow e^-p_sX$ scattering [35]. It was filled with a 80:20 He:CO₂ gas mixture and
 361 placed inside a 4 T solenoidal magnetic field, perpendicular to the radial electric
 362 field (1100 V/cm on average), tilting the drift (see Eq. 1.2). The amplification
 363 used cylindrical triple GEM stacks.

364 Garfield++ simulations and study of reconstructed tracks have shown that the
 365 radial component of the drift velocity almost proportional to the radial electric
 366 field, and the r -coordinate can be reconstructed using an analytical formula. Sim-
 367 ilarly, the azimuthal component is nearly proportional to the radial component,
 368 resulting in a largely constant Lorentz angle between the radial and actual direc-
 369 tion, and the ϕ -coordinate can be solved analytically. The remaining z -coordinate
 370 stays undistorted. The momentum is determined by fitting tracks with a helix,
 371 while accounting for the energy losses (the small variability of magnetic field along
 372 the z -axis has a negligible effect).

373 ALPHA-g rTPC

374 In 2023, the Antihydrogen Laser Physics Apparatus (ALPHA) collaboration pub-
 375 lished results of measurements of antihydrogen (\bar{H}) annihilation² after release
 376 from magnetic confinement, showing that it behaves in a way consistent with grav-
 377 itational attraction to the Earth [36]. They used a 2.3 m long rTPC (Fig. 1.7a)

²The main \bar{p} annihilation mode is into several π^\pm and π^0 , only the π^\pm tracks are long enough to be reconstructed. The scattering of π^\pm is not negligible, and photons from π^0 decay create e^+e^- pairs as background.



(a) Sketch of ALPHA-g. Antiprotons and positrons are injected from the bottom and form \bar{H} in a Penning trap while being cooled by the cryostat (green). The annihilation is reconstructed by the rTPC (blue).

(b) Cross section view of the rTPC (Garfield++ simulation). The electrons (orange) produced by a pion track (green) drift towards the anode wires, while influenced by the axial magnetic field. The size of the field and anode wires is exaggerated.

Figure 1.7: Schematic view of the ALPHA-g detector [37].

with a 40 cm outer and 20 cm inner diameter in a 1 T solenoidal magnetic field, and filled with an Ar/CO₂ mixture [37]. The readout consists of an MWPC (Fig. 1.7b). The radial confinement of the cold \bar{H} is achieved with a superconducting octupole magnet, the axial with a set of so-called *mirror* coils.

The *r*-coordinate of the ionization cluster is reconstructed from the drift time using a tabulated space-time relation. The 3D position of the interaction (cluster) vertex is obtained by matching the wires and pads by drift time using a k-d tree algorithm. Reconstructed tracks are fitted with a helix using the least squares method [38].

1.3 Readout

1.3.1 Multi-Wire Proportional Chamber

In most TPCs operated in experiments, Multi-Wire Proportional Chamber (MWPC) was used for the readout (Fig. 1.8). The electrons enter the chamber through a cathode grid and get accelerated by a strong electric field towards the parallel, thin anode wires and create an avalanche, multiplying the signal. The trajectory can be reconstructed from the drift time and two coordinates measured using

- a) two segmented cathodes (wires or strips) rotated by 90° or
- b) the ratio of charge collected on two sides of the hit resistive wires.

For high counting rates, the positive ions from the avalanches accumulate, creating a space charge that distorts the electric field. This can be solved by using a gating grid near the readout plane to collect these ions at the cost of introducing a dead time in the detector.

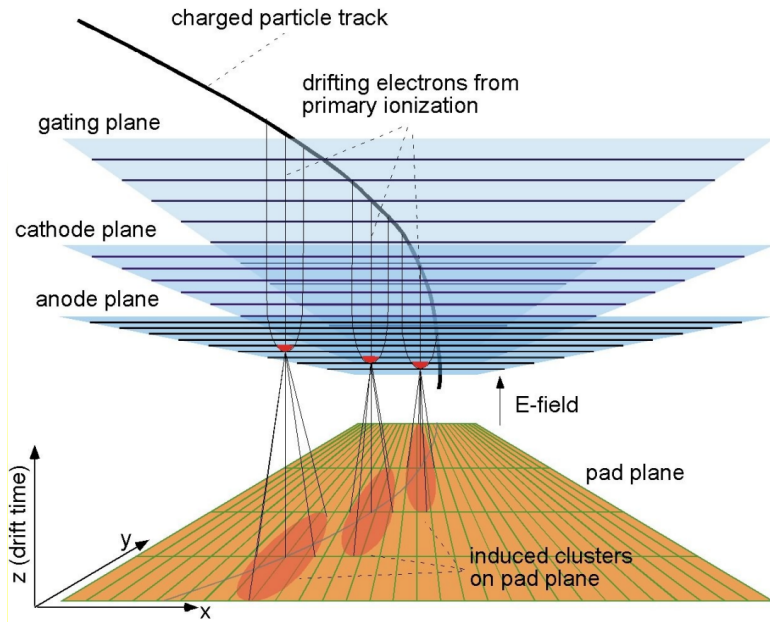


Figure 1.8: Schematic view of the ALICE MWPC readout (working principle) [39].

400 1.3.2 Micro-Pattern Gaseous Detectors

401 In order to avoid MWPC limitations (e.g., diffusion, wire $\mathbf{E} \times \mathbf{B}$ effect, space
 402 charge effects), a family of Micro-Pattern Gaseous Detector (MPGD) technologies
 403 are being developed. The readouts can reach higher spatial resolution (down to
 404 30 μm) with faster response time (ns range) and much higher rate capability.

405 Gas Electron Multiplier

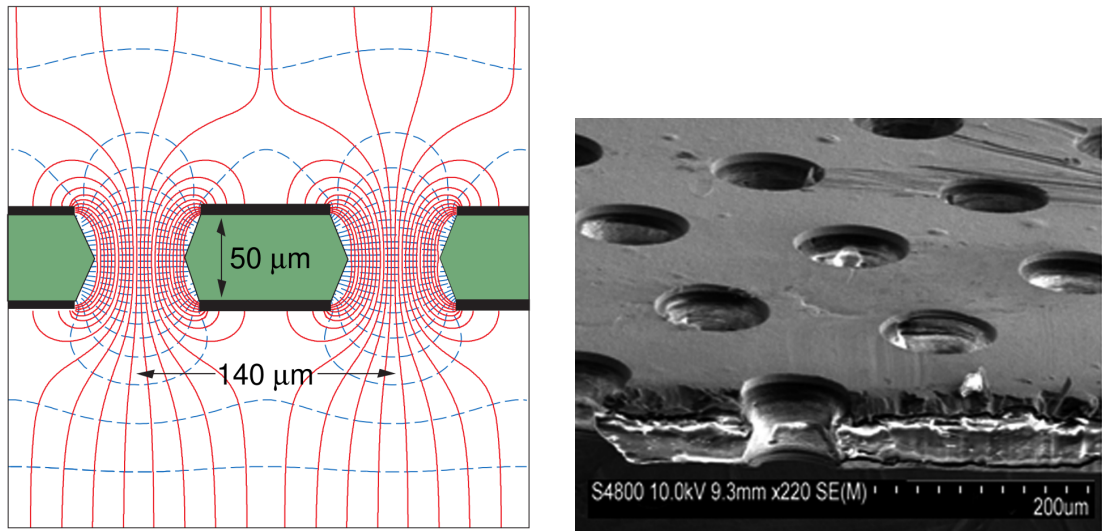
406 A Gas Electron Multiplier (GEM) is a thin metal-coated polyimide sheet with
 407 a dense pattern of small, chemically etched holes (Fig. 1.9). The amplification is
 408 achieved by applying voltage across the metal layers and placing the foil between
 409 two moderate uniform electric fields. This creates a strong electric field inside the
 410 holes that accelerates the incoming electrons and causes avalanches (see Fig. 1.10).
 411 Some charges may land on the dielectric surfaces due to diffusion, modifying the
 412 field and affecting gain.

413 Double or triple stacks of GEMs are usually used to create a sufficient gain
 414 while maintaining stability (reducing discharges). From the last foil, the electrons
 415 drift to a segmented anode where the signal is read. The ion backflow is reduced
 416 compared to MWPC.

417 A cheaper alternative (especially for large area coverage) is a THick GEM
 418 (THGEM) with a \sim 10-fold upscaling of geometrical parameters. It can be made
 419 by mechanically drilling holes into a standard Printed Circuit Board (PCB) and
 420 creating a circular rim around the holes by etching the metal coating.

421 Micromegas

422 In a MICRO-MEsh GAseous Structure (Micromegas) (in sources I viewed it is not
 423 capitalized) electrons pass through a fine mesh (made out of very thin wires) into



(a) A schematic view of a GEM cell with its typical dimensions, electric field lines (red), and equipotentials (blue) [25].

(b) A scanning electron microscope image of a GEM foil [40].

Figure 1.9: Gas Electron Multiplier (GEM).

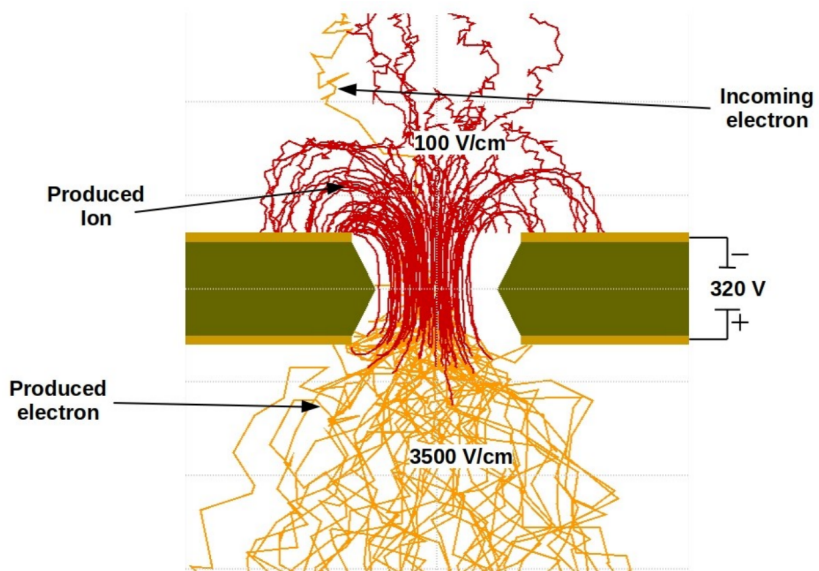
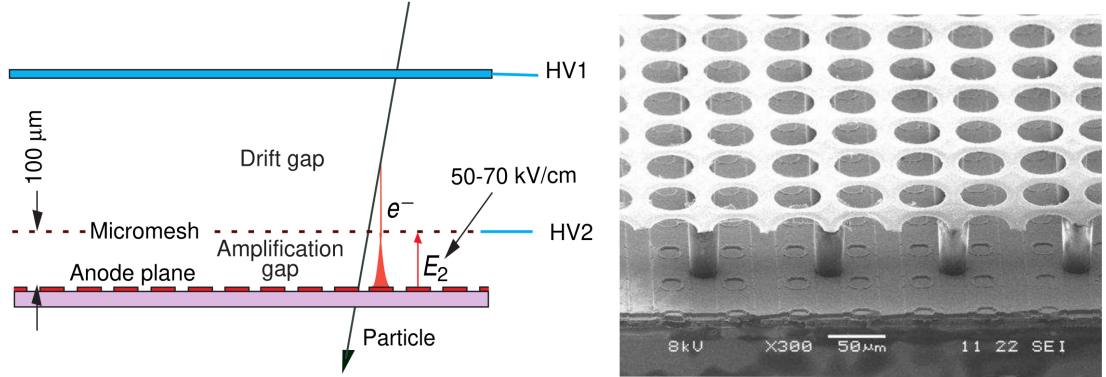


Figure 1.10: Garfield simulation of an avalanche in a GEM hole [41]. An incoming electron (orange) is accelerated in the strong electric field of the GEM and causes further ionization multiplying the number of free electrons (orange). Most of the produced cations (red) are captured by the GEM cathode.



(a) A schematic view of a Micromegas detector.

(b) A scanning electron microscope image of a Micromegas "GridPix" detector.

Figure 1.11: MICRO-MEsh Gaseous Structure (Micromegas) [25].

a narrow amplification gap where they are multiplied in the high field and read as a signal on the segmented anode (Fig. 1.11a). Very high field ($30-80 \text{ kV/cm}^2$) is necessary to achieve sufficient gain. Ion backflow is heavily suppressed by the mesh.

A Timepix chip (a high granularity pixel detector) can be used for the readout anode to achieve the best spatial resolution, making an integrated readout called GridPix (Fig. 1.11b). Thanks to the high spatial resolution, it is possible to distinguish individual electron clusters, which enables a new method of particle identification.

Other MPGDs

A Resistive Plate WELL (RPWELL) consists of a THGEM with only the top side metal-coated, mounted on a resistive film deposited on a thin isolating sheet (which is read out similarly to a Resistive Plate Chamber (RPC)). Due to the higher field in the closed holes of the THGEM, a higher gain can be reached for the same voltage. A Micro-RWELL (μ -RWELL) is a similar architecture with ~ 7 times smaller pitch (distance between holes). These options provide a better spark resistance and could allow to cover large areas for a lower cost.

A Micro-Pixel Gas Chamber (μ -PIC) is a PCB with anode strips on one side and orthogonal cathode strips on the other. The cathode has a resistive coating and a regular pattern of uncoated regions with anode "dots" penetrating the PCB at the centers.

1.4 Orthogonal Fields TPC at IEAP CTU

At IEAP CTU, we are going to use six identical atypical TPCs with inhomogeneous toroidal magnetic field **orthogonal** to the electric field (details below), hereafter referred to as Orthogonal Fields TPC (OFTPC). It has the shape of isosceles trapezoidal prism 16 centimeters high with triple-GEM readout on one of its bases. Dimensions of the OFTPC are discussed in detail in section 1.4.2 below. Throughout this thesis, we assume a uniform electric field along the z axis with $E_z = -400 \text{ V/cm}$. Isn't the field affected by the MWPCs? Eventually a sim-

ulation will be needed. Measured particles enter the OFTPC through a window after crossing the MWPC. Gas mixture used in the detector (70/30) and its effect – some graph with the mixture, reasons for the choice. Add a figure of the real TPC. More about the design choices.

1.4.1 Motivation and Associated Challenges

The reasons for the unusual field layout are mostly cost related:

- a) we use permanent magnets instead of a solenoid and parallel fields are difficult to accomplish this way,
- b) granularity of the TPC readout is limited in order to fit one SAMPA/SRS hybrid in each sector – parallel fields would bend the trajectories parallel to the readout requiring more pads and different architecture.

In this thesis, we will show that such a setup can reach a similar energy resolution as common cylindrical TPCs while reducing the overall cost.

The layout introduces two complications to the track reconstruction – the trajectory in inhomogeneous field is not circular and the drift is distorted by the magnetic field as shown in the Equation 1.1(in our case $\omega\tau \approx 0.08$ for 0.3 T assuming $\mu \approx 0.25$ T⁻¹, varies inside the detector). We will deal with these effects in the upcoming chapters.

The diffusion in such setup is larger since parallel orientation reduces diffusion by curling the electrons in the x - y direction (see Equation 1.8), but for our relatively weak magnetic field and short drift distance, the difference is negligible.

1.4.2 Coordinate Systems and Dimensions

In order to describe events in our detector, we use three distinct spaces: the detector space \mathcal{D} , the readout space \mathcal{R} and the pad space \mathcal{P} (different spaces that describe different things and each has their own coordinate system, so maybe rename the section somehow?). Each space is later used to represent ionization electrons at different stages of the detection process: their creation in the gas, their final position when hitting the readout plane, and finally their representation in the discrete pad space.

Detector Space

The detector space \mathcal{D} represents the physical space of our detector. We describe it using Cartesian coordinates (x, y, z) . The z -axis is the detector's axis of symmetry, with its negative direction aligned with the proton beam. The origin $(0, 0, 0)$ is located at the center of the irradiated target. The positive x -axis passes through the center of one the OFTPCs along the intersection of its two planes of symmetry. The y -axis is then chosen to maintain a right-handed coordinate system.

Since the detector has a hexagonal symmetry, we use only one of its sectors in this work – the first sector $\mathcal{D}_1 \subset \mathcal{D}$ which is defined by the condition:

$$(x, y, z) \in \mathcal{D}_1 \Leftrightarrow |y| \leq x \tan \frac{\pi}{6}. \quad (1.9)$$

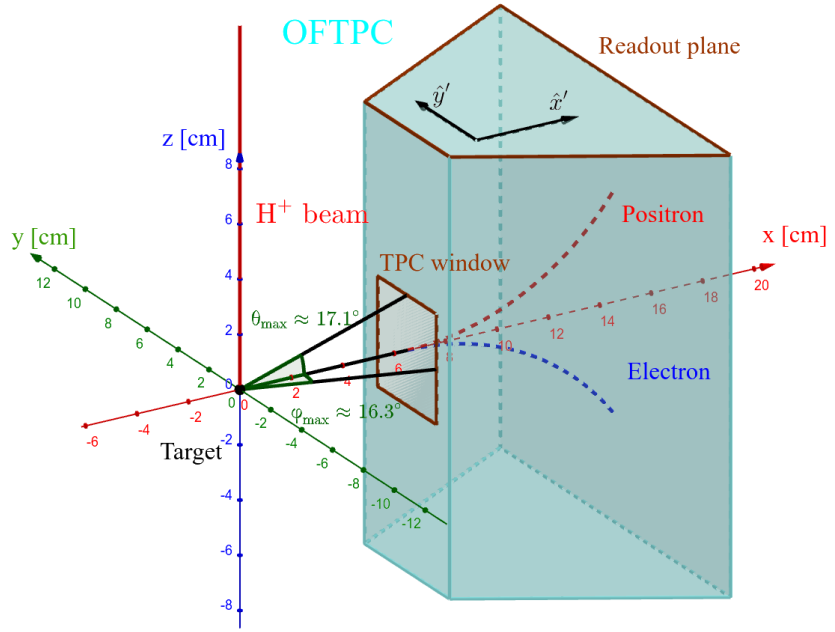


Figure 1.12: Schematics of the first sector OFTPC with detector space coordinates.

492 Simulations in this sector can be applied to all sectors by rotating the coordinates
 493 accordingly. The volume of the OFTPC in this sector, which has the shape of
 494 a trapezoidal prism, has these boundaries:

$$x \in [x_{\min}, x_{\max}] = [6.51, 14.61] \text{ cm}, \quad (1.10)$$

$$z \in [z_{\min}, z_{\max}] = [-8, 8] \text{ cm}, \quad (1.11)$$

$$y_{\max}(x_{\min}) = -y_{\min}(x_{\min}) = 2.75 \text{ cm}, \quad (1.12)$$

$$y_{\max}(x_{\max}) = -y_{\min}(x_{\max}) = 7.45 \text{ cm}, \quad (1.13)$$

495 where $y_{\max}(x)$ is the maximal value of the y -coordinate for a given x . The read-
 496 out is located at $z = 8$ cm; for some purposes, we also define the distance to
 497 the readout $d_r = 8 \text{ cm} - z$ as an alternative to the z -coordinate. **Keeping this**
 498 **paragraph as it is because the OFTPC volume is distinct from the first sector**
 499 **and some parts of this thesis use the space beyond this volume.** The OFTPC
 500 window has width 3.8 cm and height 4.0 cm.

501 We also use spherical coordinates (r, θ, φ) with the elevation angle θ measured
 502 relative to the xy plane. Angles θ and φ are useful when describing the direction
 503 of e^+/e^- tracks. Their maximal values considered for the initial direction in
 504 simulations are $\theta_{\max} \approx 17.1^\circ$ and $\varphi_{\max} \approx 16.3^\circ$ as shown in Fig. 1.12.

505 Readout Space

506 The readout space \mathcal{R} represents the drift time and final positions of ionization
 507 electrons as measured by an ideal continuous readout. We describe it using
 508 coordinates (x', y', t) , where x' and y' correspond to the detector coordinates at
 509 the readout plane ($z = 8$ cm).

510 Currently not entirely sure how to put this into a figure since only x' and
 511 y' correspond to the detector coordinates, it will make more sense when

512 **visualizing the map.** The drift time t is approximately proportional to d_r .

513 Pad Space

514 The pad space \mathcal{P} represents the time bin and pad number of ionization electrons
515 as measured by an ideal discrete readout:

$$\mathcal{P} = \{(n_{\text{pad}}, n_t) \in \mathbb{N}^2 \mid n_{\text{pad}} \leq 128\}. \quad (1.14)$$

516 **Rewrite to reflect this:** Technically both values can be zero as defined in the
517 code (max channel 127). It is not really a subspace of \mathcal{R} but there is a mapping
518 from \mathcal{R} to \mathcal{P} . It is a discretization of a part of \mathcal{R} , the mapping can be adjusted
519 depending on the simulation. If we assume uniform electric field there will be
520 gaps, we don't use gaps in the reconstruction since the electrons should be pulled
521 towards the pads.

522 The readout of the OFTPC will consist (is the design final?) of 128 rectangular
523 pads arranged in a staggered pattern. Parameters of the pad layout are shown
524 in Fig. 1.13. The bottom left corner of n -th pad has coordinates $(x_{1,n}, y_{1,n})$, the
525 top right $(x_{2,n}, y_{2,n})$ and its center has coordinates $(x_{c,n}, y_{c,n})$. The gap between
526 neighboring pads is $g = 0.08$ cm. Time will be read out in discrete bins of size
527 $t_{\text{bin}} = 100$ ns (details?). Could also describe pad-related functions.

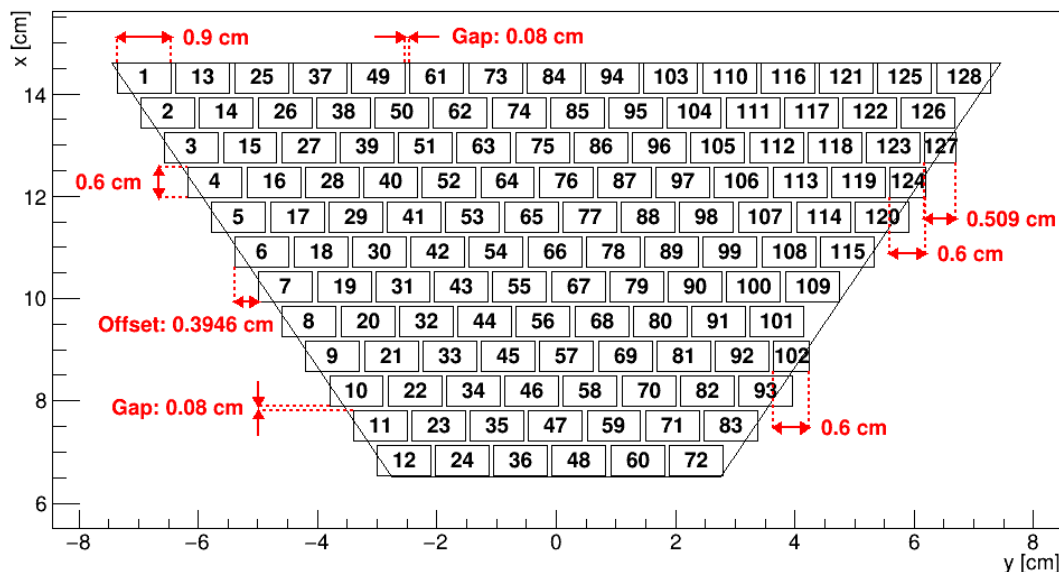
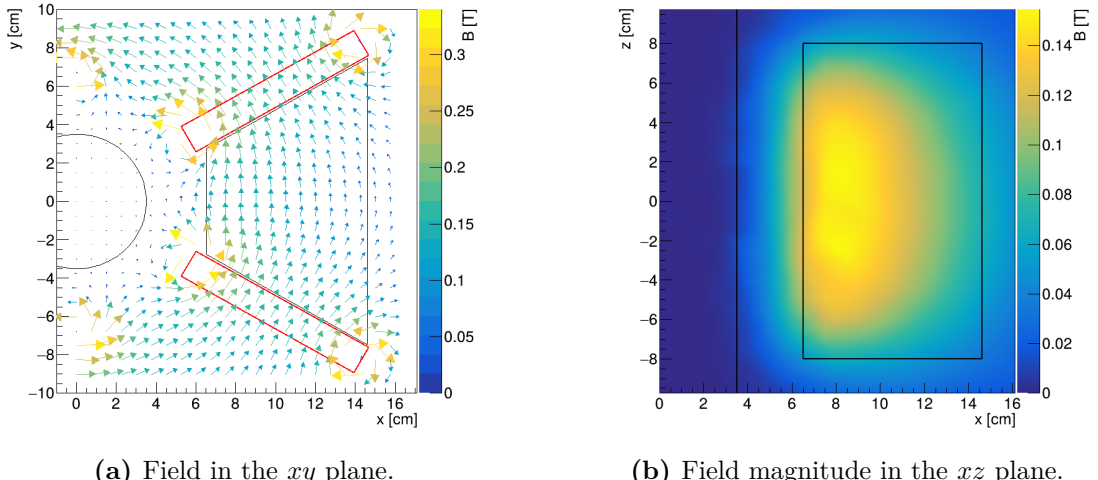


Figure 1.13: Pad layout of the OFTPC and its parameters. Pads 102, 124 and 127 are irregular, the rest has the same dimensions.

528 1.4.3 Magnetic Field Simulation

529 The magnetic field inside our detector is produced by six permanent magnets. It
530 was simulated using Ansys Maxwell (citation) which gives us values on a regular
531 grid. More details, vacuum tube, magnets (homogeneous?, density?). Visualization
532 of the magnetic field is shown in Fig. 1.14. Whenever we need to work with
533 values outside this grid, we use trilinear interpolation described below.



(a) Field in the xy plane.

(b) Field magnitude in the xz plane.

Figure 1.14: Magnetic field simulation results. The OFTPC volume and the vacuum tube are marked with black lines, the magnets are marked with red lines. **The coordinates of the magnets from the CAD drawing seem to be 9/10 of the ones from the magnetic simulation (fixed, the magnetic simulation parameters are off).**

534 Trilinear Interpolation

535 Trilinear interpolation is a 3D generalization of linear interpolation³. It can be
 536 used to interpolate a function whose values are known on a regular grid with
 537 rectangular prism cells. We use this simple method for interpolating the magnetic
 538 field, and it is later used in Section 3.2.2 to interpolate the Ionization Electron
 539 Map, a key component of our track reconstruction algorithm. In both cases, we
 540 use a regular cubic grid (apparently it is also called a Cartesian grid).

541 Let us consider a cell of our regular grid (a cube) with an edge of length a
 542 containing the point $\mathbf{C} = (x, y, z)$ where we want to interpolate a function
 543 $f: \mathbb{R}^3 \rightarrow \mathbb{R}$. We know the values of this function at the vertices of the cell
 544 $\mathbf{C}_{ijk} = (x_0 + ia, y_0 + ja, z_0 + ka)$, where $\mathbf{C}_{000} = (x_0, y_0, z_0)$ is the origin of the
 545 cell (is that clear?), and $i, j, k \in \{0, 1\}$ are indices. We also define the points $\mathbf{C}_{ij} =$
 546 $= (x, y_0 + ia, z_0 + ja)$ and $\mathbf{C}_i = (x, y, z_0 + ia)$. Then the interpolated value $\hat{f}(\mathbf{C})$
 547 can be calculated as a composition of three linear interpolations (see Fig. 1.15):

$$\hat{f}(\mathbf{C}_{ij}) = (1 - x_d) f(\mathbf{C}_{0ij}) + x_d f(\mathbf{C}_{1ij}), \quad (1.15)$$

$$\hat{f}(\mathbf{C}_i) = (1 - y_d) \hat{f}(\mathbf{C}_{0i}) + y_d \hat{f}(\mathbf{C}_{1i}), \quad (1.16)$$

$$\hat{f}(\mathbf{C}) = (1 - z_d) \hat{f}(\mathbf{C}_0) + z_d \hat{f}(\mathbf{C}_1), \quad (1.17)$$

548 where x_d , y_d , and z_d are given as follows:

$$x_d = \frac{x - x_0}{a}, \quad y_d = \frac{y - y_0}{a}, \quad z_d = \frac{z - z_0}{a}. \quad (1.18)$$

³Linear interpolation in point $x \in (x_1, x_2)$ of a function $f: \mathbb{R} \rightarrow \mathbb{R}$ known in points $x_1 < x_2$ is the convex combination $\hat{f}(x) = (1 - x_d)f(x_1) + x_d f(x_2)$, where $x_d = \frac{x - x_1}{x_2 - x_1} \in (0, 1)$.

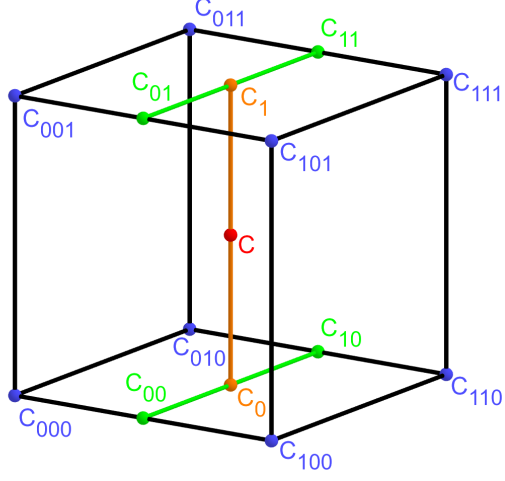


Figure 1.15: Visualization of trilinear interpolation as a composition of linear interpolations (inspired by [42]). We want to interpolate the value in the red point \mathbf{C} . First we interpolate between the four pairs of blue points sharing the last two indices along the x -axis (Eq. 1.15), then between the two pairs of the resulting green points along the y -axis (Eq. 1.16) and finally between the two resulting orange points along the z -axis to get the final red value (Eq. 1.17).

549 We can also write

$$\hat{f}(\mathbf{C}) = \sum_{i,j,k \in \{0,1\}} t_x^i t_y^j t_z^k f(\mathbf{C}_{ijk}), \quad (1.19)$$

$$t_\alpha \stackrel{\text{def}}{=} \begin{pmatrix} t_\alpha^0 \\ t_\alpha^1 \end{pmatrix} = \begin{pmatrix} 1 - \alpha_d \\ \alpha_d \end{pmatrix}, \quad (1.20)$$

550 where $\alpha \in \{x, y, z\}$ is an index. This gives a nice geometric interpretation to the
 551 trilinear interpolation as shown in Fig. 1.16. From this form and the figure, it is
 552 apparent that the final interpolated value does not depend on the order of axes
 553 along which we perform linear interpolations (see Fig. 1.15). Furthermore, we
 554 can write $\hat{f}(\mathbf{C})$ as a polynomial:

$$\hat{f}(\mathbf{C}) = \sum_{\alpha, \beta, \gamma \in \{0,1\}} \sum_{i=0}^{\alpha} \sum_{j=0}^{\beta} \sum_{k=0}^{\gamma} (-1)^{(\alpha-i)+(\beta-j)+(\gamma-k)} f(\mathbf{C}_{ijk}) x_d^\alpha y_d^\beta z_d^\gamma. \quad (1.21)$$

555 We take advantage of this form when generalizing trilinear interpolation to irreg-
 556 ular grid in section 3.2.3.

557 Maybe a citation here, although I am not sure it is necessary since it could
 558 be considered common knowledge. The last two equations are my own (but I'm
 559 not sure that's worth mentioning unless there's a citation).

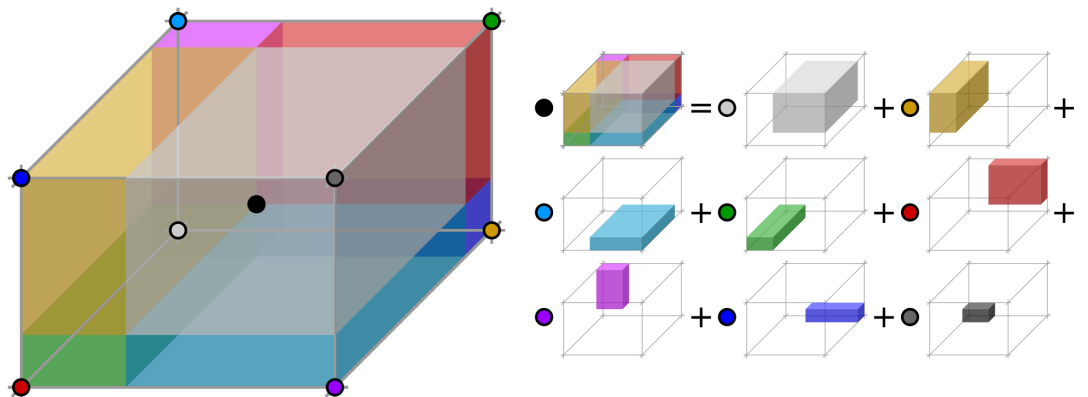


Figure 1.16: Geometric interpretation of trilinear interpolation as expressed in Equation 1.19. The colored dots represent the values in given points and the colored boxes represent the volume in the opposite corner by which the corresponding values are multiplied. The black dot represents the interpolated value which is multiplied by the entire volume [43].

560 2. Track Simulation

561 In order to develop and test the reconstruction algorithm, electron and positron
562 tracks are simulated inside the first detector sector \mathcal{D}_1 (see Section 1.4.2) with
563 different initial parameters (origin, initial direction and kinetic energy). Two ap-
564 proaches are currently used to simulate tracks, each of them for different purpose.

565 The **Microscopic Simulation** uses the Garfield++ toolkit [1]. Within this
566 toolkit:

- 567 a) Magboltz, since it is mentioned later. Or maybe just class MediumMagboltz
568 with the collision rates?
- 569 b) the High Energy Electro-Dynamics (HEED) program [44] is used to simulate
570 the primary particle,
- 571 c) the class *AvalancheMicroscopic* to simulate the drift of secondary electrons
572 created by ionization in the gas.

573 This is the most precise and time-consuming simulation used; our current goal
574 is to be able to successfully reconstruct its results and determine our best-case
575 energy resolution.

576 The **Runge-Kutta Simulation** uses the 4th order Runge-Kutta numerical
577 integration ([add citation for Runge-Kutta](#)) to simulate the trajectory of the pri-
578 mary particle in the electromagnetic field inside the detector. It is relatively
579 fast since it does not simulate the secondary particles. It is used as part of our
580 reconstruction algorithm and for testing some parts of the reconstruction.

581 All of these simulations require the knowledge of the electromagnetic field
582 (both **E** and **B**) inside the detector. A uniform electric field of $400 \text{ V}\cdot\text{cm}^{-1}$ is
583 assumed. The magnetic field was simulated in Maxwell (see Section 1.4.3). [add
584 citation](#)

585 Single track in positive x direction or initial parameter randomization. Im-
586 portance of gas composition, used gas compositions.

587 2.1 Microscopic Simulation

588 The microscopic simulation, the most detailed simulation used in this work, is
589 performed using the Garfield++ toolkit [1].

590 The electron transport properties are simulated using the program Mag-
591 boltz ([add citation](#), [\(details?\)](#)). Two different gas mixtures were compared –
592 90:10 and 70:30 Ar:CO₂. The second mixture will be used in our detector ([this
593 was probably known a priori, but the first tests that I started with used 90/10,
594 so maybe just note that the results justify the fact so far](#)). The temperature is
595 set to 20 °C, the pressure is atmospheric.

596 The primary track is simulated using the program HEED, which is an imple-
597 mentation of the photo-absorption ionization model [44] ([see the reference, moved
598 it to the end of sentence](#)). This program provides the parameters of ionizing col-
599 lisions. HEED can also be used to simulate the transport of delta electrons; we
600 do not account for these in the current simulation ([but plan to include them in
601 the future – maybe mention only in the conclusion/future section](#)). The photons
602 created in the atomic relaxation cascade ([fluorescence reabsorption, related to
603 the spread of avalanches in GM det.?](#)) are also not simulated.

604 Finally, we use the microscopic tracking provided by the class *AvalancheMicroscopic*
 605 in Garfield++ to simulate the drift of the ionization electrons. Each
 606 electron is followed from collision to collision using the equation of motion and
 607 the collision rates calculated by Magboltz (how fast is this? maybe it slows down
 608 the simulation when spreading it across multiple jobs?).

609 Add more detailed and better description of HEED, and microscopic tracking
 610 (each their own subsection?). Could also mention Monte Carlo (requires gas file
 611 generation - Magboltz) and Runge-Kutta simulation implemented in Garfield,
 612 why we don't use them (another subsection? rename the section to Garfield++
 613 simulation and mention all relevant parts?).

614 2.1.1 First testing track

615 The first electron track simulated for testing purposes was chosen to have a special
 616 set of parameters:

- 617 • the starting point of the track is the origin of the coordinate system,
- 618 • the initial direction is along the positive x -axis,
- 619 • the momentum is 8 MeV/c (the kinetic energy is 7.505 MeV).

620 Such a track moves in the XZ plane in the toroidal magnetic field of the detector,
 621 because the particle's velocity vector is always perpendicular to the field. At first,
 622 we simulated such a track in 90:10 Ar:CO₂ gas mixture, later we added a simu-
 623 lation in 70:30 Ar:CO₂, which we plan to use in our detector. The comparison of
 624 both simulations is in Fig. 2.1. In the first tests, the initial energy of produced
 625 ionization was set to 0.1 eV instead of the value generated by HEED.

626 2.1.2 Grid-like testing sample

627 In order to test all steps of the reconstruction, a sample of tracks with a grid-like
 628 distribution of parameters was generated on MetaCentrum. Five sets of 9702
 629 tracks were generated with every combination of these parameters:

- 630 • electron and positron tracks,
- 631 • 11 different kinetic energies $E_{\text{kin}} \in [3, 13]$ MeV,
- 632 • 21 different azimuth angles $\varphi \in [-16.3^\circ, 16.3^\circ]$ and
- 633 • 21 different elevation angles $\theta \in [-17.1^\circ, 17.1^\circ]$.

634 A visualization of a set of e^+/e^- tracks with the same kinetic energy is shown in
 635 Fig. 2.2 (plotting actual HEED tracks using ROOT should be also possible (but
 636 hard to make look good?)). In the 70:30 Ar:CO₂ atmosphere, each track takes
 637 5-30 CPU hours to simulate. Every tenth point on the drift line was stored, the
 638 whole sample has 3.1 terabytes (or 1.4 gigabytes without drift lines).

639 2.2 Runge-Kutta Simulation

640 The Runge-Kutta simulation in this work uses the Runge-Kutta 4th order (RK4)
 641 method to numerically integrate the equation of motion of a relativistic charged
 642 particle in an electromagnetic field. Given a system of first order differential
 643 equations

$$\frac{dy}{dt} = f(t, y(t)) \quad (2.1)$$

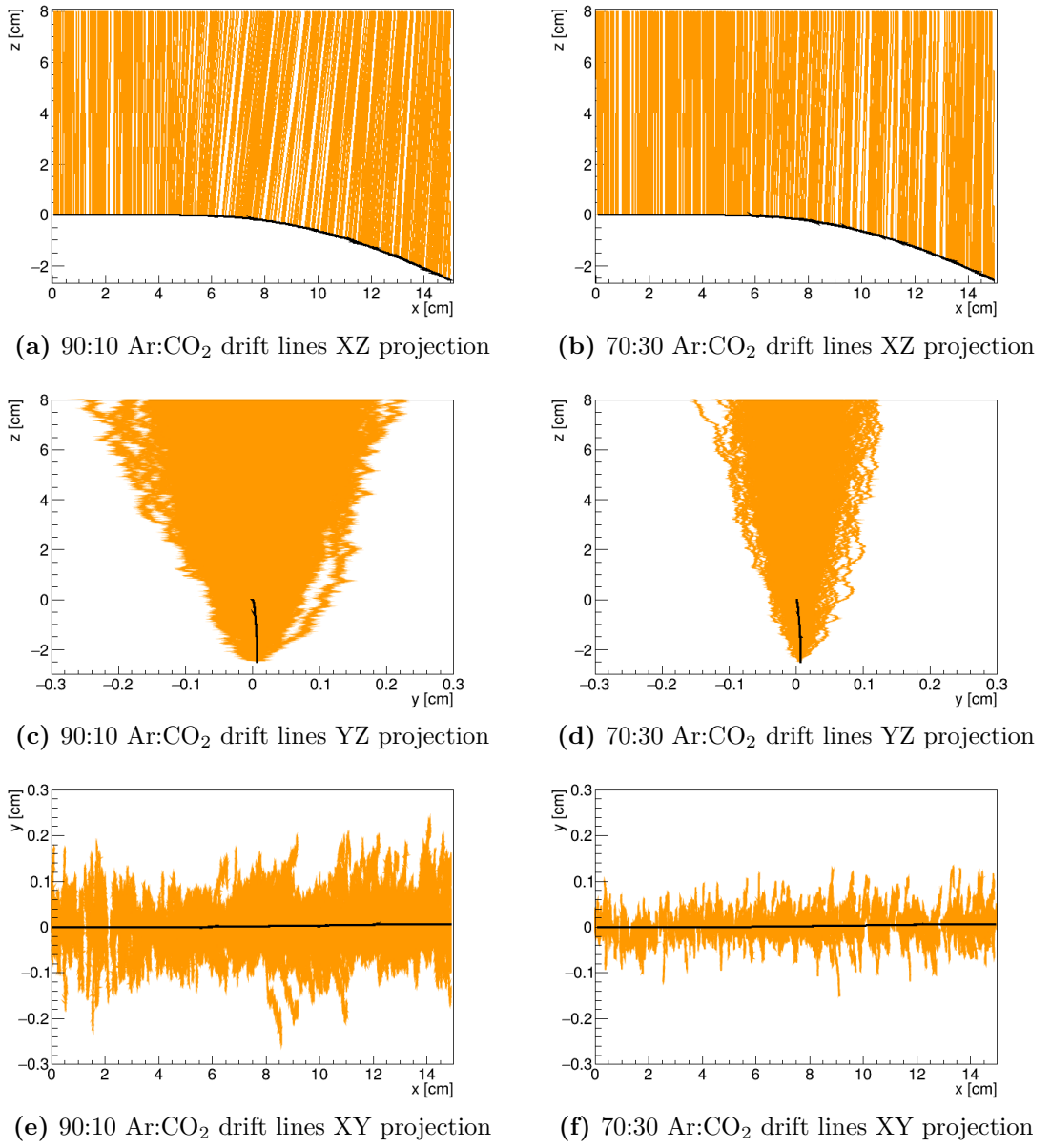


Figure 2.1: Comparison of drift lines for two different gas mixtures 90:10 and 70:30 Ar:CO₂. The electron track is marked in black, the drift lines of the ionization electrons are marked in orange. In this example, we assume a larger OFTPC volume with readout at $z = 8$ cm.

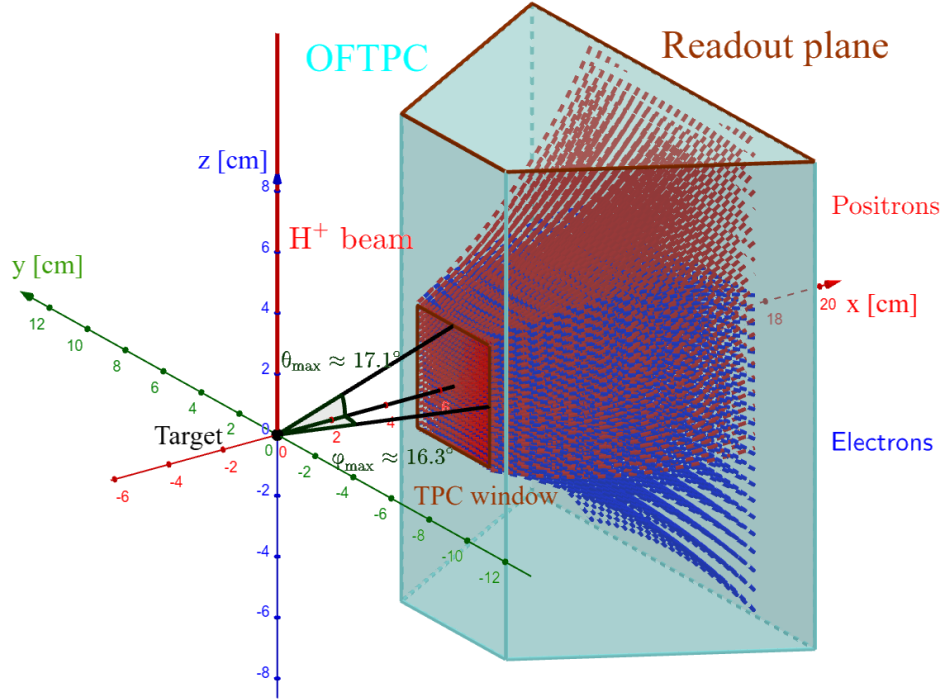


Figure 2.2: A visualization of a set of tracks from the grid-like testing sample with the same kinetic energy.

644 with an initial condition

$$\mathbf{y}(t_0) = \mathbf{y}_0, \quad (2.2)$$

645 we iteratively compute the estimate $\mathbf{y}_n = \mathbf{y}(t_n) = \mathbf{y}(t_0 + nh)$ as follows (citation?
646 common knowledge?):

$$\mathbf{k}_1 = \mathbf{f}(t_n, \mathbf{y}_n), \quad (2.3)$$

$$\mathbf{k}_2 = \mathbf{f}\left(t_n + \frac{h}{2}, \mathbf{y}_n + \frac{h\mathbf{k}_1}{2}\right), \quad (2.4)$$

$$\mathbf{k}_3 = \mathbf{f}\left(t_n + \frac{h}{2}, \mathbf{y}_n + \frac{h\mathbf{k}_2}{2}\right), \quad (2.5)$$

$$\mathbf{k}_4 = \mathbf{f}(t_n + h, \mathbf{y}_n + h\mathbf{k}_3), \quad (2.6)$$

647

$$\mathbf{y}_{n+1} = \mathbf{y}_n + \frac{1}{6}(\mathbf{k}_1 + 2\mathbf{k}_2 + 2\mathbf{k}_3 + \mathbf{k}_4). \quad (2.7)$$

648 Alternate forms (infinitely many) possible, accuracy vs computational cost. Runge-
649 Kutta-Fehlberg with adaptive step size also possible, can potentially save some
650 computation time especially in rapidly changing field (so maybe not in this case).

651 In our case, we want to integrate the equation of motion, given by the rela-
652 tivistic Lorentz force:

$$F_L^\mu = m \frac{du^\mu}{d\tau} = q F^{\mu\nu} u_\nu, \quad (2.8)$$

653 where the Einstein summation convention is used, m is the mass of the particle,
654 q is its charge, u^μ is its four-velocity, τ is the proper time (i.e., time in the particle's
655 frame of reference) and $F^{\mu\nu}$ is the electromagnetic tensor at given coordinates x^μ

656 (we consider it to be time-independent in our detector). Given the electric $\mathbf{E} =$
 657 $= (E_x, E_y, E_z)$ and the magnetic field $\mathbf{B} = (B_x, B_y, B_z)$ and using the metric
 658 signature $(+, -, -, -)$, the equation expands to

$$\frac{d}{d\tau} \begin{pmatrix} \gamma c \\ \gamma v_x \\ \gamma v_y \\ \gamma v_z \end{pmatrix} = \frac{q}{m} \begin{pmatrix} 0 & -\frac{E_x}{c} & -\frac{E_y}{c} & -\frac{E_z}{c} \\ \frac{E_x}{c} & 0 & -B_z & B_y \\ \frac{E_y}{c} & B_z & 0 & -B_x \\ \frac{E_z}{c} & -B_y & B_x & 0 \end{pmatrix} \begin{pmatrix} \gamma c \\ \gamma v_x \\ \gamma v_y \\ \gamma v_z \end{pmatrix}, \quad (2.9)$$

659 where c is the speed of light in vacuum, $\mathbf{v} = (v_x, v_y, v_z)$ is the particle's velocity
 660 and $\gamma = (1 - \frac{v^2}{c^2})^{-\frac{1}{2}}$ is the Lorentz factor. Together with the equation

$$\frac{d}{d\tau} \begin{pmatrix} ct \\ x \\ y \\ z \end{pmatrix} = \begin{pmatrix} \gamma c \\ \gamma v_x \\ \gamma v_y \\ \gamma v_z \end{pmatrix} = u^\mu, \quad (2.10)$$

661 we get a system of eight first order differential equations for x^μ and u^μ , which
 662 we can integrate using the Runge-Kutta method described above. As a result of
 663 this integration, we get the position $\mathbf{x}(\tau_n)$, the velocity $\mathbf{v}(\tau_n)$ and the detector
 664 time $t(\tau_n)$ for every proper time $\tau_n = n\tau_{\text{step}}$. Integrating using the proper time
 665 means that the step size in t gets larger by the gamma factor $\frac{dt}{d\tau} = \gamma$ (maybe
 666 change it and integrate the detector time or adjust the step size accordingly). The
 667 only difference is in the step size (because t gets also calculated as it is among the
 668 8 variables). **It might be even better to adjust the step size using approximate distance traveled.** As initial conditions, we use the origin of the track
 669 (x_0, y_0, z_0), the initial velocity direction vector $\mathbf{n} = (\cos \varphi \cos \theta, \sin \varphi \cos \theta, \sin \theta)$
 670 and the kinetic energy E_{kin} (initial parameters of the simulation (fit is in chapter 4)), we then compute γ and $\|\mathbf{v}\|$:

$$\gamma = 1 + \frac{E_{\text{kin}}}{E_0}, \quad (2.11)$$

$$\|\mathbf{v}\| = c\sqrt{1 - \gamma^{-2}}. \quad (2.12)$$

673 An example Runge-Kutta track is compared with the corresponding microscopic
 674 track in Fig. 2.3.

675 2.2.1 Testing sample

676 In order to test the simulation and reconstruction, a sample of 1 000 000 tracks
 677 with randomized parameters was generated:

- 678 • the Runge-Kutta step was set to 1.67 ps (coordinate time, each proper time
 679 step is adjusted by the gamma factor once at the beginning; for an 8 MeV
 680 track, $\tau_{\text{step}} = 0.1$ ps),
- 681 • the kinetic energy of the particle $E_{\text{kin}} = 3 - 13$ MeV,
- 682 • the starting point of the track is a random point in the OFTPC window,

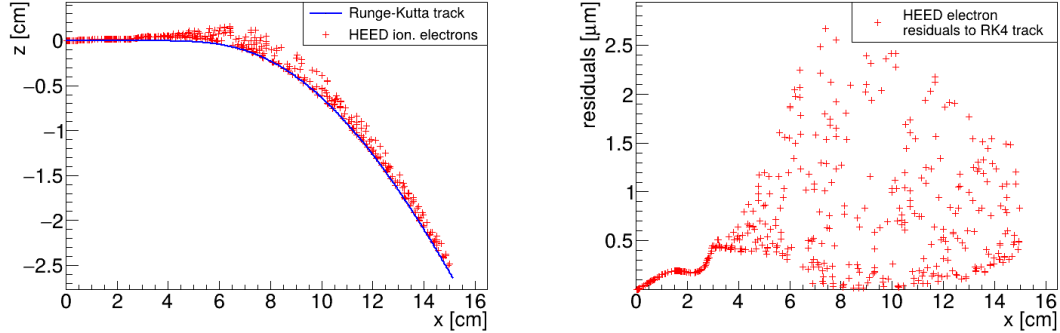


Figure 2.3: A comparison of the HEED track from the microscopic simulation in Section 2.1.1 with a Runge-Kutta track with the same initial parameters and $\tau_{\text{step}} = 0.1 \text{ ps}$ (reducing the step further doesn't make a visible difference). In the view of the tracks on the left, the distance of the HEED ionization electrons from the RK4 track is exaggerated $1000\times$. On the right, the dependence of the HEED electrons residuals (i.e., their shortest distance to the RK4 track) on their z -coordinate is shown. The images look the same even for $100,000\times$ smaller step, so the residuals are a result of something that HEED does (maybe a different interpolation technique for the magnetic field? the pattern looks similar for two different tracks so it can't be scattering).

When exaggerating, the HEED ionization electrons are moved away along the shortest line connecting them to the RK4 track. The computation of this distance is described in Section 4.3.

- 683 • the initial direction is given by the line connecting a random point on the
- 684 target¹ (a disc with 1 mm radius in the YZ plane).
- 685 Since the Runge-Kutta simulation is quite fast², it can be run locally on any
- 686 computer.

¹To generate a random point on the target, we generate a random angle α and a random square of the distance from origin r^2 to get a uniform distribution.

²One track with $t_{\text{step}} = 1.67 \text{ ps}$ takes less than one millisecond to simulate.

687 3. Track Reconstruction

688 As the first step of the reconstruction algorithm, we reconstruct the track of
689 a primary particle – either an electron or a positron. Then, using this information,
690 we determine the energy of the particle (Section 4).

691 The **Reconstruction Assuming Steady Drift (RASD)** uses the stan-
692 dard TPC approach. With parallel fields, the drift inside a uniform electric field
693 remains undistorted (as shown in Equation 1.1). Therefore, we only need to re-
694 construct the z -coordinate from the drift time using the known drift velocity. We
695 also assume that the readout coordinates (x', y', t) are known exactly, neglecting
696 the pads and time binning.

697 Reconstruction using an **Ionization Electron Map** (from now on referred
698 to as *the map*) uses a simulation of the drift of secondary (ionization) electrons
699 within the detector volume. This simulation can then be used to interpolate the
700 initial position of the secondary electrons. In the first iteration of this method
701 the readout is assumed to be continuous.

702 We present two algorithms using the map for reconstruction. The first one uses
703 a gradient descent algorithm along with trilinear interpolation (see Section 1.4.3)
704 of the map. The second method uses interpolation on the irregular inverse grid
705 with a polynomial.

706 The **Discrete Reconstruction** uses the map; instead of reconstructing the
707 exact position of each electron, we reconstruct the center of each hit pad together
708 with the time corresponding to the midpoint of the time bin. The electron count
709 in each TPC bin (consisting of the pad and the time bin) serves as an idealized
710 collected charge, which is then used as a weight in the energy reconstruction fit.

711 3.1 Reconstruction Assuming Steady Drift

712 As the first step, we tried to reconstruct a simulated electron track with a special
713 set of initial parameters, described in detail in Section 2.1.1. The starting point
714 is given by the origin of our coordinate system and its initial direction is given by
715 the positive x -axis. This means the magnetic field of our detector is perpendicular
716 to the momentum of the particle at all times, and we can reduce the problem to
717 two-dimensional space.

718 For the reconstruction, we decided to use the common method used in a stan-
719 dard TPC (*similar to?, cite some source(s)!*). We call this method *Reconstruction*
720 *Assuming Steady Drift (RASD)*. This will allow us to explore the significance of
721 the atypical behavior in our OFTPC. Additionally, we assume the readout is con-
722 tinuous to further simplify the problem. In this approximation, we reconstruct
723 the initial position of each ionization electron.

724 The reconstruction is then defined by the following relations between the
725 coordinates of the detector space and the readout space (see Section 1.4.2):

$$x = x', \tag{3.1}$$

$$y = y', \tag{3.2}$$

$$z = 8 \text{ cm} - d_r = 8 \text{ cm} - v_d t, \tag{3.3}$$

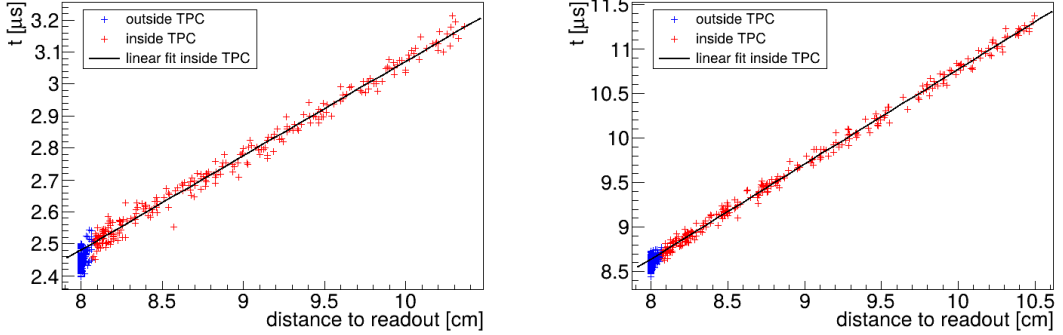


Figure 3.1: Linear fit of the drift time t dependence on the distance to the readout $d_r = 8 \text{ cm} - z$ for the ionization electrons in 90:10 (left) and 70:30 (right) Ar:CO₂ gas composition. Only electrons inside the TPC (red) are fitted. The parameters are $v_d = 3.39 \text{ cm}/\mu\text{s}$, $d_0 = -0.41 \text{ cm}$ for 90:10, and $v_d = 0.939 \text{ cm}/\mu\text{s}$, $d_0 = -0.11 \text{ cm}$ for 70:30 Ar:CO₂.

where d_r is the distance to the readout, and v_d is the drift velocity of electrons in the given gas mixture. At a phenomenological level, this velocity can be considered as a function of the electric field \mathbf{E} and the magnetic field \mathbf{B} as shown in Equation 1.1. The Garfield++ toolkit uses this fact to accelerate their drift simulation with non-microscopic approaches (could mention in the simulation chapter). Since we assume a uniform electric field in the detector and in this approximation we want to neglect the effect of our unusual magnetic field, we consider the drift velocity constant. We can estimate the drift velocity by fitting the dependence $d_r(t)$ of ionization electrons from a simulated track with a linear function:

$$d_r(t) = v_d t + d_0. \quad (3.4)$$

The fit was applied on two tracks with different gas composition, the result is in Fig. 3.1. Compare with real drift velocities – a good indication of the tilt of drift lines. The obtained parameters are then used for the reconstruction shown in Fig. 3.2. From the residuals shown in Fig. 3.3, we can see that this reconstruction algorithm leads to significant deviations from the simulated track (up to 1.1 cm for 90:10, and up to 0.3 cm for 70:30 Ar:CO₂), especially in the faster gas mixture 90:10 (as expected – for a higher mean time between collisions in Equation 1.1, the effect of the magnetic field is bigger). These deviations are mainly caused by the shift in the x -coordinate due to the tilt of the drift lines in magnetic field. In order to account for this, we need to develop a better algorithm. There is also a small irregularity in the z -coordinate but it is comparable with the diffusion. We can/will also later show that this has a significant effect on the reconstructed energy.

3.2 Ionization Electron Map

Inside an OFTPC (\exists more than one, also considering it a general concept rather than the specific OFTPC used at this experiment), the drift of the ionization electrons is significantly affected by its magnetic field as shown in Equation 1.1, see also Fig. 2.1. We need to take this into account for accurate reconstruction (should be easy to run the reconstruction without the map and show how

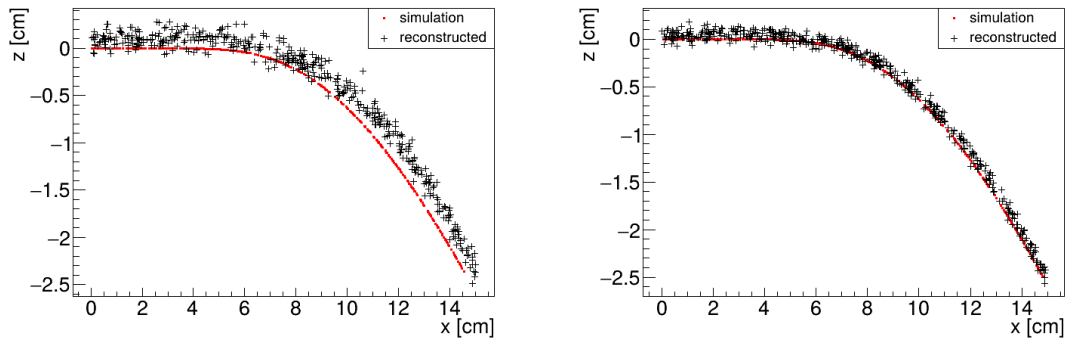


Figure 3.2: Reconstruction (black) of the starting position of ionization electrons (red) using parameters obtained from the fit (Fig. 3.1). Two gas compositions 90:10 (left) and 70:30 Ar:CO₂ (right) are compared.

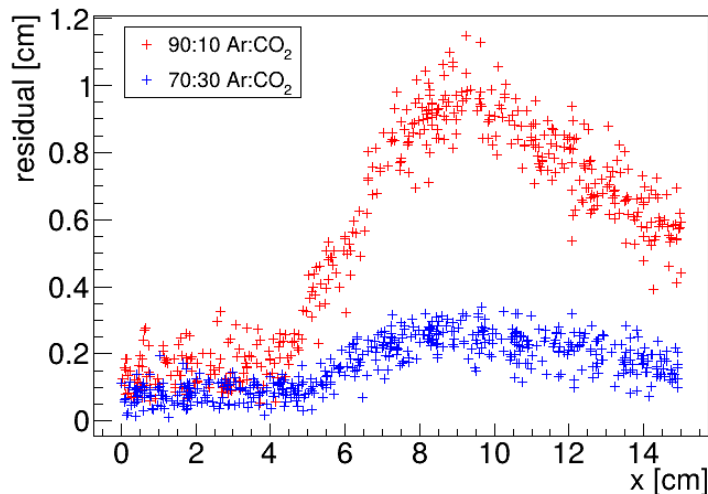


Figure 3.3: Comparison of residuals (i.e., the distance from the reconstructed point to the simulated ionization electron starting point) dependence on x for two gas mixtures 90:10 (red) and 70:30 Ar:CO₂ (blue).

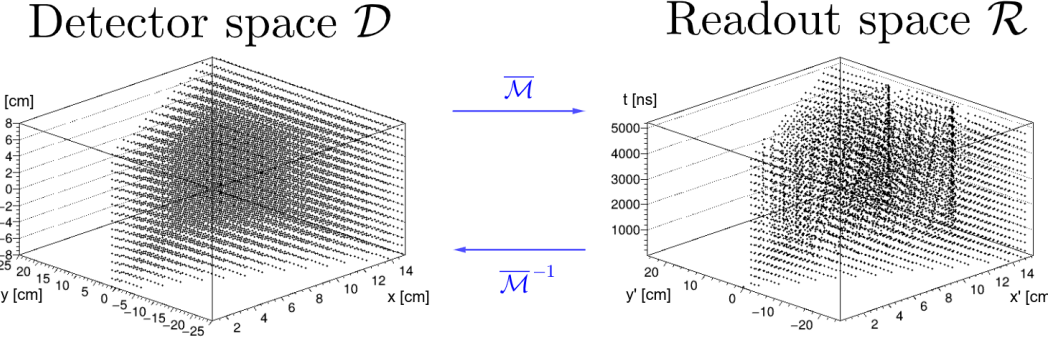


Figure 3.4: A 3D visualization of the mapping of means $\bar{\mathcal{M}}$ for the 90:10 Ar:CO₂ gas. A regular grid \mathbb{G} with $l = 1$ cm in the detector space is mapped to an irregular grid $\mathbb{G}^{-1} \equiv \bar{\mathcal{M}}(\mathbb{G})$ in the readout space.

754 much it improves the results). In the first approximation, we assume a contin-
 755 uous readout (i.e., we neglect the anode segmentation into pads). We can then
 756 reconstruct the original position of each ionization electron using its readout co-
 757 ordinates. For this purpose, we use the ionization electron map.

758 The ionization electron map represents a mapping from the detector space
 759 to the readout space (see Section 1.4.2). It tells us what readout coordinates
 760 (x', y', t) we can expect on average for an ionization electron created at the detec-
 761 tor coordinates (x, y, z). More precisely, it is a mapping to the distributions on
 762 the readout space; we can simplify this as only the means $\bar{\mathcal{M}}$ and the covariance
 763 matrices \mathcal{M}_Σ , assuming Gaussian distribution¹:

$$\bar{\mathcal{M}}: \mathcal{D} \longrightarrow \mathcal{R}, \quad (x, y, z) \longmapsto \bar{\mathbf{X}}^T \equiv (\bar{x}', \bar{y}', \bar{t}), \quad (3.5)$$

$$\mathcal{M}_\Sigma: \mathcal{D} \longrightarrow \mathbb{R}^{3 \times 3}, \quad (x, y, z) \longmapsto \Sigma \equiv \begin{pmatrix} \sigma_{x'}^2 & \text{cov}(x', y') & \text{cov}(x', t) \\ \text{cov}(y', x') & \sigma_{y'}^2 & \text{cov}(y', t) \\ \text{cov}(t, x') & \text{cov}(t, y') & \sigma_t^2 \end{pmatrix}, \quad (3.6)$$

$$\mathcal{M}: \mathcal{D} \longrightarrow D(\mathcal{R}), \quad (x, y, z) \longmapsto N(\mathbf{X}) \equiv \frac{\exp\left(-\frac{1}{2}(\mathbf{X} - \bar{\mathbf{X}})^T \Sigma (\mathbf{X} - \bar{\mathbf{X}})\right)}{\sqrt{(2\pi)^3 |\Sigma|}}. \quad (3.7)$$

764 To get an approximation of this mapping, we simulate the drift of ionization
 765 electrons generated on a regular Cartesian grid $\mathbb{G} \subset \mathcal{D}$ with spacing l inside the
 766 volume of our OFTPC² (see the visualization in Fig. 3.4). In Fig. 3.5, you can
 767 see an example of drift lines from a test of the simulation. After testing runs, two
 768 map simulations were made with different gas composition, their parameters are
 769 shown in Table 3.1.

770 In order to get accurate results, we use the microscopic simulation of these
 771 electrons described in Section 2.1 (Monte Carlo from *AvalancheMC* was also con-
 772 sidered but it doesn't (didn't? CERES used it from MAGBOLTZ???) include
 773 magnetic field, we can probably improve this anyway using the fast track sim-
 774 ulation with map proposed in the future section). It is also useful to simulate
 775 multiple (N) electrons originating from the same position so that we can account

¹The applicability of Gaussian distribution was tested on simulated points of the map using the Mardia's test.

²The detector walls are not considered and we simulate the drift even outside of the OFTPC which allows us to interpolate even close to the walls.

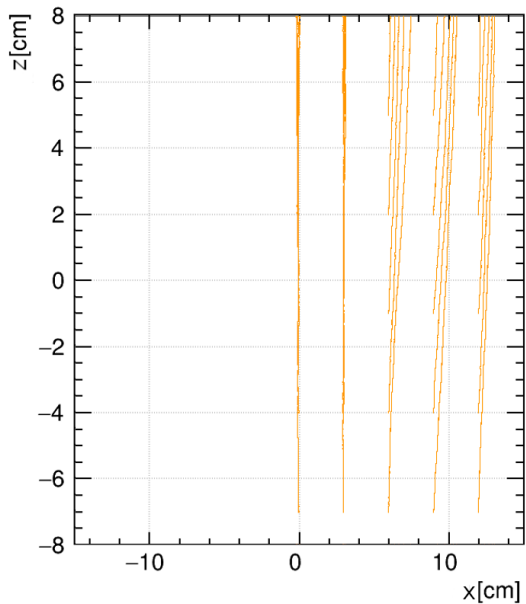


Figure 3.5: A test of the 90:10 Ar:CO₂ map simulation with spacing $l = 1.5$ cm. The resulting drift lines of evenly spaced electrons are displayed in orange.

Table 3.1: Comparison of parameters of two map simulations.

Parameter	90:10 Ar:CO ₂ map	70:30 Ar:CO ₂ map
N	100	100
l	1.0 cm	0.5 cm
z bounds	$[-8, 8]$ cm	$[-8, 8]$ cm
x bounds	$[0, 15]$ cm	$[-1.5, 15.0]$ cm
y bounds	$ y \leq x \cdot \tan \frac{\pi}{3}$	$ y \leq (x + 1.5 \text{ cm}) \cdot \tan \frac{\pi}{6}$
initial energy	0.1 eV	0.1 eV
init. direction	randomized	randomized

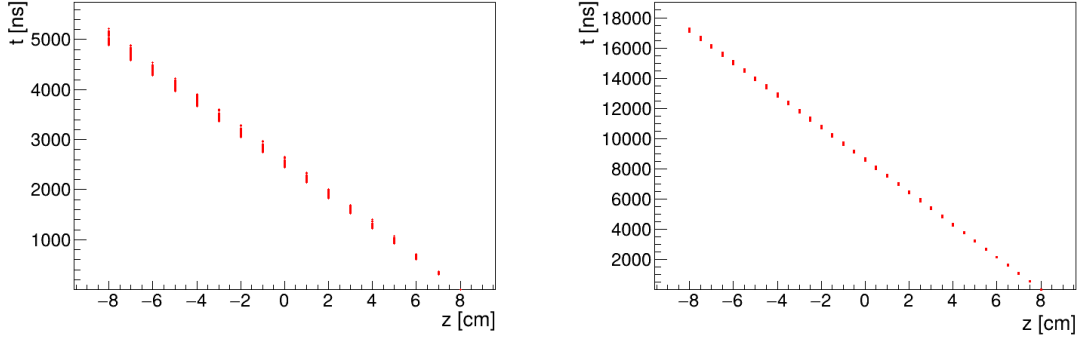


Figure 3.6: Dependence of the drift times of the simulated map $\bar{\mathcal{M}}$ on the z -coordinate. Two gas mixtures 90:10 (left) and 70:30 Ar:CO₂ (right) are compared. The spread is caused by varying Lorentz angles.

for the random fluctuations due to collisions. Using the readout coordinates of the electrons, we then estimate the means and the covariance matrix:

$$\bar{\mathbf{X}} = \frac{1}{N} \sum_{i=1}^N \mathbf{X}_i, \quad \Sigma = \frac{1}{N-1} \sum_{i=1}^N (\mathbf{X}_i - \bar{\mathbf{X}})(\mathbf{X}_i - \bar{\mathbf{X}})^T, \quad (3.8)$$

where \mathbf{X}_i represents the readout coordinates $(x'_i, y'_i, t_i)^T$ of the i -th electron. The matrix (resp. its submatrix) can then be used to plot error ellipsoid (resp. ellipse). The axes correspond to the eigenvectors, errors along these axes for a given confidence level p can be computed using the chi-squared distribution

$$\sigma_i = \sqrt{\lambda_i \chi_k^2(p)}, \quad (3.9)$$

where λ_i is the corresponding eigenvalue and k is the number of degrees of freedom.

As shown in Figs. 3.6 and 3.7, the drift times in the map are no longer proportional to the z -coordinate due to the varying Lorentz angles in the inhomogeneous magnetic field (see Equation 1.2). As expected, the effect is considerably larger in gases with higher drift velocities. Similarly, the drift distortion (i.e., its deviation from the vertical lines) is huge for the "faster" gas, but still significant for the "slower" one, as demonstrated in Figs. 3.8 to 3.10.

When evaluating the map inside the grid, we use trilinear interpolation (see Section 1.4.3). From now on, we will use the same symbol \mathcal{M} for this interpolated simulation.

Finally, we need to invert the map to get the original detector coordinates (x, y, z) from the given readout coordinates (x', y', t) . In our case, it is reasonable to assume that the mapping $\bar{\mathcal{M}}$ (we lose the information about the distribution (a wild idea how to recover this is in the Future section but it will only make sense if the GEM is already accounted for and is very preliminary as there are many factors to consider)) is one-to-one (as seen in the simulations). We implemented two methods for this purpose: the gradient descent search (Section 3.2.2) and interpolation on the inverse grid (Section 3.2.3).

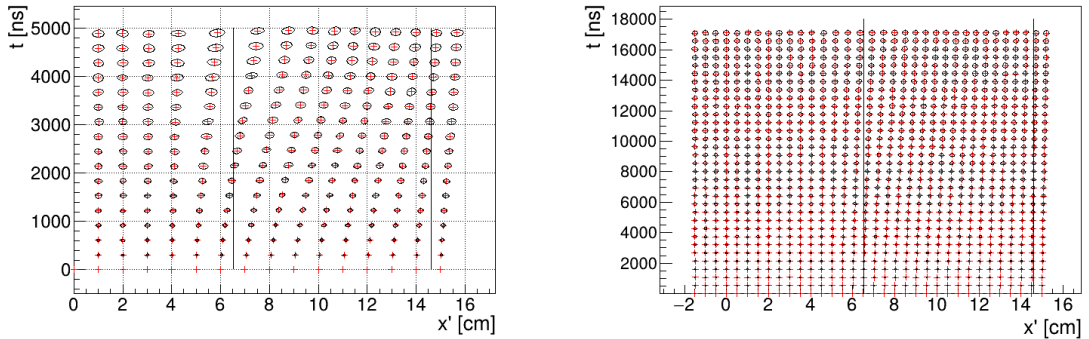


Figure 3.7: The $x't$ projection of the $\mathcal{M}(\mathbb{G}_{y=0})$ mapping of a part of the regular grid \mathbb{G} . The means $\overline{\mathcal{M}}(\mathbb{G}_{y=0})$ are marked with red crosses, and the diffusion error is denoted by black 95% confidence error ellipses computed from the diagonalized covariance matrices $\mathcal{M}_\Sigma(\mathbb{G}_{y=0})$. Two gas mixtures 90:10 (left) and 70:30 Ar:CO₂ (right) are compared. The first mixture shows differences of t for electrons with same initial z but different initial x . For the second mixture, these differences are negligible in comparison with the diffusion.

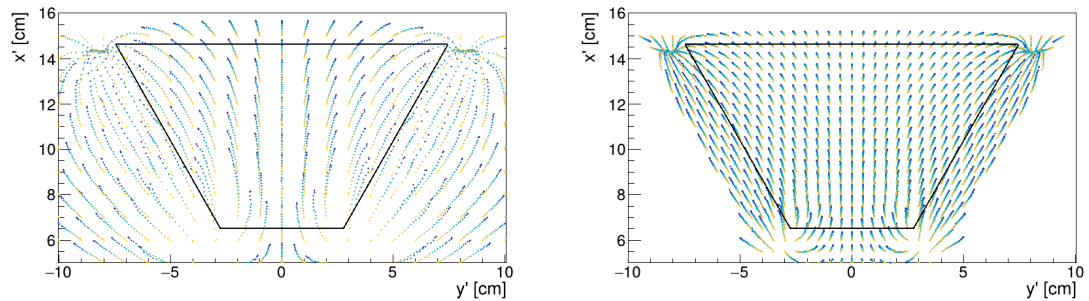
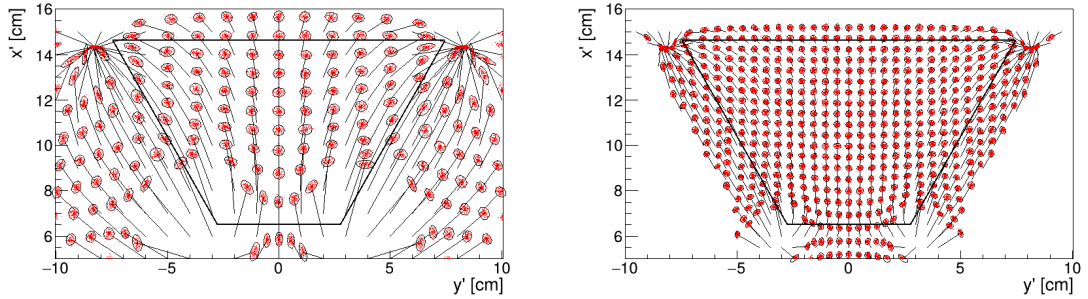
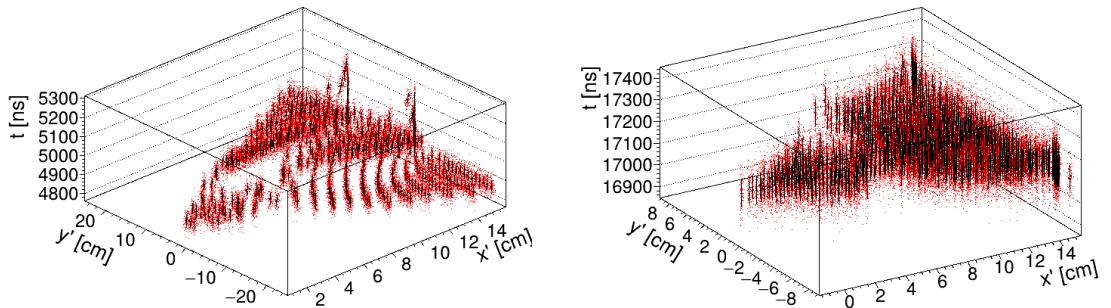


Figure 3.8: The regular grid \mathbb{G} projected by the mapping $\overline{\mathcal{M}}$ from the detector space onto the $x'y'$ plane (t is not plotted). Layers with lower z -coordinate (i.e., further away from the readout) are displayed with darker colors. The OFTPC volume is marked with black lines. Two gas mixtures 90:10 (left) and 70:30 Ar:CO₂ (right) are compared.



(a) The $x'y'$ projection of $\mathcal{M}(\mathbb{G}_{-8})$ (similar as in Fig. 3.8), the diffusion is denoted with the 95% error ellipses from the diagonalized sample covariance matrices $\mathcal{M}_\Sigma(\mathbb{G}_{-8}) \leftrightarrow$ Equation 3.8, and computed using Equation 3.9. The mean values $\bar{\mathcal{M}}(\mathbb{G}_{-8})$ are connected by black arrows with the corresponding starting position (x, y) of the simulated electrons. The OFTPC volume is marked with black lines.



(b) The full mapping $\mathcal{M}(\mathbb{G}_{-8})$, the diffusion is marked using standard error bars (black) from the diagonalized sample covariance matrices (Equations 3.8 and 3.9).

Figure 3.9: The $\mathcal{M}(\mathbb{G}_{-8})$ mapping of the bottom ($z = -8$ cm) layer \mathbb{G}_{-8} of the regular grid $\mathbb{G} \subset \mathcal{D}$. It includes both the mapping of means $\bar{\mathcal{M}}$ and of covariances \mathcal{M}_Σ . Individual electrons from the map simulation are marked with red dots. Two gas mixtures 90:10 (left) and 70:30 Ar:CO₂ (right) are compared.

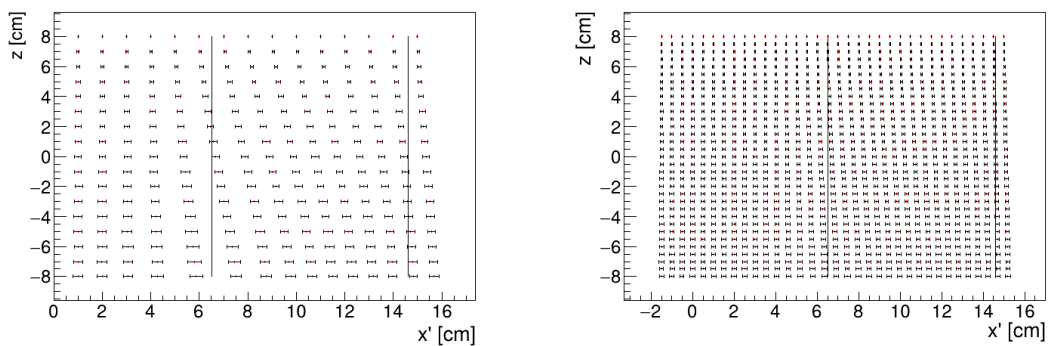


Figure 3.10: The readout coordinate x' for points on the grid $\mathbb{G}_{y=0}$ plotted against their initial coordinate z . The means are marked with red crosses, the diffusion in x' is denoted by standard error bars. Two gas mixtures 90:10 (left) and 70:30 Ar:CO₂ (right) are compared.

801 3.2.1 Map Simulation

802 Simulation of the map is a computationally heavy task. For this reason, we use
 803 the MetaCentrum grid [3] to parallelize needed calculations. At first, this was
 804 done by evenly distributing the simulated electrons across the individual jobs
 805 in a simulation with only one electron per vertex in the regular grid \mathbb{G} with
 806 a spacing of one centimeter. Later, a more efficient approach was implemented,
 807 accounting for the varying lengths of the drift of individual electrons. If we index
 808 the vertices of \mathbb{G} in the order of increasing coordinates y, x, z (picture will make
 809 things clearer), we can express the number n_l of full XY layers (i.e., electrons
 810 with the same z coordinate, the mapping of one such layer is shown in Fig. 3.9b)
 811 with index less than or equal to i

$$n_l(i) = \left\lfloor \frac{i}{n_{xy}} \right\rfloor, \quad (3.10)$$

812 where n_{xy} is the number of electrons in each XY layer calculated simply by count-
 813 ing the electrons that satisfy boundary conditions for x and y . These conditions
 814 should be mentioned above; sector condition + maximal x value. The number of
 815 electrons remaining in the top layer is then

$$n_r(i) = i \bmod n_{xy}. \quad (3.11)$$

816 Finally, we can calculate the sum of the drift gaps of electrons up to index i

$$d_{\text{sum}} = (z_{\max} - z_{\min})n_{xy}n_l - \frac{n_l(n_l - 1)}{2}n_{xy}l + n_r(z_{\max} - z_{\min} - n_ll). \quad (3.12)$$

817 We then use a binary search algorithm to find the maximum index i such that
 818 the value of this sum is less than the fraction $\frac{\text{job id}}{\max \text{ job id}}$ of the total sum. This way
 819 we obtain the minimal and the maximal index of electrons simulated in the given
 820 job.

821 The obtained map is then stored in a custom class template *Field*, could
 822 expand on that. Maybe earlier, since the same template is used for the magnetic
 823 field.

824 Extra space on the sensor. Using qsub (not sure if important).

825

826 3.2.2 Gradient Descent Algorithm

827 The first implemented method of reconstruction uses a gradient descent algorithm
 828 to calculate an inversion of the map $\bar{\mathcal{M}}$ in a given point. Gradient descent is an
 829 iterative minimization algorithm for multivariate functions. Let $R \in \mathcal{R}$ be a point
 830 in the readout space; we want to find a point $D = (x, y, z) \in \mathcal{D}$ in the detector
 831 space such that

$$\bar{\mathcal{M}}(D) = R = (x'_R, y'_R, t_R). \quad (3.13)$$

832 We define a function f_R in the readout space as a distance in this space:

$$f_R(x', y', t) = \sqrt{(x' - x'_R)^2 + (y' - y'_R)^2 + v_d^2(t - t_R)^2}, \quad (3.14)$$

833 where v_d is an approximation of the drift velocity in the TPC, obtained from the
 834 reconstruction in Section 3.1 (there will be an image with the linear fit here). We
 835 make an initial guess (actually in the original code we just take $z = 0$):

$$D_0 = (x'_R, y'_R, v_d t). \quad (3.15)$$

836 Assuming we have the n -th estimate D_n , we calculate the i -th component of the
 837 gradient of $f_R \circ \bar{\mathcal{M}}$ numerically using central differences: (signs look correct)

$$[\nabla(f_R \circ \bar{\mathcal{M}})]^i(D_n) \approx \frac{f_R(\bar{\mathcal{M}}(D_n + s \cdot e^i)) - f_R(\bar{\mathcal{M}}(D_n - s \cdot e^i))}{2s}, \quad (3.16)$$

838 where $e^i \in \mathcal{D}$ is the i -th coordinate vector and s is the step size. The step size
 839 should be sufficiently small; initially, we set it as a fraction $s = \frac{l}{10}$ of the map's
 840 grid spacing l . During the minimization, we check that $f_R(\bar{\mathcal{M}}(D_n)) < 10s$ at all
 841 times and decrease the step if needed. The next iteration can be calculated as
 842 follows:

$$D_{n+1} = D_n - \gamma \nabla(f_R \circ \bar{\mathcal{M}})(D_n), \quad (3.17)$$

843 where $\gamma \in \mathbb{R}^+$ is the damping coefficient. It should be set to a small enough
 844 value to ensure convergence, but large enough for sufficient converging speed. In
 845 order to avoid oscillation around the minimum, we also check that the size of the
 846 damped gradient does not exceed (or get too close to) the current value of the
 847 non-negative function:

$$10 \|\gamma \nabla(f_R \circ \bar{\mathcal{M}})(D_n)\| < f_R(D_n), \quad (3.18)$$

848 and lower γ otherwise. The minimization stops either when the error $f_R(\bar{\mathcal{M}}(D_n))$
 849 drops below a specified value or when the number of iterations exceeds a certain
 850 limit (in this case, a message is printed into the console).

851 The parameters of this method can be further optimized (e.g., a better choice
 852 of γ and s , analytical computation of the gradient³); instead, we later decided to
 853 use the interpolation on the inverse grid described in the next section.

854 Typical evolution of D_n during search? Not sure if this has to be cited.

855 3.2.3 Interpolation on the Inverse Grid

856 The best current algorithm uses the interpolation on the inverse grid. Rather
 857 than inverting the trilinearly interpolated map using a numerical minimization
 858 method as in the previous section, we take advantage of the fact that the map
 859 $\bar{\mathcal{M}}$ is one-to-one (isomorphism is supposed to preserve structure, not sure how
 860 to interpret that here, not the best description, we already (kind of) assume it
 861 is a bijection by saying we will invert it). Since we have simulated values of this
 862 map on a regular grid in the detector space \mathcal{D} , we also know the inverse map $\bar{\mathcal{M}}^{-1}$
 863 on the irregular inverse grid in the readout space \mathcal{R} . To get an approximation
 864 of the inverse map in the entire readout space, we can use interpolation (general
 865 concept, the specific choice is described below).

³The gradient can be computed analytically when using the trilinear interpolation, see Eq. 1.21.

866 Since the inverse grid is irregular, trilinear interpolation cannot be applied.
 867 Given that the simulated map is dense enough to provide a good approximation
 868 considering the size of our pads, we can adopt a similar approach.⁴ As shown in
 869 Equation 1.21 in Section 1.4.3, trilinear interpolation (shouldn't need an article
 870 when talking about a general concept) can be expressed as a polynomial:

$$\hat{f}(x, y, z) = axyz + bxy + cxz + dyz + ex + fy + gz + h, \quad (3.19)$$

871 where a, b, c, d, e, f, g, h are coefficients uniquely determined by the values of the
 872 function at the vertices of the interpolation cell (can be calculated in the way
 873 shown in the mentioned equation, not sure what more to add). We can generalize
 874 this for a function defined on an irregular grid. Given the function values at any
 875 eight points, we can write a system of eight linear equations

$$\begin{pmatrix} x_1y_1z_1 & x_1y_1 & x_1z_1 & y_1z_1 & x_1 & y_1 & z_1 & 1 \\ \vdots & \vdots \\ x_8y_8z_8 & x_8y_8 & x_8z_8 & y_8z_8 & x_8 & y_8 & z_8 & 1 \end{pmatrix} \begin{pmatrix} a \\ b \\ c \\ d \\ e \\ f \\ g \\ h \end{pmatrix} = \begin{pmatrix} f(x_1, y_1, z_1) \\ \vdots \\ f(x_8, y_8, z_8) \end{pmatrix}, \quad (3.20)$$

876 which has a unique solution for the coefficients for most values of (x_n, y_n, z_n) and
 877 $f(x_n, y_n, z_n)$, where $n \in \{1, \dots, 8\}$.

878 This approach introduces a small complication: finding the correct pseudocell
 879 (i.e., the image of eight vertices forming a cubic cell in the regular grid) in
 880 the inverse grid. The eight irregularly spaced vertices of this pseudocell do not
 881 define a unique volume, so there are multiple possible ways to partition \mathcal{R} into
 882 pseudocells, with no obvious choice among them. This problem could be solved
 883 by determining the exact volume boundary using the gradient descent search
 884 described above. However, since the difference between the interpolation poly-
 885 nomials is small near the boundary of the pseudocell, we choose one of them
 886 arbitrarily.

887 In the code, the map is stored in an array, and its individual points can be
 888 accessed using three indexes corresponding to the x , y , and z coordinates. Points
 889 outside of the area of the simulation are initialized with zeros. The search for
 890 the pseudocell finds the indices corresponding to the eight vertices. It starts by
 891 performing a binary search along the x -coordinate (comparing the x' -coordinate
 892 of the map vertices with that of the point, whose preimage we want to find) with
 893 indices corresponding to y and z fixed to half of their maximal value. After that,
 894 we fix the x and z indices and perform a binary search along y (making sure to
 895 exclude the zeros from initialization outside the simulation range beforehand),
 896 and finally, we fix the x and y indices and perform a search along z (inverted,
 897 since higher z corresponds to lower t). This procedure is then repeated until
 898 the pseudocell "contains" the preimage of the given point (meaning that for all
 899 readout coordinates x', y', t , there is a vertex of the pseudocell with a higher and
 900 a vertex with a lower value of that coordinate). Or until 3 iterations are exceeded,
 901 then we print an error message. We also attempt to fix the error by choosing a
 902 neighboring cell.

903 This approach should generally be faster than the gradient descent method,
 904 since we do not need to iterate. Currently, we are calculating the coefficients of

⁴A more complicated and computationally heavy alternative would be natural neighbor interpolation or Kriging.

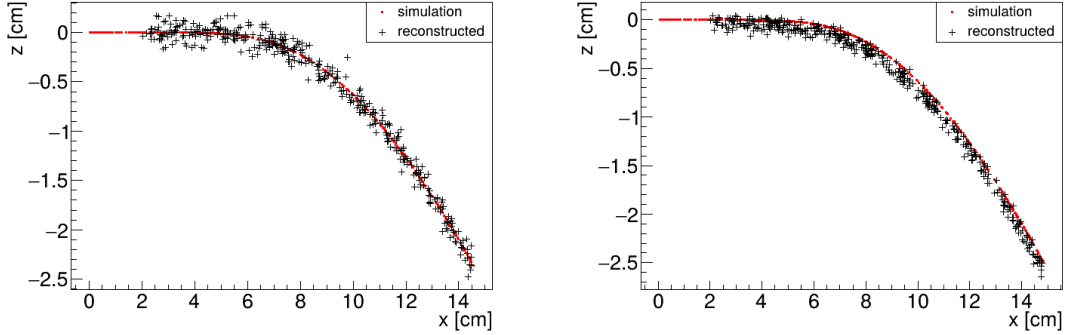


Figure 3.11: Reconstruction (black) of the starting position of ionization electrons (red) using the inversion of the ionization electron map. Two gas compositions 90:10 (left) and 70:30 Ar:CO₂ (right) are compared.

905 the interpolation polynomial during the reconstruction of every point. If further
 906 optimization is needed in the future, we can precalculate them for the whole map.

907 3.3 Reconstruction testing

908 The continuous reconstruction using the map was tested on microscopic tracks
 909 with parameters described in Sec. 2.1.1. The difference between the reconstructed
 910 positions obtained using the two map inversion algorithms was found to be smaller
 911 than the uncertainty from diffusion by several orders of magnitude. In its unop-
 912 timized state, the gradient descent search was significantly slower (at least ten
 913 times) than the interpolation on the inverse grid.

914 An example of reconstruction of tracks in 90:10 and 70:30 Ar:CO₂ gas mixture
 915 is shown in Fig. 3.11. We can clearly see that the results have improved com-
 916 pare to the Reconstruction Assuming Steady Drift (RASD) (shown in Fig. 3.2).
 917 A comparison of the residuals of reconstructed positions (i.e., their distances to
 918 the real starting positions) is shown in Fig. 3.12. The histograms of residuals, as
 919 well as residuals of individual coordinates, are shown in Figs. 3.13 and 3.14. The
 920 bin width for the histograms was chosen using the Scott's rule⁵. As expected,
 921 the mean values of the coordinate residuals is zero. The only exception is the
 922 z -coordinate in the 70:30 Ar:CO₂ track, where the mean is -0.064 cm (further
 923 than one standard deviation 0.051 cm from zero). This is caused by the non-zero
 924 initial energy of the ionization electrons (neglected in the other track) which is
 925 unaccounted for in the map simulation. Since the primary electron bends towards
 926 negative z , the ionization electrons are more likely to be released in this direction
 927 (and also bend in the magnetic field towards this direction).

928 3.4 Discrete Reconstruction

929 In order to get a more realistic representation of a track measured in the OFTPC,
 930 we need to take the discretization of the position and time data into account. The

⁵The optimal bin width for normally distributed data of size N with sample standard deviation $\hat{\sigma}$ is $\hat{\sigma} \sqrt[3]{\frac{24\sqrt{\pi}}{N}}$ [45].

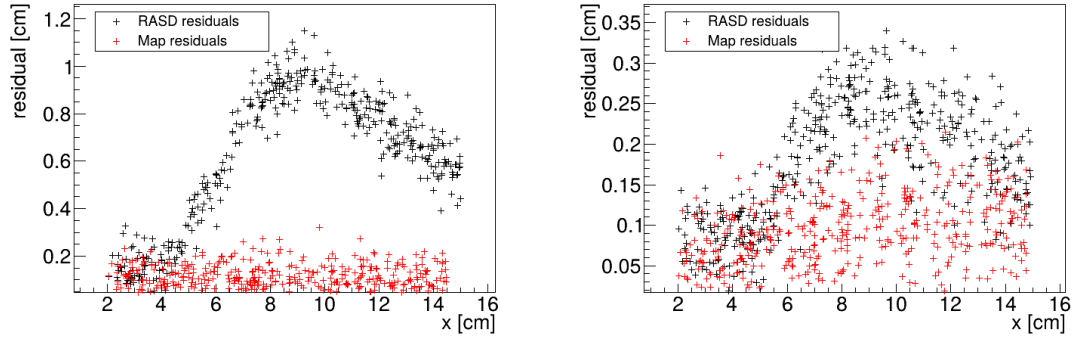


Figure 3.12: Comparison of residuals from the RASD (black) and map inversion (red) reconstruction methods. Tracks in two different gas compositions 90:10 (left) and 70:30 Ar:CO₂ (right) are compared.

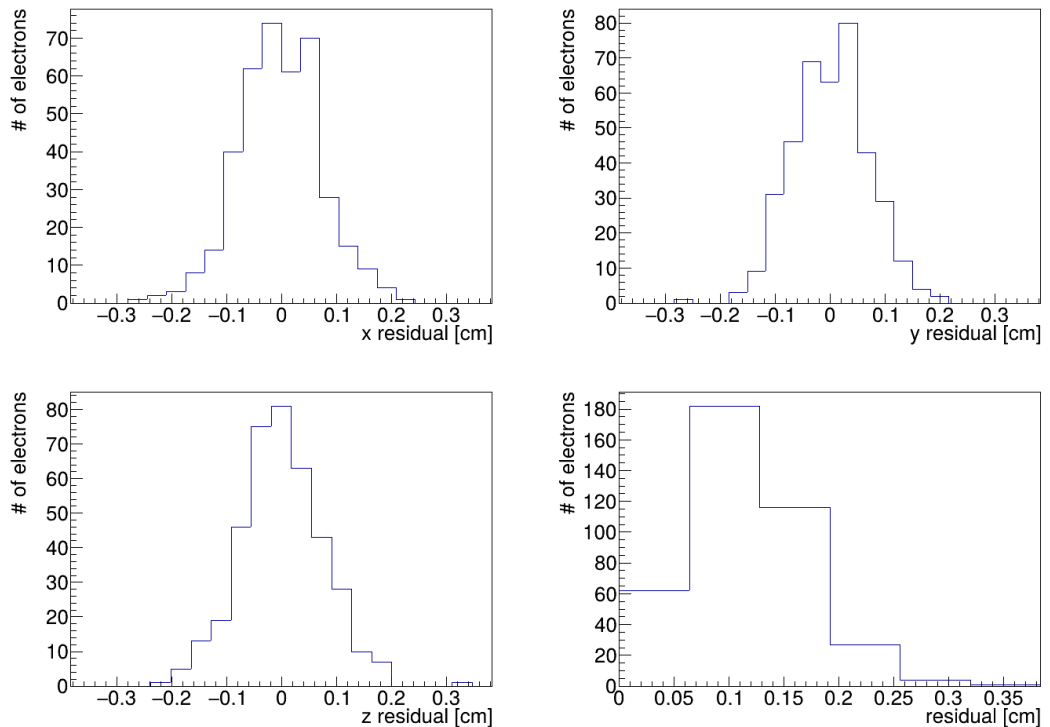


Figure 3.13: Map inversion reconstruction residuals (for the individual coordinates and total) of the testing track in 90:10 Ar:CO₂ gas mixture.

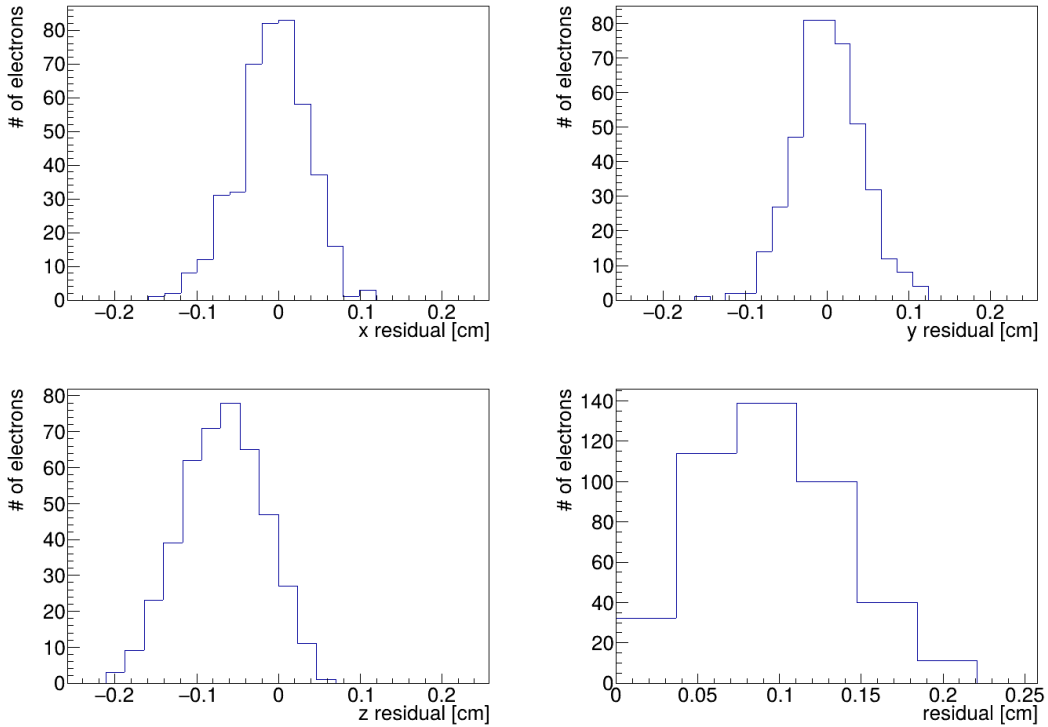


Figure 3.14: Map inversion reconstruction residuals (for the individual coordinates and total) of the testing track in 70:30 Ar:CO₂ gas mixture.

931 readout of the OFTPC will consist of 128 pads, their layout is shown in Fig. 1.13.
 932 Time is read out in discrete bins of size $t_{\text{bin}} = 100 \text{ ns}$.

933 As the first approximation, we can neglect the multiplication in the triple-GEM
 934 and assume an ideal charge readout. The time measurement starts at the begin-
 935 ning of the electron/positron simulation (depending on the specific simulation it
 936 can correspond to the production in the target or when entering the OFTPC,
 937 here the specific time doesn't matter too much since the primary particle travels
 938 basically at light speed (30 ps/cm) which is circa immediate given the time bin-
 939 ning). Randomize this time a bit and see what it does to the reconstruction (\rightarrow
 940 Future?). The readout coordinates $(x', y', t) \in \mathcal{R}$ of each ionization electron can
 941 be mapped to the pad coordinates $(n_{\text{pad}}, n_t) \in \mathcal{P}$:

$$n_{\text{pad}} = n : (x', y') \in \left[x_{1,n} - \frac{g}{2}, x_{2,n} + \frac{g}{2} \right] \times \left[y_{1,n} - \frac{g}{2}, y_{2,n} + \frac{g}{2} \right], \quad (3.21)$$

$$n_t = \left\lceil \frac{t}{t_{\text{bin}}} \right\rceil, \quad (3.22)$$

942 where $x, y_{1,n}$ and $x, y_{2,n}$ are the opposing pad corner coordinates, and g is the
 943 gap between the pads (described in detail in Section 1.4.2). This way, the clos-
 944 est pad is assigned to each readout position within the OFTPC volume⁶. Makes
 945 sense since the pads attract the electrons, the inhomogeneity of electric field is
 946 neglected. The number of electrons collected by each pad (i.e., collected charge)
 947 in each time bin is then counted and serves as a weight for the energy recon-
 948 struction. The reconstructed track consists of points for each $(n, n_t) \in \mathcal{P}$, we get

⁶Some positions near the wall are not handled and some pads extend beyond the OFTPC volume. This is where an electric field simulation would come in handy.

949 these by reconstructing the position of a hypothetical electron with the readout
950 coordinates of the pad/time bin center:⁷

$$\mathcal{D} \ni (x, y, z) = \overline{\mathcal{M}} \left(x_{c,n}, y_{c,n}, \left(n_t - \frac{1}{2} \right) t_{\text{bin}} \right). \quad (3.23)$$

951 Examples of positions reconstructed for a single pad are shown in Fig. 3.15. For
952 pads near the magnet poles, the interpolation becomes problematic, due to large
953 distortion. We can use the slower, unoptimized gradient descent search instead,
954 the results are shown in Fig. 3.16. An example of a track from the grid-like testing
955 sample described in Sec. 2.1.2 is shown in Fig. 3.17

⁷Mapping the center of the pad (along with the midpoint of the time bin) is not necessarily the best approach since it might not correspond to the average parameters of an electron with these readout parameters.

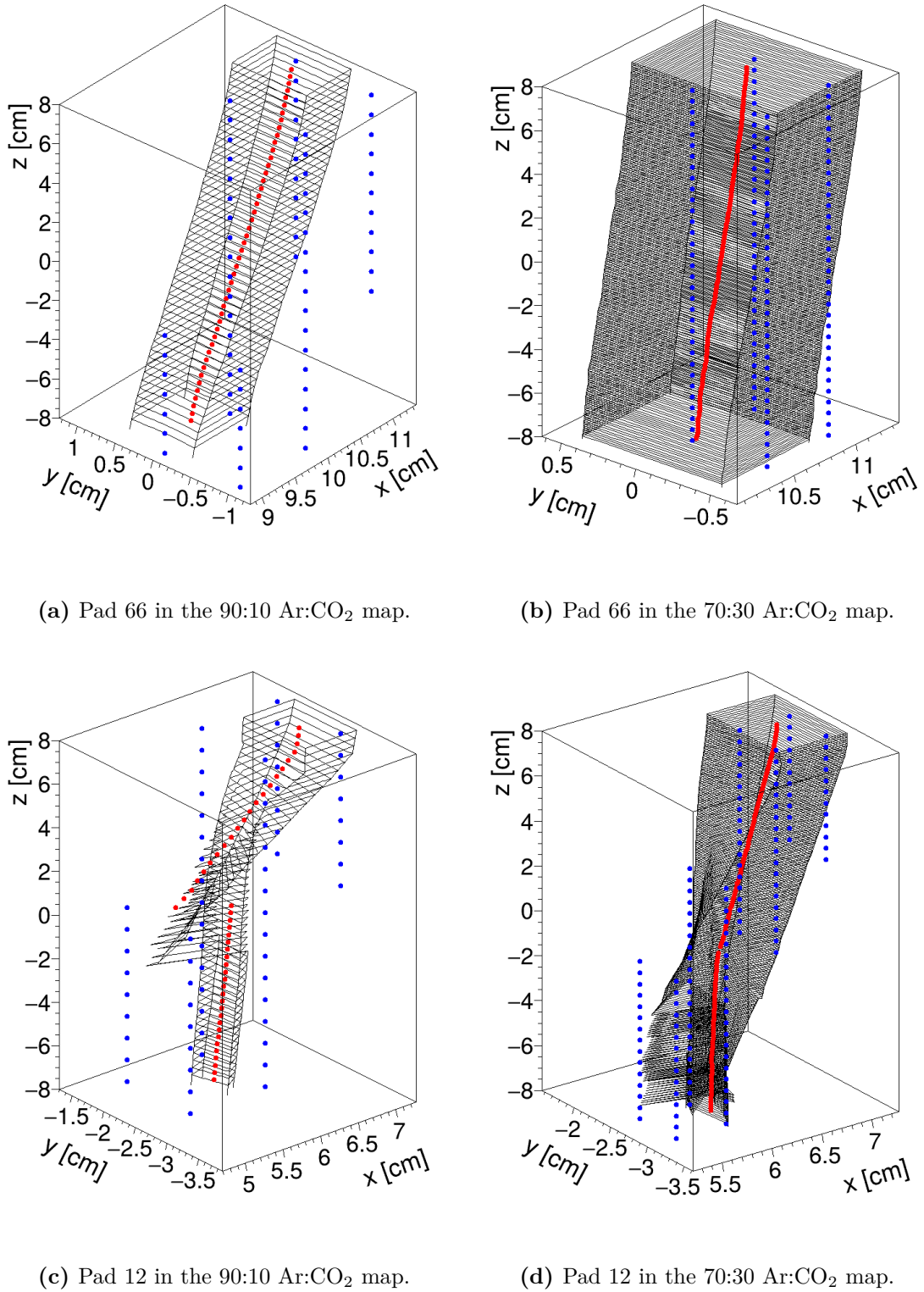


Figure 3.15: Reconstruction of detector coordinates for ionization electrons that are read out in a certain pad (number 66 near the center of the OFTPC, and number 12 near the magnet pole that suffers from large distortion effects, causing issues with interpolation on the inverse grid) and time bin. Boundaries of regions mapped to these discrete coordinates are shown in black, reconstructed center of the pad and time bin is shown in red, and map points used for the center reconstruction are shown in blue. Readout is placed at $z = -8$ cm.

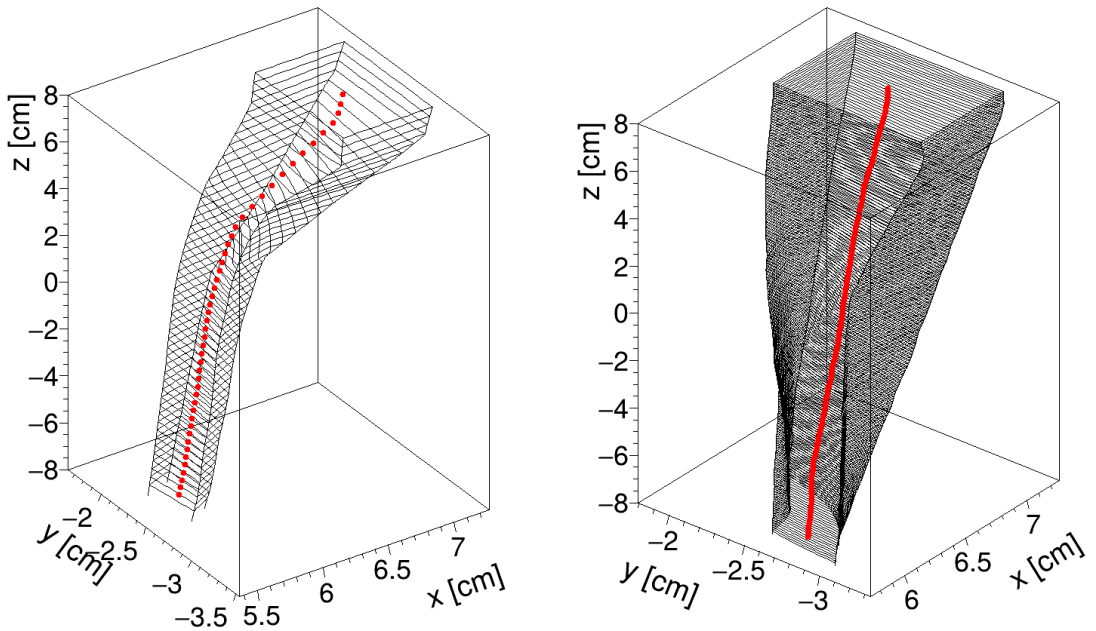


Figure 3.16: Reconstruction of detector coordinates corresponding to pad 12 (near the magnet pole) for different time bins. Unlike Fig. 3.15, we used the gradient descent search, which handles the large distortion better. In its current unoptimized state, these figures took 280 times longer to produce, compared to the interpolation on the inverse grid.

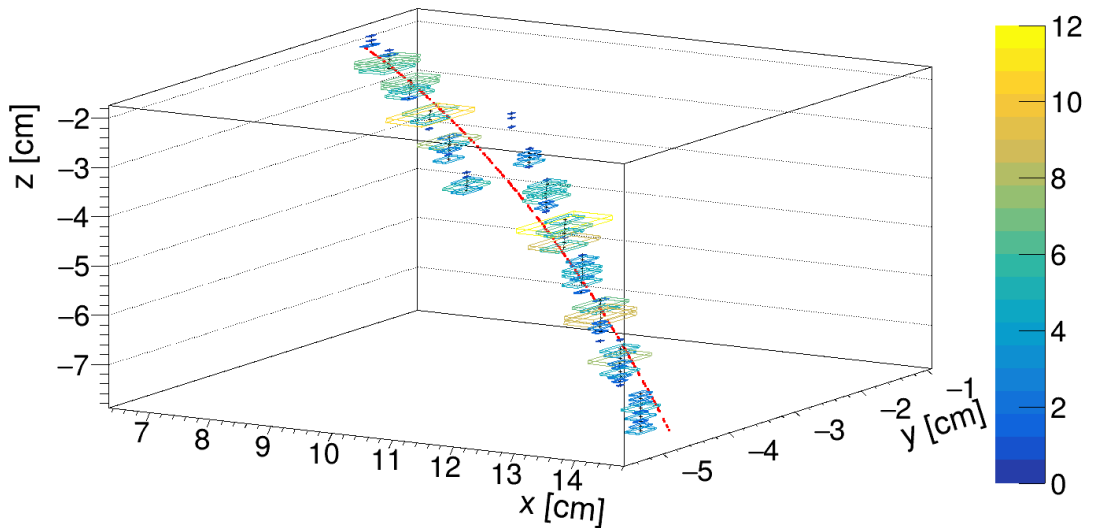


Figure 3.17: Discrete reconstruction of an 8 MeV track from the grid-like testing sample (described in Sec. 2.1.2) with minimal values of θ and ϕ initial direction angles. The simulated ionization vertices are shown in red, the reconstructed track is shown with the colored boxes. The number of electrons in each pad/time bin is denoted with the size of the boxes and their color.

956 4. Energy Reconstruction

957 The second stage is the reconstruction of the particle's energy using a fit of its
958 reconstructed track (see Section 3). We have tested three ways of reconstructing
959 the energy. Fitting is done using the MINUIT algorithm implemented in
960 ROOT [2]. **Cite some CERN article directly on MINUIT, can add a section. Or**
961 **is it done using MIGRAD? The circle and RK4 probably was.**

962 The **Cubic Spline Fit** was a tested and later rejected method of energy
963 reconstruction. It uses smoothly connected piecewise cubic polynomials between
964 uniformly spaced nodes. The reconstructed energy is calculated using the fit
965 parameters by computing the radius of curvature in different points of the fitted
966 curve using the known magnitude of the magnetic field perpendicular to the
967 trajectory. We rejected this method because the tuning of the fit turned out
968 to be unpractical compared to the other used methods. **Reconstructs energy at**
969 **every position (even though the actual energy doesn't change much) and it might**
970 **be slower but no profiling has been done yet. Of course, it wasn't tested on the**
971 **newer track reconstruction methods at all.**

972 The **Circle and Lines Fit** was chosen as an alternative since this corresponds
973 to the shape of a trajectory of a charged particle crossing a finite volume with
974 a homogeneous magnetic field. The energy of the particle can be estimated using
975 the fitted radius and the magnitude of the perpendicular magnetic field in the
976 middle of the TPC.

977 The **Runge-Kutta Fit** uses the 4th order Runge-Kutta numerical integration
978 described in Section 2.2. Initial parameters of the track (including the particle's
979 energy) are optimized so that the integrated trajectory fits to the reconstructed
980 one. This fit can also be performed as a single parameter (i.e., energy) fit if we
981 get the initial position and orientation of the particle on the entrance to the TPC
982 from previous detectors (TPX3 and MWPC, see Section 0.2).

983 4.1 Cubic Spline Fit

984 The first method for the estimation of the kinetic energy of the particle uses
985 a cubic spline fit. We use an electron track simulated using the microscopic
986 simulation, described in detail in Section 2.1.1. The track was reconstructed
987 using the map described in Section 3.2.

988 In order to calculate the spline, we use the class *TSplines3* from ROOT. This
989 allows us to evaluate the spline using the coordinates (x_n, z_n) of each node and
990 the derivatives d_1, d_2 in the first and the last node. We can fit these parameters
991 of a fixed amount of nodes to the simulated trajectory. We use the IMPROVE
992 algorithm provided by the *TMinuit* class in ROOT (**there are some guidelines for**
993 **fonts in MFF UK template (Czech version) that I will eventually apply (see notes**
994 **in the conclusion)). This algorithm attempts to find a better local minimum after**
995 **converging (could reformulate a bit, taken word for word from some manual).**

996 After the fit converges, we calculate an energy estimate using the radius of
997 curvature, which we can extract from the fitted spline equation at every point of
998 the trajectory. The part of the spline corresponding to a given node is defined as

$$z(x) = z_n + b\Delta x + c(\Delta x)^2 + d(\Delta x)^3, \quad (4.1)$$

999 where $\Delta x = x - x_n$ and b, c, d are coefficients. Using this equation, we derive the
1000 radius of curvature¹ as:

$$r(x) = \frac{(1 + z'^2(x))^{\frac{3}{2}}}{z''(x)} = \frac{(1 + (b + 2c\Delta x + 3d(\Delta x)^2)^2)^{\frac{3}{2}}}{2c + 6d\Delta x}. \quad (4.2)$$

1001 Based on the geometry of our detector, we assume that the magnetic field satisfies
1002 $\mathbf{B}(x, 0, z) = (0, B(x, z), 0)$ for a track in the XZ plane. Since the electron is
1003 relativistic, the effect of the electric field on its trajectory is negligible. The
1004 Lorentz force \mathbf{F}_L is then always perpendicular to the momentum of the electron
1005 and acts as a centripetal force \mathbf{F}_c (not quite sure how to handle this then?):

$$\begin{aligned} \mathbf{F}_L &= \mathbf{F}_c, \\ \|e\mathbf{v} \times \mathbf{B}\| &= \frac{\gamma m_e v^2}{r}, \\ ec\beta B &= \frac{E_{0e}\beta^2}{r\sqrt{1 - \beta^2}}, \end{aligned} \quad (4.3)$$

$$\begin{aligned} \sqrt{1 - \beta^2} &= \frac{E_{0e}\beta}{ecBr}, \\ \beta^2(x) &= \left[1 + \left(\frac{E_{0e}}{ecB(x, z(x))r(x)} \right)^2 \right]^{-1}, \end{aligned} \quad (4.4)$$

1006 where e is the elementary charge, c is the speed of light in vacuum, m_e is the rest
1007 mass of electron, $E_{0e} = m_e c^2$ is its rest energy, γ is the Lorentz factor, \mathbf{v} is the
1008 velocity of the electron, and $\beta = \frac{v}{c}$. The kinetic energy for a given point on the
1009 trajectory is then given as

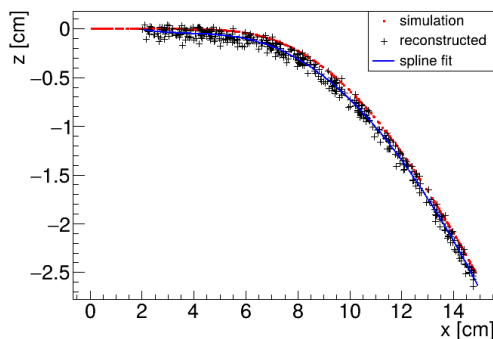
$$E_{\text{kin}}(x) = \left(\frac{1}{\sqrt{1 - \beta^2(x)}} - 1 \right) E_{0e}. \quad (4.5)$$

1010 We could then average these estimates at multiple points (possibly using some
1011 weights to account for the change in accuracy) to get a single value. An example of
1012 the reconstruction for a reconstructed track is shown in Fig. 4.1. This method was
1013 later rejected in favor of the circle and lines fit (the name was already established
1014 at the beginning of the chapter) described in the next section.

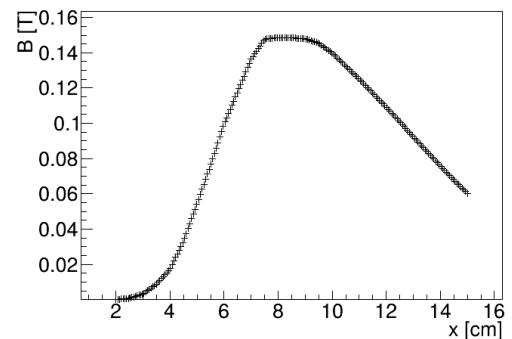
1015 4.2 Circle and Lines Fit

1016 Another way to estimate the particle's kinetic energy is to fit its (??) trajectory
1017 with a circular arc with lines attached smoothly. This shape of trajectory cor-
1018 responds to a movement of a charged particle through a homogeneous magnetic
1019 field perpendicular to the particle's momentum and limited to a certain volume.
1020 In general, the shape of such a trajectory with a non-perpendicularly oriented
1021 momentum is a spiral. In our case, the magnetic field is approximately toroidal
1022 and the particle motion is nearly perpendicular to it (verify, could add some

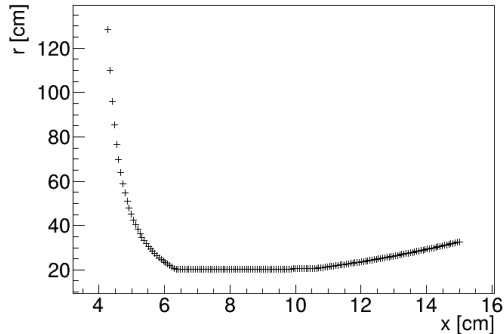
¹For the general formula see https://en.wikipedia.org/wiki/Curvature#Graph_of_a_function.



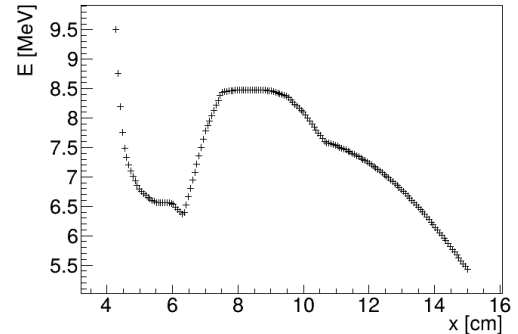
(a) Spline fit of a reconstructed track.



(b) Magnetic field along the track.



(c) Reconstructed radius of curvature along the track.



(d) Reconstructed energy along the track.

Figure 4.1: Energy reconstruction of a 7.51 MeV track in a 70:30 Ar:CO₂ gas mixture (described in detail in Sec. 2.1.1) using a cubic spline fit with four evenly spaced nodes of points reconstructed using the map.

1023 magnetic field plots in different vertical planes; shouldn't have a big effect on the
 1024 reconstructed radius anyway). At first, we tested a 2D version of this fit, then
 1025 we adapted it to 3D.

1026 The field in our detector is not homogeneous, it is therefore not entirely clear
 1027 what value of magnetic field should be used along with the fitted radius (using
 1028 equations 4.4 and 4.5) to get the best estimate for the kinetic energy. Since we
 1029 only use this method as the first iteration of the particle's energy that we later
 1030 refine, an optimal solution of this problem is not required. Instead, we tested two
 1031 options: taking the value of the field in the middle of the fitted circular arc (or
 1032 is it in the middle x of the OFTPC?) and taking the average field along it. We
 1033 haven't really tried to plot this for multiple tracks, but these estimates are saved
 1034 somewhere and could be plotted.

1035 4.2.1 Two-dimensional fit

1036 In the 2D case, the fitted function used for the electron track² described in Sec-
 1037 tion 2.1.1 (one specific track at the time, technically this function doesn't work
 1038 for a curvature that gets outside of the semicircle) is defined as follows:

$$z(x) = \begin{cases} a_1x + b_1 & x < x_1 \\ z_0 + \sqrt{r^2 - (x - x_0)^2} & x_1 \leq x \leq x_2, \\ a_2x + b_2 & x > x_2 \end{cases} \quad (4.6)$$

1039 where $a_{1,2}$ and $b_{1,2}$ are the parameters of the lines, (x_0, z_0) is the center of the cir-
 1040 cle, r is its radius, and $(x_{1,2}, z_{1,2})$ are the coordinates of the function's nodes. That
 1041 means we have 9 parameters ($z_{1,2}$ are not used in the function) along with 2 con-
 1042 tinuity conditions and 2 smoothness conditions (9 parameters of the described
 1043 function, 5 of them independent after taking the conditions into account). For
 1044 the fit, we use the coordinates of the nodes and the radius of the circle, which
 1045 gives us 5 independent parameters (only the radius has to be larger than half
 1046 of the distance between nodes). The continuity conditions (combined with the
 1047 relations for $z_{1,2}$) are

$$z_{1,2} = a_{1,2}x_{1,2} + b_{1,2} = z_0 - \sqrt{r^2 - (x_{1,2} - x_0)^2}, \quad (4.7)$$

1048 the smoothness conditions are

$$a_{1,2} = \frac{x_0 - x_{1,2}}{\sqrt{r^2 - (x_{1,2} - x_0)^2}}. \quad (4.8)$$

1049 Together with the Equation 4.7 we get the values of $b_{1,2}$

$$b_{1,2} = z_{1,2} - a_{1,2}x_{1,2}. \quad (4.9)$$

1050 For the coordinates of the center of the circle, we can use the fact that the center
 1051 has to lie on the axis of its chord. In other words, there is a value of a parameter t
 1052 such that, using the parametric equation of the axis

$$\begin{pmatrix} x_0 \\ z_0 \end{pmatrix} = \begin{pmatrix} \frac{x_1+x_2}{2} \\ \frac{z_1+z_2}{2} \end{pmatrix} + t \begin{pmatrix} \frac{z_2-z_1}{2} \\ \frac{x_1-x_2}{2} \end{pmatrix}. \quad (4.10)$$

²Electron tracks bend towards negative z , we need to use the upper part of the circle.

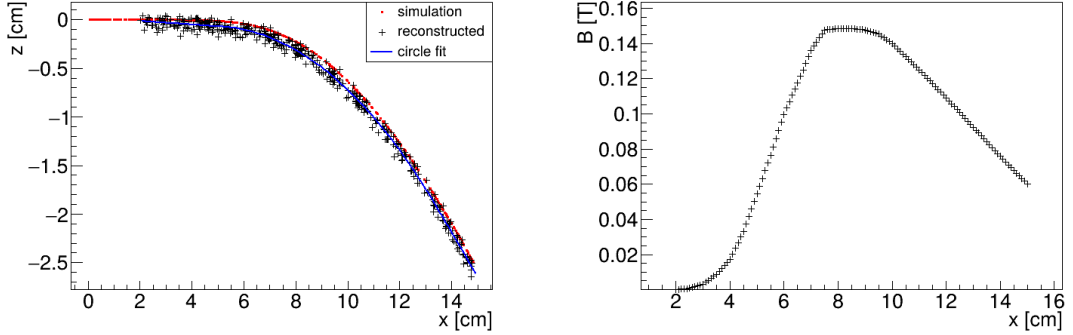


Figure 4.2: Circle and lines 2D energy reconstruction of a 7.51 MeV track in a 70:30 Ar:CO₂ gas mixture (described in detail in Sec. 2.1.1) reconstructed with the map. The fitted position of the nodes is $(x_1, z_1) = (5.20, -0.07)$ cm and $(x_2, z_2) = (14.43, -1.93)$ cm, the radius is $r = 20.79$ cm. The resulting energy is 7.70 MeV, the magnetic field along the track is shown on the right.

1053 At the same time, the center has to be in a distance of r from the nodes:

$$\begin{aligned} (x_1 - x_0)^2 + (z_1 - z_0)^2 &= r^2, \\ \left(\frac{x_1 - x_2}{2} + \frac{z_1 - z_2}{2} t \right)^2 + \left(\frac{z_1 - z_2}{2} + \frac{x_2 - x_1}{2} t \right)^2 &= r^2, \\ \left(\left(\frac{x_2 - x_1}{2} \right)^2 + \left(\frac{z_2 - z_1}{2} \right)^2 \right) t^2 + \left(\frac{x_2 - x_1}{2} \right)^2 + \left(\frac{z_2 - z_1}{2} \right)^2 - r^2 &= 0. \end{aligned} \quad (4.11)$$

1054 Since our electron track bends towards negative z and $x_2 > x_1$, we only care
1055 about the solution with $t > 0$

$$t = \sqrt{\frac{r^2}{\left(\frac{x_2-x_1}{2}\right)^2 + \left(\frac{z_2-z_1}{2}\right)^2} - 1}, \quad (4.12)$$

$$\begin{aligned} x_0 &= \frac{x_1 + x_2}{2} + \frac{z_2 - z_1}{2} \sqrt{\frac{r^2}{\left(\frac{x_2-x_1}{2}\right)^2 + \left(\frac{z_2-z_1}{2}\right)^2} - 1}, \\ z_0 &= \frac{z_1 + z_2}{2} - \frac{x_2 - x_1}{2} \sqrt{\frac{r^2}{\left(\frac{x_2-x_1}{2}\right)^2 + \left(\frac{z_2-z_1}{2}\right)^2} - 1}. \end{aligned} \quad (4.13)$$

1056 The function defined in Equation 4.6 along with equations 4.8, 4.9, and 4.13
1057 derived using the continuity and smoothness conditions (combined with the relations
1058 for $z_{1,2}$) fully define our fitted function with parameters $r, x_{1,2}, z_{1,2}$.

1059 For the calculation of kinetic energy from the radius of the circle, we use the
1060 value of the magnetic field in the middle of the OFTPC (this could be further
1061 optimized in the future). An example of a fit of vertices reconstructed with the
1062 map is shown in Fig. 4.2. Use GeoGebra schematics to generate a picture of 2D
1063 geometry.

1064 4.2.2 Three-dimensional fit

1065 In three dimensions, the shape of a trajectory of a charged particle in a uniform
1066 magnetic field is a cylindrical helix. Nevertheless, since we assume that the

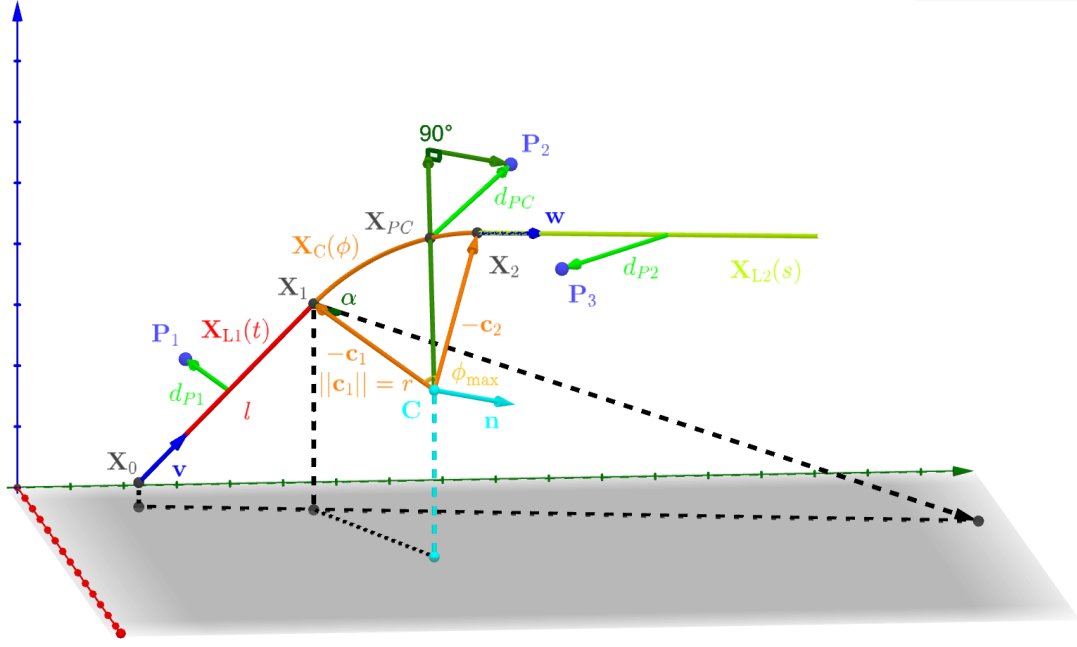


Figure 4.3: Visualization of the 3D geometry of the Circle and Lines Fit and its parameters. Projection of some points on the XY plane is shown to better display the spatial arrangement.

field is approximately perpendicular to the particle's momentum at all times, we will further approximate the trajectory with a circular arc $\mathbf{X}_C(\phi)$ (with lines $\mathbf{X}_{L1}(t), \mathbf{X}_{L2}(s)$ attached smoothly).

We assume that the initial position $\mathbf{X}_0 = (x_0, y_0, z_0)$ and direction (given by the spherical angles θ, φ , see Sec. 1.4.2) are known, since this information will be provided by TPX3 and MWPC layers. We could further refine it at the end of the current algorithm with some kind of global fit (all detector layers). The fit then has four free parameters (see Fig. 4.3):

- the length of the first line l (as measured from the initial position),
- the radius of the circular arc r ,
- the central angle of the arc $\phi_{\max} \in [0, 2\pi]$,
- the direction of the curvature given by the angle $\alpha \in [0, 2\pi]$ (right-handed with respect to the particle direction, $\alpha = 0$ if the particle curves towards negative z in a plane given by \hat{z} and the direction vector).

Using these parameters, we can derive a parametrization of the whole curve. Let \mathbf{v} be the initial unit direction vector, i.e., using the spherical angles

$$\mathbf{v} = (\cos \varphi \cos \theta, \sin \varphi \cos \theta, \sin \theta)^T, \quad (4.14)$$

then we can parameterize the first line as follows:

$$\mathbf{X}_{L1}(t) = \mathbf{X}_0 + t\mathbf{v} \quad t \in [0, l]. \quad (4.15)$$

This gives us the starting point of the arc

$$\mathbf{X}_1 = \mathbf{X}_{L1}(l) = \mathbf{X}_0 + l\mathbf{v}. \quad (4.16)$$

The vector \mathbf{c}_1 that lies in the plane of curvature and points from \mathbf{X}_1 to the center of curvature can be calculated using a composition of rotations. First, we rotate \mathbf{v}

1087 to point in the $\hat{\mathbf{x}}$ direction, the normal for $\alpha = 0$ than points in the $-\hat{\mathbf{z}}$ direction,
 1088 we apply the α rotation and reverse the rotations into the $\hat{\mathbf{x}}$ direction: (parameters
 1089 are explained in the bullet points above)

$$\begin{aligned}\mathbf{c}_1 &= R_z(\varphi)R_y(-\theta)R_x(\alpha)R_y\left(\frac{\pi}{2}\right)R_y(\theta)R_z(-\varphi)\mathbf{v}, \\ &= R_z(\varphi)R_y(-\theta)R_x(\alpha)(-\hat{\mathbf{z}}), \\ &= \begin{pmatrix} \cos \varphi & -\sin \varphi & 0 \\ \sin \varphi & \cos \varphi & 0 \\ 0 & 0 & 1 \end{pmatrix} \begin{pmatrix} \cos \theta & 0 & -\sin \theta \\ 0 & 1 & 0 \\ \sin \theta & 0 & \cos \theta \end{pmatrix} \begin{pmatrix} 1 & 0 & 0 \\ 0 & \cos \alpha & -\sin \alpha \\ 0 & \sin \alpha & \cos \alpha \end{pmatrix} \begin{pmatrix} 0 \\ 0 \\ -1 \end{pmatrix}, \quad (4.17) \\ &= \begin{pmatrix} -\sin \alpha \sin \varphi + \cos \alpha \cos \varphi \sin \theta \\ \sin \alpha \cos \varphi + \cos \alpha \sin \varphi \sin \theta \\ -\cos \alpha \cos \theta \end{pmatrix}.\end{aligned}$$

1090 Signs should be correct because right-handed rotation around y rotates z into x
 1091 and this one is the opposite. Seems like in this part of the code θ is actually taken
 1092 from the pole. Instead of the equator plane. Similarly by rotating $\hat{\mathbf{y}}$, we can get
 1093 the normal vector $\mathbf{n} = \mathbf{v} \times \mathbf{c}_1$ perpendicular to the plane of the trajectory:

$$\mathbf{n} = R_z(\varphi)R_y(-\theta)R_x(\alpha)\hat{\mathbf{y}} = \begin{pmatrix} -\cos \alpha \sin \varphi - \sin \alpha \cos \varphi \sin \theta \\ \cos \alpha \cos \varphi - \sin \alpha \sin \varphi \sin \theta \\ \sin \alpha \cos \theta \end{pmatrix}. \quad (4.18)$$

1094 This allows us to express the coordinates of the center \mathbf{C} of the circular arc:

$$\mathbf{C} = \mathbf{X}_1 + r\mathbf{c}_1. \quad (4.19)$$

1095 We can then get the parametrization and the endpoint of the circular arc using
 1096 Rodrigues' rotation formula: (all parameters explained in the bullet points above)

$$\begin{aligned}\mathbf{c}_2 &= \mathbf{c}_1 \cos \phi_{\max} + (\mathbf{n} \times \mathbf{c}_1) \sin \phi_{\max} + \mathbf{n}(\mathbf{n} \cdot \mathbf{c}_1)(1 - \cos \phi_{\max}), \\ &= \mathbf{c}_1 \cos \phi_{\max} - \mathbf{v} \sin \phi_{\max},\end{aligned} \quad (4.20)$$

$$\mathbf{X}_C(\phi) = \mathbf{C} - r(\mathbf{c}_1 \cos \phi - \mathbf{v} \sin \phi) \quad \phi \in [0, \phi_{\max}], \quad (4.21)$$

$$\mathbf{X}_2 = \mathbf{X}_C(\phi_{\max}) = \mathbf{C} - r\mathbf{c}_2, \quad (4.22)$$

1097 and if we define the direction vector of the second line, we also get its parametriza-
 1098 tion

$$\mathbf{w} = \mathbf{v} \cos \phi_{\max} + (\mathbf{n} \times \mathbf{v}) \sin \phi_{\max} = \mathbf{v} \cos \phi_{\max} + \mathbf{c}_1 \sin \phi_{\max}, \quad (4.23)$$

$$\mathbf{X}_{L2}(s) = \mathbf{X}_2 + s\mathbf{w} \quad s \in [0, \infty). \quad (4.24)$$

1099 The fit is performed as a (weighted) least square minimization (MIGRAD
 1100 ROOT), therefore we need to derive the distance of any point \mathbf{P} to the fitted
 1101 curve. For the first line, we simply compute the parameter value of the closest
 1102 point on the line:

$$\begin{aligned}t_P &= \mathbf{v} \cdot (\mathbf{P} - \mathbf{X}_1), \\ d_{P1} &= \|\mathbf{P} - \mathbf{X}_{L1}(t_P)\|.\end{aligned} \quad (4.25)$$

1103 If the parameter value is outside of its bounds defined above, we take the boundary
 1104 value instead. The distance to the second line is computed likewise. For the

Parameter	Fit of microscopic track	Fit of reconstructed track
l	-0.27(90) cm	-0.26(62) cm
α	-6.2(23) $^\circ$	-8.2(23) $^\circ$
r	17.2(48) cm	16.8(28) cm
ϕ_{\max}	26.1(72) $^\circ$	20.5(36) $^\circ$
$E_{\text{reco}}^{\text{mid}}$	7.93 MeV	7.35 MeV
$E_{\text{reco}}^{\text{avg}}$	7.80 MeV	8.19 MeV

Table 4.1: 3D circle fit parameters of an 8 MeV track from the grid-like testing sample (described in Sec. 2.1.2) with minimal values of θ and ϕ initial direction angles.

1105 circular arc (**specific circular arc in the fit**), we find the closest point (**on the arc**)
 1106 by projecting the center connecting line onto the arc plane:

$$\mathbf{X}_{PC} = \mathbf{C} + r \frac{(\mathbf{P} - \mathbf{C}) - (\mathbf{n} \cdot (\mathbf{P} - \mathbf{C}))\mathbf{n}}{\|(\mathbf{P} - \mathbf{C}) - (\mathbf{n} \cdot (\mathbf{P} - \mathbf{C}))\mathbf{n}\|}, \quad (4.26)$$

$$d_{PC} = \|\mathbf{P} - \mathbf{X}_{PC}\| \quad (4.27)$$

1107 If the point \mathbf{X}_{PC} lies outside of the arc, distance to the closest endpoint is taken
 1108 instead. Sometimes (rarely?) the distance might be underestimated when the
 1109 point is closer to the circle, the arc is a part of, than to the curve. I tried to
 1110 fix this, but it breaks the fit and makes the results worse. The shortest dis-
 1111 tance out of d_{P1}, d_{PC}, d_{P2} is then taken as the distance to the curve. **TVirtual-**
 1112 **Fitter+MIGRAD, maximal num of iterations, toleration. Different uncertainties**
 1113 **in x, y, z not taken into account.**

1114 For the calculation of the kinetic energy from the radius, we implemented two
 1115 variants:

- 1116 1. using the perpendicular projection to the plane of the trajectory of magnetic
 1117 field at a point, where the circular arc crosses the central plane of the
 1118 OFTPC (parallel to the YZ plane), and
- 1119 2. using the average value of this projection along the circular arc.

1120 This way, we get two energy estimates $E_{\text{reco}}^{\text{mid}}$ and $E_{\text{reco}}^{\text{avg}}$. If needed, this choice
 1121 can be further optimized, however, since this method will only provide an initial
 1122 guess of the kinetic energy for the more sophisticated, and computationally heavy
 1123 Runge-Kutta fit, it is not necessary to reach the best precision, and fast solutions
 1124 are preferred.

1125 An example of a fitted track (both the actual initial points and the discrete
 1126 reconstruction of the track) from the microscopic grid-like testing sample (de-
 1127 scribed in Sec. 2.1.2) is shown in Fig. 4.4, the fitted parameters are given in
 1128 Table 4.1.

1129 **Fit details (parameter bounds, initial setting).**

1130 4.2.3 Testing on a Runge-Kutta sample

1131 The three dimensional circle and lines fit was tested on a sample of Runge-Kutta
 1132 tracks with randomized parameters described in Section 2.2.1. These tracks of pri-
 1133 mary electrons and positrons consist of points calculated with the RK4 algorithm

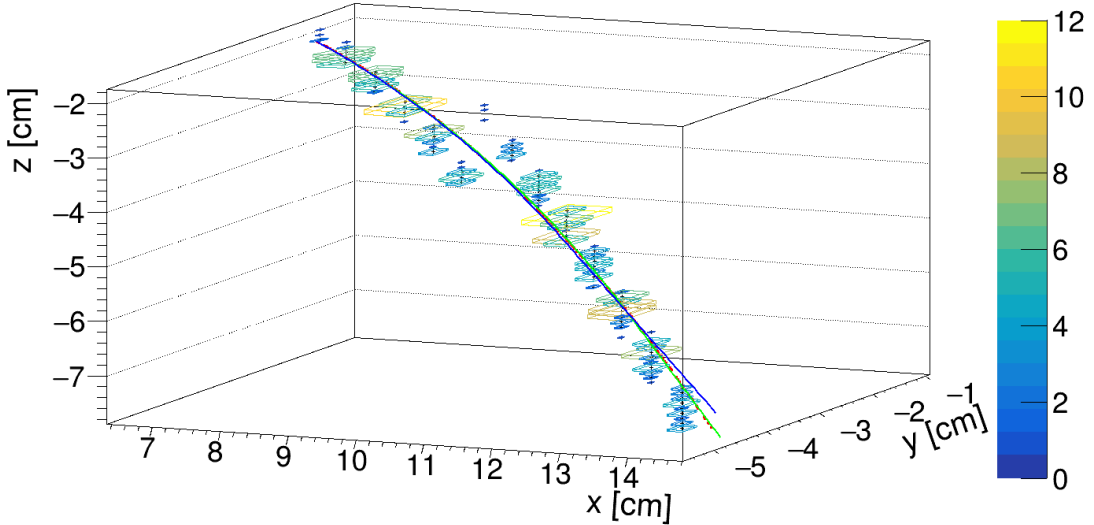


Figure 4.4: 3D circle fit of an 8 MeV track (red points) from the grid-like testing sample (described in Sec. 2.1.2) with minimal values of θ and ϕ initial direction angles. Both fits of the original (green) and reconstructed track (blue) are shown. Resulting parameter values are given in Table 4.1.

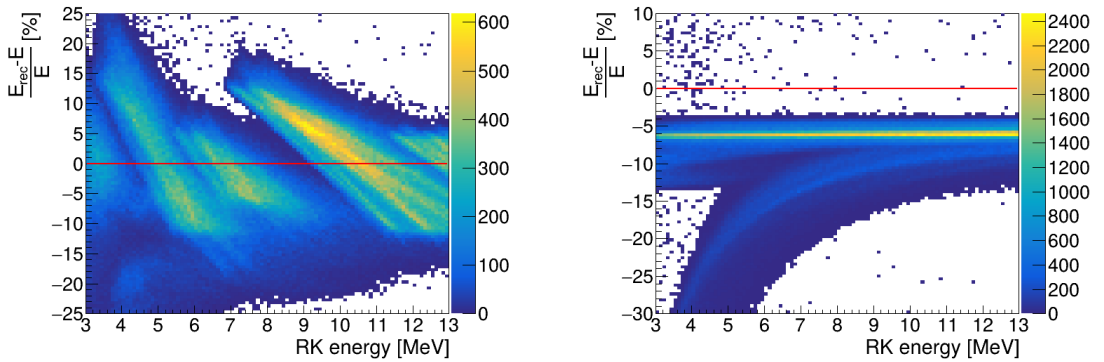
for a given time step. The parameter ranges in the MIGRAD minimizer have to be carefully tuned, simple exclusion of pathologic values can lead to convergence towards an edge value. After the tuning, only 4163 out of 1 000 000 tracks failed to converge to energy within 2 MeV from the simulation. We compared the two methods of choosing the magnetic fields. The resulting relative errors of reconstructed energy are shown in Fig. 4.5. The average field method systematically underestimates the particle's energy, but has \sim 25 times lower FWHM.

4.3 Runge-Kutta Fit

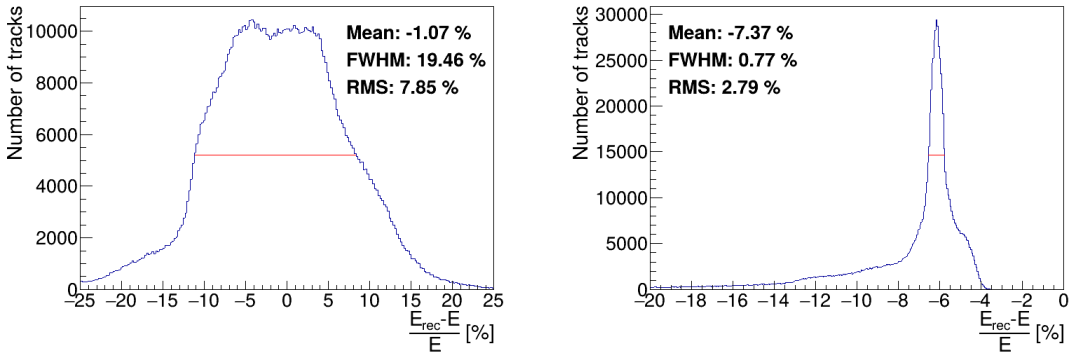
The Runge-Kutta fit uses the Runge-Kutta 4th order (RK4) numerical integration of the equation of motion (see Section 2.2) to find the best values of the track parameters – the track origin, initial velocity direction and the kinetic energy. In order to speed up the energy reconstruction, an initial guess of these parameters can be obtained from the 3D circle fit described in the previous section. Furthermore, assuming we know the track origin and orientation, we can perform a single parameter fit of the kinetic energy (**do some profiling and show that it is faster – below in the microscopic testing**).

The fit is performed as a least square minimization of the (weighted) distances of the track points (true ionization vertices from the simulation or reconstructed points). The simulated RK4 track consists of line segments with known endpoints, therefore we can calculate the distance of a point from this segment analogically to Equation 4.25 with \mathbf{v} given as a unit vector in the direction of the segment.

We need to find the segment with the lowest distance. We assume, that the distance $d_{\mathbf{P}}(\tau)$ of a point \mathbf{P} to the point on the track (a curve parameterized by the proper time τ) $\mathbf{X}(\tau)$ has a single minimum (local and global), no local



(a) Dependence of relative error on simulated energy for both magnetic field selection methods.



(b) Overall relative error for both magnetic field selection methods. Freedman-Diaconis rule was used for bin width selection [46].

Figure 4.5: Relative error of the energy of Runge-Kutta tracks reconstructed with the 3D circle and lines fit. The middle field (left) and the average field (right) methods are compared. Dependence on the initial direction angles θ and φ is small in comparison.

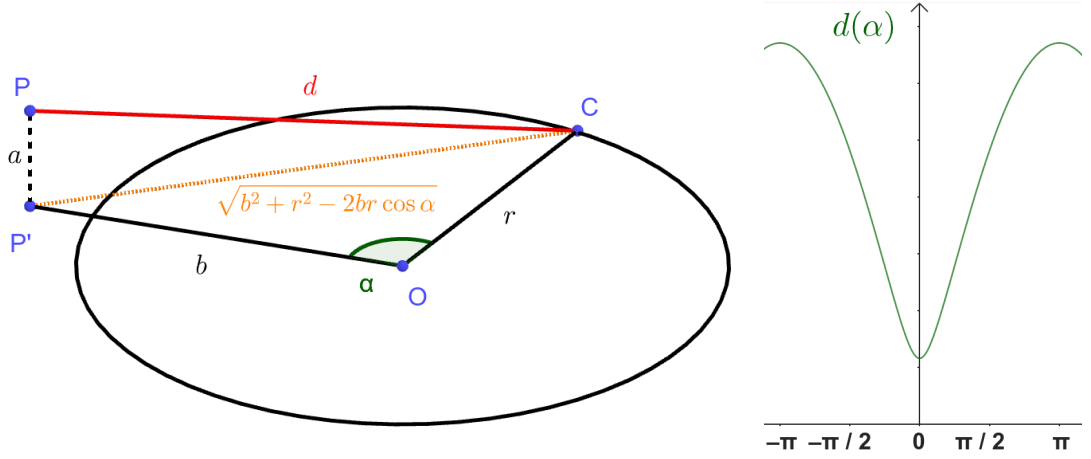


Figure 4.6: Demonstration of the convexity of the distance function $d(\alpha)$ for a circular track (see Equation 4.29).

1158 maximum (except the interval endpoints) and no saddle point

$$\exists! \tau_{\min} \in [0, \tau_N]: (\forall \tau \in [0, \tau_N]: d_{\mathbf{P}}(\tau) \geq d_{\mathbf{P}}(\tau_{\min})) \vee \frac{dd_{\mathbf{P}}}{d\tau}(\tau_{\min}) = 0, \quad (4.28)$$

1159 where N is the number of RK4 steps. This is a reasonable assumption for a track
 1160 with an approximate shape of a circular arc with a radius r , since the distance d
 1161 from a point \mathbf{C} on the corresponding circle of a point \mathbf{P} offset by a from the arc
 1162 plane and by b from the arc's center when projected on its plane is given by the
 1163 law of cosines:

$$d^2 = a^2 + b^2 + r^2 - 2br \cos \alpha, \quad (4.29)$$

1164 where α is the angle between points \mathbf{C} and \mathbf{P} as seen from the center of the arc
 1165 (see Fig. 4.6). This function is strictly convex for $\alpha \in (-\frac{\pi}{2}, \frac{\pi}{2})$ and in our case,
 1166 the center of the arc lies outside of the detector and α is restricted to a small
 1167 interval around zero (especially considering that the initial guess should make the
 1168 fitted trajectory reasonably close to any relevant point, in the worst-case scenario,
 1169 the distance is overestimated which should keep the fit from converging to such
 1170 solutions).

1171 In a more general case, if we consider the vector $\mathbf{a}(\tau) = \mathbf{P} - \mathbf{X}(\tau)$ whose size
 1172 is $\|\mathbf{a}(\tau)\| = d_{\mathbf{P}}(\tau)$, then we get

$$2d_{\mathbf{P}} \frac{dd_{\mathbf{P}}}{d\tau} = \frac{dd_{\mathbf{P}}^2}{d\tau} = 2\mathbf{a} \cdot \frac{d\mathbf{a}}{d\tau} = -2\mathbf{a} \cdot \frac{d\mathbf{X}}{d\tau}, \quad (4.30)$$

1173 therefore for the derivative of $d_{\mathbf{P}}(\tau)$ to be zero, $\mathbf{a}(\tau)$ has to be perpendicular to
 1174 the tangent of the track. In 3D, for a given $\mathbf{X}(\tau)$, this condition restricts \mathbf{P} to
 1175 a plane. This means that on a curving track, for any two points $\mathbf{X}(\tau_1), \mathbf{X}(\tau_2)$
 1176 with non-parallel tangents, we can find a point \mathbf{P} that has $\frac{dd_{\mathbf{P}}}{d\tau}(\tau_1) = \frac{dd_{\mathbf{P}}}{d\tau}(\tau_2) =$
 1177 $= 0$, which violates the assumption 4.28. If we have a circle-and-lines track as
 1178 described in the previous sections, such a point has to lie outside of the circular
 1179 sector given by the arc.

1180 For a planar track $\mathbf{X}(\tau) = (X_1(\tau), X_2(\tau))$, the envelope of all its normals is
 1181 the evolute of the curve (i.e., the set of centers of all its osculating circles). If the

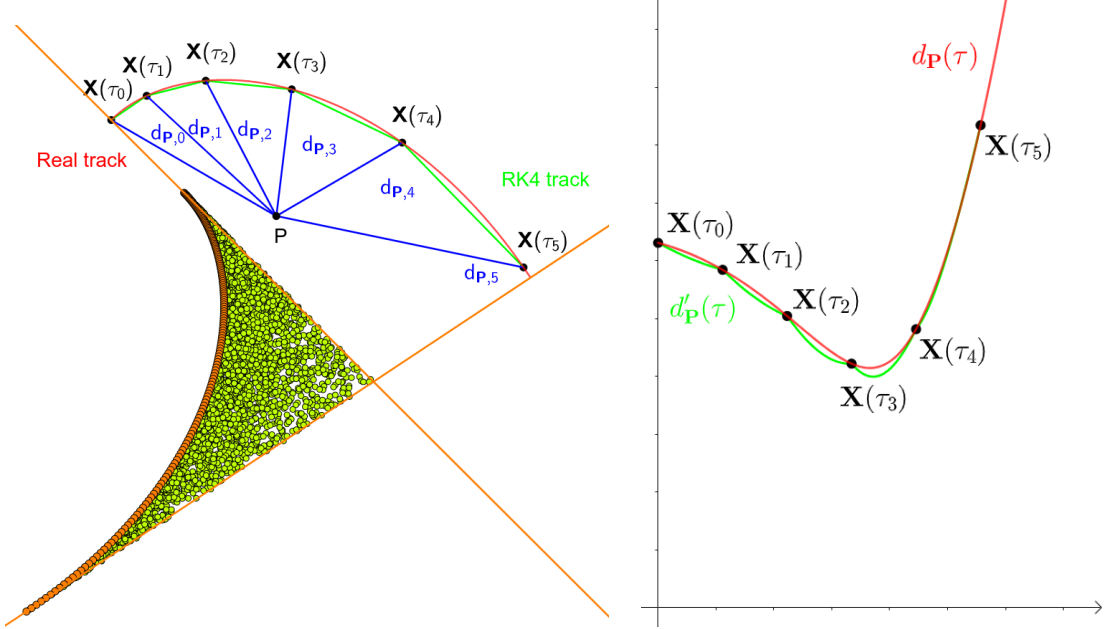


Figure 4.7: An example track (red) with a polygonal chain approximation (green, representing a RK4 simulation). The distance of the point \mathbf{P} from the chain is found using a binary search among the distances to the vertices $d_{\mathbf{P}}(\tau_i)$ (blue) and subsequently calculating the distance to segments neighboring the found vertex (thus finding the minimum of the function $d'_{\mathbf{P}}(\tau)$, function $d_{\mathbf{P}}(\tau)$ for the actual track is showed for reference). This approach works if the condition 4.28 is satisfied, which is not the case for a point from the green area bordered by the normals at endpoints and the evolute of the track (orange).

1182 track has a monotonous tangent angle

$$\alpha(\tau) = \text{atan} \frac{\frac{dX_2}{d\tau}}{\frac{dX_1}{d\tau}} \quad (4.31)$$

1183 with minimal and maximal α differing by less than π (i.e., the track changes
 1184 direction by less than 180°), then all intersections of the track's normals must lie
 1185 in an area bordered by the evolute and the normals at the beginning and the end
 1186 of the curve (from their intersection with the evolute to their mutual intersection,
 1187 see Figs. 4.7 and 4.8). Together, these three boundaries define a closed shape that
 1188 will lie outside of the OFTPC for a typical track in our detector³.

1189 With the assumption 4.28, we can find the segment on the RK4 track with
 1190 the lowest distance to a given point \mathbf{P} using a binary search algorithm. Let the
 1191 distance of the point from the n -th vertex be $d_{\mathbf{P},n} = d_{\mathbf{P}}(\tau_n)$. Then the difference
 1192 $\Delta d_{\mathbf{P},n} = d_{\mathbf{P},n} - d_{\mathbf{P},n-1}$ satisfies

$$\begin{aligned} \Delta d_{\mathbf{P},n} &< 0 & \forall n \text{ such that } \tau_n < \tau_{\min}, \\ \Delta d_{\mathbf{P},n} &> 0 & \forall n \text{ such that } \tau_{n-1} > \tau_{\min}. \end{aligned} \quad (4.32)$$

1193 Therefore, we can search for the segment containing $d_{\mathbf{P},\min} = d_{\mathbf{P}}(\tau_{\min})$ with binary
 1194 search starting with $\Delta d_{\mathbf{P},1}$ and $\Delta d_{\mathbf{P},N}$, then calculate the difference $\Delta d_{\mathbf{P},m}$ for

³The smallest anticipated radius of curvature is 39 cm for an electron or positron with a kinetic energy 3 MeV in a 0.3 T magnetic field. All points in the exclusion area must be farther from the track and therefore outside the OFTPC.

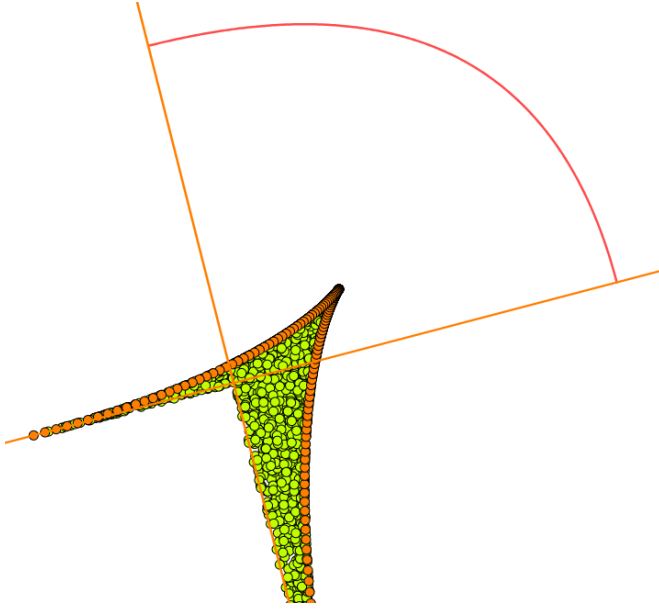


Figure 4.8: An exclusion area (green) of a track (red) bordered by its evolute and the normals at endpoints (orange), where the assumption 4.28 is violated. Unlike the track in Fig. 4.7, this track has a minimal curvature point in the middle, corresponding to the cusp on its evolute.

1195 the middle index $m = \left\lfloor \frac{N+1}{2} \right\rfloor$. If $\Delta d_{P,m} > 0$ (minor bug in the implementation
 1196 – if the value for the maximal index is negative, it shouldn't change anything),
 1197 we can replace the higher index with m , otherwise we replace the lower index.
 1198 The search stops when the difference between the minimal and maximal index is
 1199 one. Would it be better if they were the same (maybe not)? Then the minimal
 1200 value is $d_{P,n-1}$ or $d_{P,N}$ and we can take the minimum of the distances from the two
 1201 segments connected to $n - 1$. Currently taking the maximal index (and starting
 1202 at $N - 2$ maximal index $\leftrightarrow N - 1$ -th point), this should be equivalent, since either
 1203 $\Delta d_{P,\max} > 0$ (in the code is equivalent to max-1 here) or we are at $N - 1$. The
 1204 minimum of the two distances still taken.

1205 Same details with MIGRAD etc. as previously.

1206 4.3.1 Testing on a microscopic sample

1207 The Runge-Kutta fit together with the 3D circle-and-lines pre-fit was tested on
 1208 a sample of tracks simulated using the microscopic simulation described in Sec-
 1209 tion 2.1. At first, few tracks with randomized initial parameters (same as the
 1210 Runge-Kutta sample in Section 2.2.1) were generated for preliminary testing.
 1211 Later, a sample with a grid-like distribution of track parameters was generated
 1212 (see Section 2.1.2 for details).

1213 Initial parameters of the HEED track (also should be in the first testing track).
 1214 Initial parameters set in the circle fit (if electron set alpha one way, otherwise
 1215 other way) and parameter bounds.

Conclusion

We have developed and implemented several methods for the reconstruction of electron and positron trajectories inside the Orthogonal Fields Time Projection Chambers (OFTPCs) that will be used in the X17 project at the Institute of Experimental and Applied Physics, Czech Technical University in Prague (IEAP CTU) to confirm or disprove the ATOMKI anomaly [11]. We tested these methods on simulated tracks and made a preliminary estimate of achievable energy resolution.

We used the Garfield++ toolkit [1] for simulations in combination with the ROOT framework [2] for data analysis and visualization. Some of our more demanding simulations were run on the MetaCentrum grid [3]. The main method of track simulation was the microscopic simulation (provided by the **Avalanche-Microscopic** class), which follows ionization electrons from collision to collision.

Track Reconstruction

The inhomogeneous magnetic field created by permanent magnets is perpendicular to the electric field of the chambers and has a significant effect on the drift of ionization electrons (as demonstrated in Sec. 3.1). For this reason, we created the ionization electron map, i.e., a mapping from the detector space \mathcal{D} (coordinates (x, y, z)), where the initial positions of ionization electrons lie, to the readout space \mathcal{R} (coordinates (x', y', t)), where their endpoints on the readout plane lie. The map was simulated using the microscopic simulation. One hundred electrons with low initial velocity were simulated for each point on a Cartesian grid to get their mean readout coordinates and their covariance. Two gas mixtures 90:10 and 70:30 Ar:CO₂ were compared. In the former, the drift velocity is significantly higher, leading to increased effect of the magnetic field and larger diffusion (see, for example, Fig. 3.9a).

To use the map in reconstruction, we have to invert it. We implemented two methods – a gradient descent algorithm that finds a minimum in the trilinearly interpolated map, and a polynomial interpolation on the inverse grid in the readout space (where we know the inverse from the simulation). Both methods reach almost identical result for the testing track, while the latter is much faster, does not require optimization of parameters, and can be accelerated by precalculating the interpolation coefficients in the future if needed. The reconstruction was shown to be accurate with less than 2 mm FWHM, although a slight shift in the z -coordinate was detected when accounting for different initial velocities of the ionization electrons (see Figs. 3.13 and 3.14).

The discrete reconstruction takes into account the anode segmentation into pads and the finite size of the time bins. It neglects the gaps between the pads and assumes an ideal readout of charge, counting each individual electron hitting the pad. Charge multiplication in the triple-GEM stack used in the OFTPC is not taken into account. For each pad/time-bin combination, we use the map inversion to reconstruct its center. Reconstruction of detector coordinates corresponding to electrons hitting the pad 12 near the magnet pole (Figs. 3.15 and 3.16) show that interpolation on the inverse grid behaves pathologically for large distortions, unlike the much slower gradient descent algorithm. **Or maybe there is a problem**

1261 in the algorithm??? Actually not quite sure, what causes this behavior.

1262 Energy Reconstruction

1263 To reconstruct energy of a particle in a OFTPC, we assess its curvature in the
1264 inhomogeneous magnetic field. Preliminary tests were done using tracks recon-
1265 structed with the map with no discretization. At first, we tested a cubic spline
1266 fit, where the radius of curvature can be determined analytically. This approach
1267 turned out to be unpractical because of relatively low speed and necessity to cre-
1268 ate the energy estimate from the radius and magnetic field at different points on
1269 the track (see Fig. 4.1).

1270 Another tested approach (at first as a 2D version without pads, later in 3D
1271 with pads) was the fit with circular arc with smoothly attached lines, which is
1272 the shape of trajectory of a particle crossing a finite volume with homogeneous
1273 magnetic field oriented perpendicularly to the particles velocity vector. This way
1274 we get a single reconstructed radius of curvature, however, since the magnetic field
1275 varies greatly along the track inside the OFTPC volume, it is not clear, which
1276 value of magnetic field to use to calculate the energy. Two simple estimates were
1277 implemented:

- 1278 1. using the value at the point, where the track crosses the middle x -coordinate, |
1279 and
- 1280 2. using the average value along the circular arc in the fit,
1281 in both cases, only the component perpendicular to the plane of the fit is consid-
1282 ered. The three dimensional version of the fit has four free parameters (radius,
1283 length of the first line, length of the circular arc, and rotation angle around the
1284 first line). In order for the fit to converge correctly in all cases, the parameter
1285 bounds have to be set carefully. Disallowing pathological values that are not
1286 expected for any real track may cause the MIGRAD algorithm to converge at
1287 the bound. The fit was successfully tested on a sample of Runge-Kutta tracks
1288 described in Sec. 2.2.1; the results in Fig. 4.5 show that the average field estimate
1289 systematically underestimates the energy of the track, but its FWHM is much
1290 smaller than that of the middle field estimate.

1291

1292 Notes

1293 General notes about the thesis:

- 1294 • Check that all of the classes and other code are marked the same way in
1295 the text. I used italics somewhere, could use different font for this instead.
- 1296 • Check unbreakable space in front of articles. Remove excessive article usage
1297 with proper nouns.
- 1298 • Currently using margins for single-sided printing (bigger on the left side).
- 1299 • Check that present tense is used
- 1300 • Active vs passive voice usage
- 1301 • American English quotation marks (") instead of British English (').

- Some of the overfull hbox warnings might change if duplex printing is used (they generate black rectangles on the edge of the page), leaving them be for now
- Check nobreakdash usage (is it always necessary)
- Check capitalized references (e.g., Figure, Section, Equation)
- Check $\backslash(...\backslash)$ math mode instead of $\$...$$. (actually unlike $\backslash[...\backslash]$ math mode, there is apparently no real benefit to this clumsy syntax)
- Use siunitx package to ensure correct formatting, physics package for derivatives.
- Check other stuff that's written in the MFF UK template. Apparently it has since been updated and there are some differences (check for them).
- Check correct subscripts in equation (italics vs no italics)
- Consistent bold marking of points/vectors
- Correct footnotes (capital letters, etc.).
- Might have to mention GeoGebra as per the non-commercial license agreement (Made with GeoGebra®) – maybe put it into acknowledgments next to the MetaCentrum credit? And list all of the figures where GeoGebra was used?
- Maybe make some section outside of References specifically for literature? (such as the old CERN TPC review, ATOMKI review is currently not mentioned, not sure if some Wikipedia articles should get a mention or how do these things work)
- Consistent use of `bm` vs `mathbf`
- Consistent use of $\overline{\mathcal{M}}$ instead of \mathcal{M} when talking about the map of the means (so most of the time)
- Proper equation numbering when deriving a relation
- Hugo should be mentioned somewhere in the title pages probably?
- Consistent itemize/enumerate style (namely spacing) that looks good (ideally set by some macro? maybe the new MFF UK template will solve this?)
- Consistent gas mixture notation (e.g., 90:10 Ar:CO₂). Maybe mention at the beginning that it is a molar ratio.
- Labels of figures and tables – maybe in bold? Abbreviated?
- Check graph labels, make them bigger if needed.
- "The map" can be viewed as a mapping between spaces or just as a coordinate transform.
- Maybe switch to cleverref.
- siunitx qty not SI
- Correct em dash?

- In the future, it might be useful to save pictures as tex files whenever possible and using siunitx for the labels
 - Should list of figures/tables be in the thesis? Also, it is currently not in TOC.
 - link to GitHub
- Random notes:
- Terminology consistency – ionization/primary/secondary electrons
 - Consistent TPC vs OFTPC acronym usage in the text or individual chapters.
 - Only electrons that start and end in the sector closer than 0.5 cm are used for reconstruction (newest version).
 - Attachment, Penning transfer and secondary ionization not considered in the microscopic simulation.
 - Suspicious artifacts of trilinear interpolation in Fig. 1.14. **Fixed – integers instead of doubles in the implementation, influenced reconstruction SIGNIFICANTLY (but not simulation).**
 - Profiling of the reconstruction!!!! Find out what's taking the most time (probably Runge-Kutta integration which the fit calls a lot). Could gradually decrease the step size to refine the fit instead of making it small right away (arbitrarily small – the effect of this was never tested). This could take some time to do properly (find a profiler or make profiling macros).
 - Slow drift velocity good for z reconstruction, too low leads to recombination
 - Could add link to the GitHub repository, mention CMake? Details about simulating on MetaCentrum?
 - The first used track had 8 MeV momentum $p = \gamma mv$ (not kinetic energy $E_{\text{kin}} = (\gamma - 1)mc^2 = \sqrt{p^2c^2 + m^2c^4} - mc^2 \approx 7.5 \text{ MeV}$)
 - Maybe cite Garfield++ user manual instead?
 - Using TRandom3 for random number generation.
 - Does the RK fit error correlate with the actual error?
 - Some Garfield settings in micro track generation probably not mentioned
 - one-to-one only means injection (not bijection)? Make sure correct terminology is used.

Future

Should this be in the TOC?

Things planned for the future:

- Testing the reconstruction algorithm by measuring real particles with a known energy distribution (at first just laser, muons?).

- The **Fast Simulation with Ionization Electron Map** is planned for the future. It will use the HEED program [44] to simulate the primary particle and the Ionization Electron Map (see Section 3.2) to simulate the drift of secondary electrons. It should be significantly faster than the Microscopic Simulation but offer comparable precision since it will rely on an already simulated drift map. (Primary track simulated in HEED. Readout parameters by interpolating the map. Diffusion from the map for randomization.) Currently more or less implemented, but it turns out that the initial energy of ionization electrons cannot be discarded.
- Account for GEM, delta electrons, ...
- Likelihood approach instead of least squares (if it improves the reconstruction significantly), we should at least use a better method than taking the center of the TPC bin.
- More detailed electric field simulation (if needed, GEM will have more complex field, some irregularities in the field should be considered)
- Account for the triggering in MWPC/TPX3 (particle travels from TPX3 to MWPC basically immediately – fraction of a nanosecond so there should be no significant difference)
- Better choice of initial velocity in the map? Maybe look at the distribution for e+e- with different energies and either use this distribution combined for all (if the dependence isn't too big) or even few different simulations? Might (?) raise the requirement of electrons simulated per position. Or maybe just make some adjustment of the z coordinate in the end?
- Create a pad map. Might be worth it to use gradient descent search after all.
- Testing of different pad layouts possible.

1404 Likelihood - inverse map

1405 If we wanted to further improve this procedure, taking into account the whole
 1406 map \mathcal{M} , we could make an "inverse map" from \mathcal{R} to distributions on \mathcal{D} . We could
 1407 achieve this by taking the normalized probability density of an electron with initial
 1408 coordinates (x, y, z) having readout coordinates (x', y', t) . If we fix (x', y', t) , we
 1409 get an unnormalized probability density $f(x, y, z) = \mathcal{M}_{(x,y,z)}(x', y', t)$ (assuming
 1410 that all initial coordinates are a priori equally likely). This could potentially
 1411 improve the discrete reconstruction if we take the mean value of this probability
 1412 density across the pad and time bin

$$f_{\text{pad, bin}}(x, y, z) = \frac{1}{A_{\text{pad}} \Delta t_{\text{bin}}} \int_{\text{pad, bin}} \mathcal{M}_{(x,y,z)}(x', y', t) dx' dy' dt \quad (4.33)$$

1413 and using it for a likelihood fit instead of using least squares. This still assumes
 1414 that all initial coordinates are equally likely which is clearly not the case for
 1415 a primary particle track. In the future, we could even use the fast track simulation
 1416 with the map (should be possible to make around 1000 tracks per minute per core

1417 with current settings), create a big set of tracks with reasonable parameters and
1418 use these to get an approximation of the probability distribution of the detector
1419 response. Some approximations would be necessary when interpreting the data to
1420 decrease the degrees of freedom of this distribution (we would have to pick a set of
1421 parameters and assume that some of them are independent). This could give us
1422 an idea about the best achievable resolution (how significantly will the detector
1423 response differ for a given change in energy). If the difference is significant, we
1424 could try to further improve the likelihood fit.

1425 Bibliography

- 1426 1. *Garfield++* [<https://garfieldpp.web.cern.ch/garfieldpp/>]. [N.d.].
1427 Accessed: 2023-05-18.
- 1428 2. BRUN, Rene; RADEMAKERS, Fons. Root — An Object Oriented Data Analysis Framework. *Nucl. Instrum. Methods Phys. Res. Sect. A: Accel. Spectrom. Detect. Assoc. Equip.* 1997, vol. 389, no. 1–2, pp. 81–86. Available from DOI: [10.1016/s0168-9002\(97\)00048-x](https://doi.org/10.1016/s0168-9002(97)00048-x). Proceedings AIHENP'96 Workshop, Lausanne, Sep. 1996, See also <https://root.cern/>, Paper published in the Linux Journal, Issue 51, July 1998.
- 1434 3. *About MetaCentrum* [<https://metavo.metacentrum.cz/en/about/index.html>]. 2023. Accessed: 2024-11-27.
- 1436 4. ROSE, M. E. Internal Pair Formation. *Phys. Rev.* 1949, vol. 76, pp. 678–681.
1437 Available from DOI: [10.1103/PhysRev.76.678](https://doi.org/10.1103/PhysRev.76.678).
- 1438 5. ESSIG, R. et al. *Dark Sectors and New, Light, Weakly-Coupled Particles*. 2013. Available from arXiv: [1311.0029](https://arxiv.org/abs/1311.0029) [hep-ph].
- 1440 6. DE BOER, F.W.N. et al. A deviation in internal pair conversion. *Phys. Lett. B*. 1996, vol. 388, no. 2, pp. 235–240. ISSN 0370-2693. Available from DOI: [https://doi.org/10.1016/S0370-2693\(96\)01311-1](https://doi.org/10.1016/S0370-2693(96)01311-1).
- 1443 7. BOER, F W N de et al. Excess in nuclear pairs near 9 MeV/ invariant mass. *J. Phys. G: Nucl. Part. Phys.* 1997, vol. 23, no. 11, p. L85. Available from DOI: [10.1088/0954-3899/23/11/001](https://doi.org/10.1088/0954-3899/23/11/001).
- 1446 8. BOER, F W N de et al. Further search for a neutral boson with a mass around 9 MeV/c². *J. Phys. G: Nucl. Part. Phys.* 2001, vol. 27, no. 4, p. L29. Available from DOI: [10.1088/0954-3899/27/4/102](https://doi.org/10.1088/0954-3899/27/4/102).
- 1449 9. VITÉZ, Attila et al. Anomalous Internal Pair Creation in ⁸Be as a Signature of the Decay of a New Particle. *Acta Phys. Pol. B - ACTA PHYS POL B*. 2008, vol. 39, p. 483.
- 1452 10. KRASZNAHORKAY, A. et al. Searching for a light neutral axial-vector boson in isoscalar nuclear transitions. *Frascati Phys. Ser.* 2012, vol. 56, p. 86.
- 1454 11. KRASZNAHORKAY, A. J. et al. Observation of Anomalous Internal Pair Creation in ⁸Be: A Possible Indication of a Light, Neutral Boson. *Phys. Rev. Lett.* 2016, vol. 116, no. 4. ISSN 1079-7114. Available from DOI: [10.1103/physrevlett.116.042501](https://doi.org/10.1103/physrevlett.116.042501).
- 1458 12. TILLEY, D.R. et al. Energy levels of light nuclei A=8,9,10. *Nucl. Phys. A*. 2004, vol. 745, no. 3, pp. 155–362. ISSN 0375-9474. Available from DOI: <https://doi.org/10.1016/j.nuclphysa.2004.09.059>.
- 1461 13. SAS, N. J. et al. *Observation of the X17 anomaly in the ⁷Li(p,e⁺e⁻)⁸Be direct proton-capture reaction*. 2022. Available from arXiv: [2205.07744](https://arxiv.org/abs/2205.07744) [nucl-ex].
- 1464 14. KRASZNAHORKAY, A. J. et al. New anomaly observed in ⁴He supports the existence of the hypothetical X17 particle. *Phys. Rev. C*. 2021, vol. 104, no. 4. ISSN 2469-9993. Available from DOI: [10.1103/physrevc.104.044003](https://doi.org/10.1103/physrevc.104.044003).

- 1467 15. TILLEY, D.R. et al. Energy levels of light nuclei A = 4. *Nucl. Phys. A*.
1468 1992, vol. 541, no. 1, pp. 1–104. ISSN 0375-9474. Available from DOI: [https://doi.org/10.1016/0375-9474\(92\)90635-W](https://doi.org/10.1016/0375-9474(92)90635-W).
- 1470 16. KRASZNAHORKAY, A. J. et al. New anomaly observed in ^{12}C supports the
1471 existence and the vector character of the hypothetical X17 boson. *Phys. Rev.*
1472 *C*. 2022, vol. 106, p. L061601. Available from DOI: 10.1103/PhysRevC.106.
1473 L061601.
- 1474 17. AJZENBERG-SELOVE, F. Energy levels of light nuclei A = 11,12. *Nucl. Phys.*
1475 *A*. 1990, vol. 506, no. 1, pp. 1–158. ISSN 0375-9474. Available from DOI:
1476 [https://doi.org/10.1016/0375-9474\(90\)90271-M](https://doi.org/10.1016/0375-9474(90)90271-M).
- 1477 18. KÁLMÁN, Péter; KESZTHELYI, Tamás. Anomalous internal pair creation.
1478 *The Eur. Phys. J. A*. 2020, vol. 56. Available from DOI: 10.1140/epja/
1479 s10050-020-00202-z.
- 1480 19. ALEKSEJEVS, A. et al. *A Standard Model Explanation for the "ATOMKI*
1481 *Anomaly"*. 2021. Available from arXiv: 2102.01127 [hep-ph].
- 1482 20. FENG, Jonathan L. et al. Protophobic Fifth-Force Interpretation of the Ob-
1483 served Anomaly in ^8Be Nuclear Transitions. *Phys. Rev. Lett.* 2016, vol. 117,
1484 p. 071803. Available from DOI: 10.1103/PhysRevLett.117.071803.
- 1485 21. ANH, Tran The et al. Checking the 8Be Anomaly with a Two-Arm Electron
1486 Positron Pair Spectrometer. *Universe*. 2024, vol. 10, no. 4, p. 168. ISSN 2218-
1487 1997. Available from DOI: 10.3390/universe10040168.
- 1488 22. ABRAAMYAN, Kh. U. et al. *Observation of structures at ~ 17 and ~ 38 MeV/c 2*
1489 *in the $\gamma\gamma$ invariant mass spectra in pC, dC, and dCu collisions at p_{lab} of a*
1490 *few GeV/c per nucleon*. 2023. Available from arXiv: 2311.18632 [hep-ex].
- 1491 23. THE MEG II COLLABORATION et al. *Search for the X17 particle in $^7\text{Li}(p, e^+e^-)^8\text{Be}$*
1492 *processes with the MEG II detector*. 2024. Available from arXiv: 2411.07994
1493 [nucl-ex].
- 1494 24. HILKE, H J. Time Projection Chambers. *Rep. Prog. Phys.* 2010, vol. 73, no.
1495 11, p. 116201. Available from DOI: {10.1088/0034-4885/73/11/116201}.
- 1496 25. NAVAS, S. et al. Review of particle physics. *Phys. Rev. D*. 2024, vol. 110,
1497 no. 3, p. 030001. Available from DOI: 10.1103/PhysRevD.110.030001.
- 1498 26. ABED ABUD, Adam et al. A Gaseous Argon-Based Near Detector to En-
1499 hance the Physics Capabilities of DUNE. 2022. Available from DOI: 10.
1500 48550/arXiv.2203.06281.
- 1501 27. AIHARA, H. et al. Spatial Resolution of the PEP-4 Time Projection Cham-
1502 ber. *IEEE Trans. on Nucl. Sci.* 1983, vol. 30, no. 1, pp. 76–81. Available
1503 from DOI: 10.1109/TNS.1983.4332223.
- 1504 28. LOKEN, Stewart C. et al. Performance of the Signal Processing System for
1505 the Time Projection Chamber. *IEEE Trans. on Nucl. Sci.* 1983, vol. 30, no.
1506 1, pp. 162–166. Available from DOI: 10.1109/TNS.1983.4332243.
- 1507 29. COWAN, G. D. *Inclusive π^\pm , K^\pm , and p , \bar{p} production in e^+e^- annihilation*
1508 *at $\sqrt{s} = 29$ GeV*. 1988. Available from DOI: 10.2172/5188194. Lawrence
1509 Berkeley National Lab. (LBNL), Berkeley, CA (United States).

- 1510 30. ALME, J. et al. The ALICE TPC, a large 3-dimensional tracking device
1511 with fast readout for ultra-high multiplicity events. *Nucl. Instrum. Methods*
1512 *Phys. Res. Sect. A: Accel. Spectrom. Detect. Assoc. Equip.* 2010, vol. 622,
1513 no. 1, pp. 316–367. ISSN 0168-9002. Available from DOI: <https://doi.org/10.1016/j.nima.2010.04.042>.
- 1514
- 1515 31. HAUER, Philip. The upgraded ALICE TPC. *Nucl. Instrum. Methods Phys.*
1516 *Res. Sect. A: Accel. Spectrom. Detect. Assoc. Equip.* 2022, vol. 1039, p. 167023. ISSN
1517 0168-9002. Available from DOI: <https://doi.org/10.1016/j.nima.2022.167023>.
- 1518
- 1519 32. DI MAURO, A. Particle identification methods other than RICH. *Nucl. Instrum.*
1520 *Methods Phys. Res. Sect. A: Accel. Spectrom. Detect. Assoc. Equip.* 2020, vol. 952, p. 162124. ISSN 0168-9002. Available from DOI: <https://doi.org/10.1016/j.nima.2019.04.078>. 10th International Workshop on
1521 Ring Imaging Cherenkov Detectors (RICH 2018).
- 1522
- 1523
- 1524 33. ADAMOVÁ, D. et al. The CERES/NA45 radial drift Time Projection Chamber.
1525 *Nucl. Instrum. Methods Phys. Res. Sect. A: Accel. Spectrom. Detect.*
1526 *Assoc. Equip.* 2008, vol. 593, no. 3, pp. 203–231. ISSN 0168-9002. Available
1527 from DOI: [10.1016/j.nima.2008.04.056](https://doi.org/10.1016/j.nima.2008.04.056).
- 1528
- 1529 34. BIAGI, S.F. Monte Carlo simulation of electron drift and diffusion in count-
1530 ing gases under the influence of electric and magnetic fields. *Nucl. Instrum.*
1531 *Methods Phys. Res. Sect. A: Accel. Spectrom. Detect. Assoc. Equip.* 1999,
1532 vol. 421, no. 1, pp. 234–240. ISSN 0168-9002. Available from DOI: [https://doi.org/10.1016/S0168-9002\(98\)01233-9](https://doi.org/10.1016/S0168-9002(98)01233-9).
- 1533
- 1534 35. ALBAYRAK, I. et al. Design, construction, and performance of the GEM
1535 based radial time projection chamber for the BONuS12 experiment with
1536 CLAS12. *Nucl. Instrum. Methods Phys. Res. Sect. A: Accel. Spectrom. De-*
1537 *tect. Assoc. Equip.* 2024, vol. 1062, p. 169190. ISSN 0168-9002. Available from
DOI: <https://doi.org/10.1016/j.nima.2024.169190>.
- 1538
- 1539 36. ANDERSON, E. et al. Observation of the effect of gravity on the motion of
1540 antimatter. *Nature*. 2023, vol. 621, pp. 716–722. Available from DOI: [10.1038/s41586-023-06527-1](https://doi.org/10.1038/s41586-023-06527-1).
- 1541
- 1542 37. Design of a Radial TPC for Antihydrogen Gravity Measurement with ALPHA-
1543 g. In: *Proceedings of the 12th International Conference on Low Energy An-*
1544 *tiproton Physics (LEAP2016)*. [N.d.]. Available from DOI: [10.7566/JPSCP.18.011015](https://doi.org/10.7566/JPSCP.18.011015).
- 1545
- 1546 38. CAPRA, A. Antihydrogen annihilation detection: the ALPHA-g radial TPC.
1547 *PoS*. 2025, vol. EXA-LEAP2024, p. 063. Available from DOI: [10.22323/1.480.0063](https://doi.org/10.22323/1.480.0063).
- 1548
- 1549 39. WIECHULA, Jens; CHRISTIANSEN, Peter. *The ALICE Time Projection Cham-*
1550 *ber* [https://www.hep.lu.se/staff/christiansen/teaching/spring_2013/the_alice_tpc.pdf]. 2013. Slides credited to J. Wiechula; hosted on
1551 Lund University website.

- 1552 40. HILDÉN, T. et al. Optical quality assurance of GEM foils. *Nucl. Instrum.*
1553 *Methods Phys. Res. Sect. A: Accel. Spectrom. Detect. Assoc. Equip.* 2015,
1554 vol. 770, pp. 113–122. ISSN 0168-9002. Available from DOI: 10.1016/j.
1555 *nima*.2014.10.015.
- 1556 41. AHMED, Misbah Uddin. *Simulation of the electron and ion movement through*
1557 *a 4-GEM stack*. 2021. Institut für Kernphysik.
- 1558 42. MARMELAD. *3D interpolation2.svg*. 2025. Available also from: https://commons.wikimedia.org/wiki/File:3D_interpolation2.svg. Licensed
1559 under CC BY-SA 3.0 (<https://creativecommons.org/licenses/by-sa/3.0/legalcode>). Accessed: 9-April-2025.
- 1560 43. CMGLEE. *Trilinear interpolation visualisation*. 2025. Available also from:
1561 https://commons.wikimedia.org/wiki/File:Trilinear_interpolation_visualisation.svg. Licensed under CC BY-SA 3.0 (<https://creativecommons.org/licenses/by-sa/3.0/legalcode>). Accessed: 26-March-2025.
- 1562 44. SMIRNOV, I.B. Modeling of ionization produced by fast charged particles in
1563 gases. *Nucl. Instrum. Methods Phys. Res. Sect. A: Accel. Spectrom. Detect.*
1564 *Assoc. Equip.* 2005, vol. 554, no. 1, pp. 474–493. ISSN 0168-9002. Available
1565 from DOI: <https://doi.org/10.1016/j.nima.2005.08.064>.
- 1566 45. SCOTT, DAVID W. On optimal and data-based histograms. *Biometrika*.
1567 1979, vol. 66, no. 3, pp. 605–610. ISSN 0006-3444. Available from DOI: 10.
1568 [10.1093/biomet/66.3.605](https://doi.org/10.1093/biomet/66.3.605).
- 1569 46. FREEDMAN, David A.; DIACONIS, Persi. On the histogram as a density esti-
1570 mator:L2 theory. *Zeitschrift fur Wahrscheinlichkeitstheorie und Verwandte*
1571 *Gebiete*. 1981, vol. 57, pp. 453–476. Available also from: <https://api.semanticscholar.org/CorpusID:14437088>.

1572 **Acknowledgments:** Computational resources were provided by the e-INFRA
1573 CZ project (ID:90254), supported by the Ministry of Education, Youth and Sports
1574 of the Czech Republic. **Figures that were drawn with GeoGebra. Maybe grant?**

List of Figures

1581	0.1	The ATOMKI anomalous IPC measured for different nuclei.	5
1582	0.2	Results from the Hanoi spectrometer – angular e^+e^- pair correlations measured in the ${}^7\text{Li}(p, e^+e^-){}^8\text{Be}$ reaction at $E_p = 1225$ keV [21].	6
1583	0.3	Results from the MEG II experiments – angular correlation of e^+e^- pairs with $E_{\text{sum}} \in [16, 20]$ MeV measured in the ${}^7\text{Li}(p, e^+e^-){}^8\text{Be}$ reaction with proton beam energies 500 and 1080 keV. The 500 keV dataset is fitted with Monte Carlo of both the IPC deexcitation and the EPC produced by gammas [23].	7
1584	0.4	Schematics of the detector at the Van der Graaff facility at IEAP CTU (ref).	7
1585	1.1	Particle identification in the PEP-4 TPC at SLAC based on the energy loss per distance $\frac{dE}{dx}$ in the 80:20 Ar:CH ₄ filling at 8.5 atm pressure [26]. The reference doesn't point to the original PEP-4 article because this adapted version of the original picture that they used in the DUNE article looks better.	9
1586	1.2	Schematic view of the PEP-4 TPC [28]. A charged particle produced in a collision in the beam pipe creates a spiral ionization track in the magnetic field. The central cathode then accelerates ionization electrons towards the endcap anode wires where they are multiplied and read out. A TPC sector with a detailed view of one of the pad rows is shown on the right [29].	12
1587	1.3	Schematic view of the ALICE TPC [31]. The readout at each endcap is divided into 18 sectors, each subdivided into an Inner Readout Chamber (IROC) with one GEM stack and Outer Readout Chamber (OROC) with three GEM stacks. A visualization of a GEM stack is on the right [32].	13
1588	1.4	Experimental setup of the CERES/NA45 experiment with two Ring Imaging Cherenkov Counters (RICHs) on the left and a rTPC on the right. The magnetic field (red) is generated by two solenoidal coils (blue) with opposite polarity. Produced ionization electrons drift outward radially towards the readout chamber (yellow) [33].	14
1589	1.5	Cross section of a CERES/NA45 readout MWPC. The wires are stretched in the azimuthal direction above the pad plane. The gating grid controls the passage of electrons and ions. [33].	14
1590	1.6	Schematic view of the BONuS12 rTPC [35].	15
1591	1.7	Schematic view of the ALPHA-g detector [37].	16
1592	1.8	Schematic view of the ALICE MWPC readout (working principle) [39].	17
1593	1.9	Gas Electron Multiplier (GEM).	18
1594	1.10	Garfield simulation of an avalanche in a GEM hole [41]. An incoming electron (orange) is accelerated in the strong electric field of the GEM and causes further ionization multiplying the number of free electrons (orange). Most of the produced cations (red) are captured by the GEM cathode.	18
1595	1.11	MICRO-MEsh GAseous Structure (Micromegas) [25].	19

1625	1.12 Schematics of the first sector OFTPC with detector space coordinates.	21
1626		
1627	1.13 Pad layout of the OFTPC and its parameters. Pads 102, 124 and 127 are irregular, the rest has the same dimensions.	22
1628		
1629	1.14 Magnetic field simulation results. The OFTPC volume and the vacuum tube are marked with black lines, the magnets are marked with red lines. The coordinates of the magnets from the CAD drawing seem to be 9/10 of the ones from the magnetic simulation (fixed, the magnetic simulation parameters are off).	23
1630		
1631		
1632		
1633		
1634	1.15 Visualization of trilinear interpolation as a composition of linear interpolations (inspired by [42]). We want to interpolate the value in the red point C . First we interpolate between the four pairs of blue points sharing the last two indices along the x -axis (Eq. 1.15), then between the two pairs of the resulting green points along the y -axis (Eq. 1.16) and finally between the two resulting orange points along the z -axis to get the final red value (Eq. 1.17).	24
1635		
1636		
1637		
1638		
1639		
1640		
1641	1.16 Geometric interpretation of trilinear interpolation as expressed in Equation 1.19. The colored dots represent the values in given points and the colored boxes represent the volume in the opposite corner by which the corresponding values are multiplied. The black dot represents the interpolated value which is multiplied by the entire volume [43].	25
1642		
1643		
1644		
1645		
1646		
1647	2.1 Comparison of drift lines for two different gas mixtures 90:10 and 70:30 Ar:CO ₂ . The electron track is marked in black, the drift lines of the ionization electrons are marked in orange. In this example, we assume a larger OFTPC volume with readout at $z = 8$ cm.	28
1648		
1649		
1650		
1651	2.2 A visualization of a set of tracks from the grid-like testing sample with the same kinetic energy.	29
1652		
1653	2.3 A comparison of the HEED track from the microscopic simulation in Section 2.1.1 with a Runge-Kutta track with the same initial parameters and $\tau_{\text{step}} = 0.1$ ps (reducing the step further doesn't make a visible difference). In the view of the tracks on the left, the distance of the HEED ionization electrons from the RK4 track is exaggerated 1000 \times . On the right, the dependence of the HEED electrons residuals (i.e., their shortest distance to the RK4 track) on their z -coordinate is shown. The images look the same even for 100,000x smaller step, so the residuals are a result of something that HEED does (maybe a different interpolation technique for the magnetic field? the pattern looks similar for two different tracks so it can't be scattering).	31
1654		
1655		
1656		
1657		
1658		
1659		
1660		
1661		
1662		
1663		
1664		
1665	3.1 Linear fit of the drift time t dependence on the distance to the readout $d_r = 8$ cm – z for the ionization electrons in 90:10 (left) and 70:30 (right) Ar:CO ₂ gas composition. Only electrons inside the TPC (red) are fitted. The parameters are $v_d = 3.39$ cm/ μ s, $d_0 = -0.41$ cm for 90:10, and $v_d = 0.939$ cm/ μ s, $d_0 = -0.11$ cm for 70:30 Ar:CO ₂	33
1666		
1667		
1668		
1669		
1670		

1671	3.2 Reconstruction (black) of the starting position of ionization elec-	
1672	trons (red) using parameters obtained from the fit (Fig. 3.1). Two	
1673	gas compositions 90:10 (left) and 70:30 Ar:CO ₂ (right) are compared.	34
1674	3.3 Comparison of residuals (i.e., the distance from the reconstructed	
1675	point to the simulated ionization electron starting point) dependence	
1676	on x for two gas mixtures 90:10 (red) and 70:30 Ar:CO ₂	
1677	(blue).	34
1678	3.4 A 3D visualization of the mapping of means $\bar{\mathcal{M}}$ for the 90:10	
1679	Ar:CO ₂ gas. A regular grid \mathbb{G} with $l = 1$ cm in the detector space	
1680	is mapped to an irregular grid $\mathbb{G}^{-1} \equiv \bar{\mathcal{M}}(\mathbb{G})$ in the readout space.	35
1681	3.5 A test of the 90:10 Ar:CO ₂ map simulation with spacing $l = 1.5$ cm.	
1682	The resulting drift lines of evenly spaced electrons are displayed in	
1683	orange.	36
1684	3.6 Dependence of the drift times of the simulated map $\bar{\mathcal{M}}$ on the	
1685	z -coordinate. Two gas mixtures 90:10 (left) and 70:30 Ar:CO ₂	
1686	(right) are compared. The spread is caused by varying Lorentz	
1687	angles.	37
1688	3.7 The $x't$ projection of the $\mathcal{M}(\mathbb{G}_{y=0})$ mapping of a part of the regu-	
1689	lar grid \mathbb{G} . The means $\bar{\mathcal{M}}(\mathbb{G}_{y=0})$ are marked with red crosses, and	
1690	the diffusion error is denoted by black 95% confidence error ellipses	
1691	computed from the diagonalized covariance matrices $\mathcal{M}_{\Sigma}(\mathbb{G}_{y=0})$.	
1692	Two gas mixtures 90:10 (left) and 70:30 Ar:CO ₂ (right) are com-	
1693	pared. The first mixture shows differences of t for electrons with	
1694	same initial z but different initial x . For the second mixture, these	
1695	differences are negligible in comparison with the diffusion.	38
1696	3.8 The regular grid \mathbb{G} projected by the mapping $\bar{\mathcal{M}}$ from the detector	
1697	space onto the $x'y'$ plane (t is not plotted). Layers with lower	
1698	z -coordinate (i.e., further away from the readout) are displayed	
1699	with darker colors. The OFTPC volume is marked with black	
1700	lines. Two gas mixtures 90:10 (left) and 70:30 Ar:CO ₂ (right) are	
1701	compared.	38
1702	3.9 The $\mathcal{M}(\mathbb{G}_{-8})$ mapping of the bottom ($z = -8$ cm) layer \mathbb{G}_{-8} of the	
1703	regular grid $\mathbb{G} \subset \mathcal{D}$. It includes both the mapping of means $\bar{\mathcal{M}}$ and	
1704	of covariances \mathcal{M}_{Σ} . Individual electrons from the map simulation	
1705	are marked with red dots. Two gas mixtures 90:10 (left) and 70:30	
1706	Ar:CO ₂ (right) are compared.	39
1707	3.10 The readout coordinate x' for points on the grid $\mathbb{G}_{y=0}$ plotted	
1708	against their initial coordinate z . The means are marked with red	
1709	crosses, the diffusion in x' is denoted by standard error bars. Two	
1710	gas mixtures 90:10 (left) and 70:30 Ar:CO ₂ (right) are compared.	39
1711	3.11 Reconstruction (black) of the starting position of ionization elec-	
1712	trons (red) using the inversion of the ionization electron map. Two	
1713	gas compositions 90:10 (left) and 70:30 Ar:CO ₂ (right) are compared.	43
1714	3.12 Comparison of residuals from the RASD (black) and map inversion	
1715	(red) reconstruction methods. Tracks in two different gas compo-	
1716	sitions 90:10 (left) and 70:30 Ar:CO ₂ (right) are compared.	44
1717	3.13 Map inversion reconstruction residuals (for the individual coordi-	
1718	nates and total) of the testing track in 90:10 Ar:CO ₂ gas mixture.	44

1719	3.14 Map inversion reconstruction residuals (for the individual coordinates and total) of the testing track in 70:30 Ar:CO ₂ gas mixture.	45
1720		
1721	3.15 Reconstruction of detector coordinates for ionization electrons that	
1722	are read out in a certain pad (number 66 near the center of the	
1723	OFTPC, and number 12 near the magnet pole that suffers from	
1724	large distortion effects, causing issues with interpolation on the	
1725	inverse grid) and time bin. Boundaries of regions mapped to these	
1726	discrete coordinates are shown in black, reconstructed center of	
1727	the pad and time bin is shown in red, and map points used for	
1728	the center reconstruction are shown in blue. Readout is placed at	
1729	$z = -8$ cm.	47
1730		
1731	3.16 Reconstruction of detector coordinates corresponding to pad 12	
1732	(near the magnet pole) for different time bins. Unlike Fig. 3.15,	
1733	we used the gradient descent search, which handles the large dis-	
1734	tortion better. In its current unoptimized state, these figures took	
1735	280 times longer to produce, compared to the interpolation on the	
1736	inverse grid.	48
1737		
1738	3.17 Discrete reconstruction of an 8 MeV track from the grid-like test-	
1739	ing sample (described in Sec. 2.1.2) with minimal values of θ and	
1740	ϕ initial direction angles. The simulated ionization vertices are	
1741	shown in red, the reconstructed track is shown with the colored	
1742	boxes. The number of electrons in each pad/time bin is denoted	
1743	with the size of the boxes and their color.	48
1744		
1745	4.1 Energy reconstruction of a 7.51 MeV track in a 70:30 Ar:CO ₂ gas	
1746	mixture (described in detail in Sec. 2.1.1) using a cubic spline fit	
1747	with four evenly spaced nodes of points reconstructed using the map.	51
1748		
1749	4.2 Circle and lines 2D energy reconstruction of a 7.51 MeV track in	
1750	a 70:30 Ar:CO ₂ gas mixture (described in detail in Sec. 2.1.1) re-	
1751	constructed with the map. The fitted position of the nodes is	
1752	$(x_1, z_1) = (5.20, -0.07)$ cm and $(x_2, z_2) = (14.43, -1.93)$ cm, the	
1753	radius is $r = 20.79$ cm. The resulting energy is 7.70 MeV, the mag-	
1754	netic field along the track is shown on the right.	53
1755		
1756	4.3 Visualization of the 3D geometry of the Circle and Lines Fit and its	
1757	parameters. Projection of some points on the XY plane is shown	
1758	to better display the spatial arrangement.	54
1759		
1760	4.4 3D circle fit of an 8 MeV track (red points) from the grid-like test-	
1761	ing sample (described in Sec. 2.1.2) with minimal values of θ and ϕ	
1762	initial direction angles. Both fits of the original (green) and recon-	
1763	structed track (blue) are shown. Resulting parameter values are	
1764	given in Table 4.1.	57
1765		
1766	4.5 Relative error of the energy of Runge-Kutta tracks reconstructed	
1767	with the 3D circle and lines fit. The middle field (left) and the	
1768	average field (right) methods are compared. Dependence on the	
1769	initial direction angles θ and φ is small in comparison.	58
1770		
1771	4.6 Demonstration of the convexity of the distance function $d(\alpha)$ for	
1772	a circular track (see Equation 4.29).	59
1773		

1780 List of Tables

¹⁷⁸⁵ List of Abbreviations

- ¹⁷⁸⁶ **ALPHA** Antihydrogen Laser Physics Apparatus
- ¹⁷⁸⁷ **BONuS12** Barely Off-shell NeUtron Structure 12 GeV
- ¹⁷⁸⁸ **GEM** Gas Electron Multiplier
- ¹⁷⁸⁹ **HEED** High Energy Electro-Dynamics
- ¹⁷⁹⁰ **IEAP CTU** Institute of Experimental and Applied Physics, Czech Technical
¹⁷⁹¹ University in Prague
- ¹⁷⁹² **IPC** Internal Pair Creation
- ¹⁷⁹³ **EPC** External Pair Creation
- ¹⁷⁹⁴ **FWHM** Full Width at Half Maximum
- ¹⁷⁹⁵ **LArTPC** Liquid Argon TPC
- ¹⁷⁹⁶ **Micromegas** MICRO-MEsh GAseous Structure
- ¹⁷⁹⁷ **MPGD** Micro-Pattern Gaseous Detector
- ¹⁷⁹⁸ **MWPC** Multi-Wire Proportional Chamber
- ¹⁷⁹⁹ **OFTPC** Orthogonal Fields TPC
- ¹⁸⁰⁰ **PCB** Printed Circuit Board
- ¹⁸⁰¹ **RASD** Reconstruction Assuming Steady Drift
- ¹⁸⁰² **RICH** Ring Imaging Cherenkov Counter
- ¹⁸⁰³ **RK4** Runge-Kutta 4th order
- ¹⁸⁰⁴ **RPC** Resistive Plate Chamber
- ¹⁸⁰⁵ **RPWELL** Resistive Plate WELL
- ¹⁸⁰⁶ **rTPC** radial-drift TPC
- ¹⁸⁰⁷ **THGEM** THick GEM
- ¹⁸⁰⁸ **ToA** time-of-arrival
- ¹⁸⁰⁹ **ToT** time-over-threshold
- ¹⁸¹⁰ **TPC** Time Projection Chamber
- ¹⁸¹¹ **TPX3** Timepix3
- ¹⁸¹² **μ -PIC** Micro-Pixel Gas Chamber
- ¹⁸¹³ **μ -RWELL** Micro-RWELL